Volcanic Ash in the Atmosphere

Gemma Susan Prata

St Edmund Hall

University of Oxford

A thesis submitted for the degree of

Doctor of Philosophy

Hilary 2018

This thesis is dedicated

to Mum

for constant encourage-mint

Acknowledgements

I would like to gratefully acknowledge the Clarendon Fund, Burdett Coutts Fund and St Edmund Hall for the funding of my doctorate. Without this financial support I would not have been able to undertake this amazing opportunity to study at the University of Oxford.

I have many people to whom I owe a great debt for their continued support throughout my DPhil. Firstly, I would like to thank my supervisors, Tamsin Mather and David Pyle. I've had a difficult time over the past few years, but you have patiently supported me and given me encouragement and understanding when I've needed it most. Thank you for the many insightful discussions and opportunities you have provided, helping me to learn and grow as a researcher. Thank you to my research group who have always taken an interest in my work and have provided many fruitful discussions. I'd also like to acknowledge the many people in the Department of Earth Sciences who have helped in any way, large or small, with my project. To my collaborators in the Department of Atmospheric, Oceanic and Planetary Physics, Don Grainger, Elisa Carboni and Lucy Ventress, thank you for your helpful input and feedback throughout my DPhil. I feel so lucky to have had the opportunity to work in such a multidisciplinary environment.

Thank you to my office mates, Stefan, John, Vicky, Maria, Will, Dave, Afsaneh & Alexandre. It has been a pleasure to share a workspace with all of you. Thank you for reading through various drafts, giving feedback, the many welcome tea breaks, and generally helping me stay on track. Thanks

also to my writing buddy Erfan—we crushed loads of tomatoes! To all my Teddy Hall friends, there are too many to mention, but I think that speaks volumes for the warm and welcoming environment the College fosters. You've been like a family away from home to me.

I would also like to thank the St Edmund Hall Boat Club, who have provided a much-needed physical and mental outlet during my studies. College rowing at Oxford has given me some amazing opportunities and has taught me important lessons about teamwork and discipline. Huge thanks go to all my various coaches and crew members over the years, I wish I could name you all but it would take up most of the thesis if I did!

To Charlotte, I couldn't have got through this without you. Literally, seeing as you are submitting this thesis for me as my proxy while I'm in Australia! Your friendship and support have meant the world to me and I can't thank you enough.

Finally, thanks go to my family for their unwavering support throughout my academic journey. To my parents, Alison and Fred, thank you for encouraging me and supporting my academic pursuits. Mum, thank you for always proof reading anything I give you, even at short notice! Dad, I can't thank you enough for all the help and advice you have given me over the years. Thank you in particular for all the feedback you've given me on some of the more technical aspects of my work. I'm lucky to have your knowledge and experience to draw from. To my sister, Katharine, your hard work and dedication has been an inspiration to me and has helped me persevere with this. I look forward to reading your own PhD thesis in a few years' time. And last, but certainly not least, my brother, Andrew aka Dr Prata the 2nd, for not only helping me with the typesetting of this thesis in LaTeX, but also for your thoughtful input and feedback on various drafts. I look forward to writing a paper together!

Abstract

This thesis presents new work on the characterisation of volcanic ash in the atmosphere. The eruption of Eyjafjallajökull in 2010 brought the issue of ash in the atmosphere into sharp focus. Radiative transfer models used in remote sensing and hazard assessment of volcanic ash require knowledge of ash optical parameters, which are governed by the spectral complex refractive index ($n + ik$: where n is the real and k is the imaginary part). By investigating the relationship between volcanic ash composition and refractive index, a new parameterisation has been developed which will aid in the detection and quantification of hazardous ash clouds. It has been tested on retrievals from three recent eruptions using Infrared Atmospheric Sounding Interferometer (IASI) satellite data. The eruptions of Chaitén (Chile) in May 2008, Okmok (Aleutian Peninsula) in July 2008 and Grímsvötn (Iceland) in May 2011 allowed the testing and application of the parameterisation on a range of compositions, demonstrating that use of a parameterised index may significantly improve the retrieval of mass loading, a crucial parameter for assessing hazards to health, infrastructure and aviation. Direct sampling techniques are required to supplement satellite observations in order to ground-truth remote sensing techniques. A study of aerosol samples collected in the UK when the ash plume of Eyjafjallajökull was overhead has demonstrated that volcanic ash is chemically detectable above urban particulate matter, and that ash surface chemistry plays an important role in transporting heavy metals, which may have implications for remote sensing.

Extended Abstract

Lack of information on the physical, compositional and optical characteristics of volcanic ash and properties that affect its residence time, aggregation and interaction with other atmospheric species represents a major gap in basic knowledge and understanding of volcanic ash in the atmosphere. The eruption of Eyjafjallajökull volcano, Iceland, in April and May 2010 highlighted the importance of understanding the behaviour and influence of volcanic ash in the atmosphere and brought attention to some key areas that lacked knowledge. Since 2010 there have been significant efforts to close this gap. In particular, the microphysical, chemical and morphological characterisation of volcanic ash has been a focus. A comprehensive database of information for dispersion models, used in assimilating satellite data and forecasting the movement of ash clouds, can provide useful data for hazard assessments (e.g. human, animal and plant health impacts) and at a fundamental level provide new information for studying volcano-climate interactions (e.g. ash veils, ash-ice albedo feedback, ocean fertilisation). New measurements of volcanic ash characteristics are also very valuable for satellite retrievals that rely on assumptions of the optical properties, size distribution and morphology of ash particles. The overall aim of this research is to fill an important gap in our understanding of the atmospheric habit of fine volcanic ash.

The bulk and glass compositions of volcanic ash samples with known spectral complex refractive indices were characterised in terms of SiO_2 content and the ratio of non-bridging oxygens to tetrahedrally-coordinated cations (NBO/T). The bulk ash chemistry was demonstrated to have a stronger influence on the spectral complex refractive index compared to the glass chemistry, indicating chemical heterogeneity down to very

fine (sub-micron) size fractions. At visible wavelengths, n correlates better with bulk ash composition than with glass composition. This is true for both SiO_2 and NBO/T. Generally, k correlates better with SiO_2 content than NBO/T. Over a broader spectral range (0.4–19 μm), bulk ash composition correlates better than glass composition. The NBO/T generally correlates better than SiO_2 content for both parts of the refractive index, and this is due to the fact that NBO/T maps onto a salient feature in the silicate glass structure; the tetrahedral bond length. In order to understand the impacts of the new parameterisation on satellite retrievals, mass loading retrievals from the Infrared Atmospheric Sounding Interferometer (IASI) satellite (wavelengths 3.62–15.5 μm) using our new approach were compared with retrievals that assumed a standard (Eyjafjallajökull) ash refractive index. There are significant differences in mass loading using our calculated indices specific to ash type rather than a standard index. Where mass loadings increase, there is often improvement in retrieval quality (corresponding to cost function decrease). This new parameterisation of refractive index variation with ash composition will help to improve remote sensing retrievals for the rapid identification of ash and quantitative analysis of mass loadings from satellite data on operational timescales. This aspect is just one piece of the puzzle in understanding the life-cycle of volcanic ash in the atmosphere.

Volcanic eruptions can impact downwind air quality in a range of different ways including potentially increasing aerosol trace metal levels. The impact on trace metal levels in urban environments has, however, received relatively little attention. In order to gain a better understanding of the fate of atmospherically transported ash, a series of aerosol samples collected in Oxford, UK during the eruption of Eyjafjallajökull have been studied. These samples, collected nearly two thousand kilometres from the source, represent the distal contribution of volcanic ash from this eruption. The aerosol samples were collected using a high-flow cascade impactor over a period from 16 April to 3 June 2010, coinciding with the detection of volcanic ash from the eruption of Eyjafjallajökull, Iceland over UK airspace. Satellite and model data suggest that the ash

was rapidly transported southeast over Europe during the first intense phase, and then travelled southwards while spreading westwards as a broad diffuse cloud over southern England. The size-segregated samples were leached in dilute (pH 1) nitric acid and the leachate analysed for Mg, Al, Ca, Ti, V, Cr, Mn, Fe, Co, Ni, Cu, Zn Sr, Mo, Cd and Pb. The dilute acid extraction used to extract trace metals from the aerosol is thought to represent the upper limit that is readily soluble in rainwater. The samples show high concentrations of Mg, Al, Ca and Ti, and elevated levels of Fe, Ni, Cu, Zn and Sr above measured urban background $PM_{2.5}$ concentrations. The elemental concentration ratios to the reference element Fe are similar to that of leachates from Eyjafjallajökull ash. This demonstrates that a volcanic signal from the event was detectable over ambient $PM_{2.5}$ concentrations in the UK. The influence of volcanic ash can have important implications for short-term health hazards due to changes in the overall composition of $PM_{2.5}$ aerosols, and implications for the supply of leachable metals into the marine and terrestrial environment. While the results can be used as important validation for models that forecast the movement of ash during the Eyjafjallajökull crisis, the methodology is quite general and will have important applications in the case of future eruptions, globally.

Contents

List of Figures

List of Tables

Chapter 1

Introduction

1.1 Volcanic ash in the atmosphere

The April 2010 eruption of Eyjafjallajökull volcano in Iceland caused the largest economic and social disruption due to volcanic ash in aviation history (Schumann et al., 2011). The consequences of this event were in part due to our lack of understanding of the behaviour of volcanic ash in the atmosphere. Fine volcanic ash ($< 63\ \mu$m diameter) can remain in the atmosphere for long periods of time and be transported great distances from the source (Cashman and Rust, 2016). Depending on its grain-size, energetics of the eruption and the atmospheric conditions, it may remain airborne for many hours, days or even months (Mastin et al., 2009) compared with larger sized tephra (mm- to cm-sized particles), which usually rain out within a few minutes (Bursik et al., 1992). Ash can be transported thousands of kilometres from its source, as evidenced by tephra deposits of ancient eruptions and by satellite observations of recent eruptions (e.g. Barton et al., 1992; Klüser et al., 2013). If volcanic ash enters the jet stream, transport of the plume may be enhanced, posing a significant hazard to aircraft (Bursik et al., 2009), which often utilise the jet stream for fuel economical purposes. This makes effective detection and tracking of volcanic ash in the atmosphere incredibly important. Satellite remote sensing of ash provides a vital tool in understanding and mitigating these hazards (Prata, 2016) and new technologies are currently being investigated to provide aircraft with on-board detection methods (e.g. Prata et al., 2016). Satellite remote sensing of ash requires information on the spectral extinction coefficient, spectral single

scattering albedo and phase function. An understanding of how these optical properties relate to the physical and compositional characteristics of ash will allow more accurate retrievals from satellite data (Prata, 1989; Wen and Rose, 1994; Prata and Grant, 2001). The composition, size distribution, shape and number of ash particles in eruption clouds govern the interaction with radiation (Clarisse and Prata, 2016) and influence the potential effects on the environment and climate (Durant et al., 2010). Measurements of the physical, compositional and optical properties of fine ash are needed as input for radiative transfer models and dispersion models (e.g. Costa et al., 2006) that help to model the impacts of volcanic ash on the atmosphere, climate, health and aviation.

1.1.1 Ash transport and dispersal

In order to predict the fate of airborne volcanic ash using dispersion modelling, some key source parameters must be known. These include: the mass eruption rate (MER), the height of the eruption column, the total grain-size distribution (TGSD) and certain microphysical properties that determine the behaviour of ash as it is transported through the atmosphere. Most of the variability in model outputs results from variation in the description of the source term between the different models. The relationship between some of these parameters can be quantified but many need to be observed. For example, an empirical relationship exists between MER and column height, but this relationship is not well understood for columns that are bent over (weak plumes) and not sustained (e.g. Woodhouse et al., 2013). Sparse data on grain-size prevent a thorough assessment of its relationship with other immediately observable parameters such as plume height (Mastin et al., 2009). The eruption of Eyjafjallajökull demonstrated the urgent need for better data on these key parameters. In response, the Civil Aviation Authority introduced recommendations for air-traffic in European airspace defining three new ash-contamination zones based on concentration: 0.2–2 mg/m^3, 2–4 mg/m^3 and 4 mg/m^3 (ICAO, 2016). These zones must be determined from forecast modelling, which in turn requires input source parameters. The use of sparse data to extrapolate

ash deposition in distal settings can be unreliable due to uncertainties in the TGSD (e.g. Watt et al., 2009; Beckett et al., 2015). If the initial size distribution is incorrect, then it is very likely that the model predictions will not be accurate and the delineation of the ash-contamination zones will be incorrect. Thus, effective hazard mitigation requires better information on the physical properties of volcanic ash and how they are related to observable plume dynamics.

There are also other benefits of obtaining better information on volcanic ash. For ancient eruptions, all that is left behind are the deposits. Relating these back to the eruption style and intensity requires knowledge of how the characteristics of ash deposits are related to ash transport and deposition. Ash deposition maps could be improved by obtaining better and more comprehensive information on volcanic ash. Our understanding of effects like phytoplankton blooms initiated by ash falling into iron-deficient ocean water (Duggen et al., 2010; Langmann et al., 2010b; Ayris and Delmelle, 2012) and associated effects on fisheries could benefit from this. Likewise, the potential effects of diminishing the albedo of snow and ice-covered surfaces due to ash deposition could be better assessed.

On a fundamental level, these effects of ash on the earth system may lead to a better understanding of how volcanic ash can change the radiation balance of the earth-atmosphere. For example, a large super-volcanic eruption that results in a continent-sized ash blanket may affect climate due to the high albedo of the ash (like snow) and through altering precipitation patterns, in particular the El Niño Southern Oscillation (Jones et al., 2007). More generally, the impacts of volcanic ash are complex and may be manifest through ash veil shading (cooling), ash-ice albedo feedback (warming), and ash-ocean interaction (fertilising), which on a large scale could lead to CO_2 drawdown (Watson, 1997), providing an air-conditioning mechanism for a climate warmed by CO_2. While volcano-climate interactions have been studied in some detail (e.g. Robock, 2015), these studies have mostly focused on stratospheric aerosols (from SO_2 conversion to sulphate) and on the changes to atmospheric dynamics that result, and

comparatively little work has been done on the effects of ash particles on the earth system.

1.1.2 Sedimentation processes

Removal of volcanic ash from the atmosphere is another important process that is poorly understood (Langmann et al., 2010a; Brown et al., 2012). Observations of distal mass deposition maxima indicate that fine ash tends to settle out at a faster rate than predicted from single-particle terminal fall velocities. This could be due to hydrometeor formation, which enhances aggregation, or due to convective instabilities such as the formation of mammatus (e.g. Mt St Helens) on the underside of volcanic clouds (Durant et al., 2009). Tracking of the deposition of ash from the eruption of Chaitén in 2008 using a combination of satellite and field data has highlighted the complexity of depositional processes within a single eruption. The deposit revealed a bimodal size distribution providing evidence for cloud aggregation processes (Watt et al., 2009). Dry and wet aggregation processes are not yet well understood (Brown et al., 2012), and they are currently not included in the physics of any operational dispersion models, although efforts are underway to bring models that do include aggregation (e.g. Marti et al., 2017) into operation. This has important implications for predicted airborne ash concentrations and for predicted fallout.

The lack of observational and laboratory data highlight a significant gap in our knowledge. One aspect of this, that makes observations of ash aggregation difficult, is the wide range of grain-size over which this process acts. No single remote sensing technique or field method can detect the full range of particle sizes which means that incorporation of data from multiple techniques must be employed (Brown et al., 2012). Another reason for sparse observational data on distal ash deposits is that many eruptions result in ash dispersal over the ocean. Ash from the June 2011 eruption of Puyehue-Cordón Caulle in Chile circumvented the globe in significant enough concentrations to cause disruption to air travel in Australia (Klüser et al., 2013). Much of the

ultra-distal ash from this eruption will have been deposited over the oceans, making observation of the resulting deposits impossible. For eruptions like this, especially in the southern hemisphere—an area mostly covered by ocean—we must rely on remote sensing techniques. Improvements in satellite detection and retrieval of ash properties will be extremely valuable to our understanding of the long-range transport and fate of fine volcanic ash.

1.1.3 Impacts of volcanic ash

The transport and deposition of atmospheric aerosols into the marine environment are an important source of trace metals to the surface ocean and can have important implications for ocean biogeochemistry (Jickells et al., 2005). Volcanic emissions are an important source of trace metals to the surface ocean (Browning et al., 2015). Atmospheric trace metals such as Fe, Zn and Co are required for phytoplankton growth (Dixon, 2008; Saito and Goepfert, 2008), while others, such as Cu, can be toxic (Paytan et al., 2009; Jordi et al., 2012). In particular, volcanic ash has the potential to release large amounts of Fe into the marine environment (Duggen et al., 2010; Langmann et al., 2010b; Olgun et al., 2011). If ash fallout occurs over nutrient-limited waters, the addition of Fe can "fertilise" the ocean and lead to phytoplankton blooms (e.g. Browning et al., 2014). Leaching of Fe from volcanic aerosols occurs rapidly through the dissolution of Fe-bearing surface salts (Frogner et al., 2001; Jones and Gislason, 2008). The solubility of Fe and hence, its bioavailability, is strongly influenced by Fe-speciation in the ash bulk and surface composition, and depends on the duration of contact with acids before deposition into the ocean (Hoshyaripour et al., 2014; Maters et al., 2017).

The respiratory health hazards of volcanic ash have been extensively studied and summarised in a comprehensive review by Horwell and Baxter (2006). The characteristics of ash that make it hazardous to human health are: the crystalline silica content, the presence of bio-toxic elements and compounds, and the surface chemistry of the particles. The extent to which these can affect respiratory health is predominantly

influenced by the size, shape and surface area of the particles. Particles with an aerodynamic diameter < 10 μm (PM_{10}) are classed as 'thoracic' and can be inhaled into the trachea and bronchi. Particles below < 4 μm (PM_4) are classed as 'respirable', meaning they can get as far as the alveoli, where the gas exchange occurs and where they have the greatest potential for toxicity. Therefore, characterising the proportion of these size fractions is very important when assessing the respiratory hazard of volcanic ash (Horwell, 2007). For example, the proportion of respirable ash (PM_4) from Eyjafjallajökull ranged from 2–13 vol% whereas Grímsvötn was < 3.5 vol% (Horwell et al., 2013). Horwell et al. (2013) also found the ash from Grímsvötn had a lower surface area (< 0.6 m^2/g) than that of Eyjafjallajökull (0.3–7.7 m^2/g). Laser diffraction analysis is the most time-efficient and robust technique used to measure grain-size and is typically sensitive to particles in the range 0.1–2000 μm equivalent spherical diameter. The method uses either Mie or Fraunhofer light scattering theory with an assumed complex refractive index for the ash, highlighting the importance of knowing it accurately.

Ash fall can cause significant damage to buildings and infrastructure. The impact and severity of such damage is dependent on both the ash characteristics and environmental conditions. The extent and severity of damage to buildings is influenced by the nature of the structure (e.g. flat or slanting roofs) and the the density and thickness of the ash load, which are affected by the composition and size of the tephra particles, the compaction of the layer and its wetness (Spence et al., 2005). The impacts to critical infrastructure systems have been reviewed by Wilson et al. (2012b), defining 'critical infrastructure' as 'assets that are essential for the functioning of a society and economy'. This encompasses: electricity, water supplies, wastewater, land and air transport and telecommunications. The main impacts of ash on each of these (from Wilson et al., 2012b) are summarised below:

- ***Electricity*** — fine ash adheres to substation insulators causing unintended electrical discharge ('flashover') resulting in widespread outages. Ash conductivity is

increased when wet due to mobilisation of surface salts. Wet ash is also heavier than dry ash and can cause structural damage to electricity lines.

- ***Water supply***–ash can damage and block water pipes; water quality through leaching of toxic elements into the supply (e.g. fluoride; Witham et al., 2005), water acidification, and increased suspended particle load (turbidity), which can stimulate bacterial growth; and water shortages due to increased demand from the cleanup of ash (e.g. the 1992 eruption of Mt Spurr, Alaska).

- ***Wastewater***—blockage of sewage and stormwater drainage can cause flooding. Ash getting into wastewater treatment facilities can be particularly expensive causing abrasion damage to moving parts and clogging filtration systems.

- ***Land transport***—transportation networks can be severely impacted by ash fall due to reduced visibility and reduced traction on paved surfaces. Vehicles are vulnerable as ash can clog filters and brake systems, and abrade moving parts.

- ***Air transport***—the hazards to aviation have been reviewed by Casadevall (1994) and more recently by Prata and Tupper (2009). The main hazard for aircraft is ingestion of atmospheric volcanic ash potentially causing in-flight engine failure (e.g. the British Airways Flight 9 encounter with ash from the 1982 eruption of Galunggung, Indonesia). Damage to due to ash abrasion is also of concern for longer-term performance and maintenance of aircraft (Clarkson et al., 2016). The financial impact to the airline industry during the Eyjafjallajökull eruption was estimated to be €3.3 billion (Mazzocchi et al., 2010). Airports are also impacted in a similar way to ground transportation, due to decreased visibility and vehicular damage (Guffanti et al., 2009). Recent work to quantitatively assess the hazard to jet engines has found the proportion of glassy and crystalline components of ash (e.g. Song et al., 2016), as well as concentration (e.g. Clarkson et al., 2016), to be of critical importance.

- ***Telecommunications***—there have been no reports of signal attenuation or interference from ash fall (other than from plume-generated lightning) in the past 20 years. Telecommunications equipment, however, can be vulnerable due to overheating from ingestion of ash into ventilation and cooling systems. Laptops appear to be relatively resilient to ash exposure, with little or no permanent damage, other than problems with keyboards (Wilson et al., 2012a).

1.2 Outline and aims of this thesis

A major motivation of this study is to help reduce the economic and societal impact of ash by improving techniques to detect ash in the atmosphere and improve our understanding of the environmental impacts of distal ash. A better understanding of the behaviour of ash in the atmosphere can help assess hazards, model climate effects, and model ancient eruptions, which can give us insight into future hazards of potentially active volcanoes. The main aims of this thesis are to: (1) investigate the relationship between volcanic ash composition and optical properties, (2) develop a parameterisation in order to estimate the complex refractive index using ash composition and test its application to satellite retrievals, and (3) investigate the aerosol trace metal contribution of distal volcanic ash.

This thesis is structured around three main chapters:

- Chapter 2: Provides a review of the remote sensing of volcanic ash and the properties relevant to its detection and quantification

- Chapter 3: Develops a parameterisation of spectral complex refractive index based on the composition of volcanic ash, and investigates the usefulness of its application with three test cases, the eruptions of Chaitén (May 2008), Okmok (July 2008) and Grímsvötn (May 2011)

- Chapter 4: Investigates the atmospheric trace metal contribution of aerosols collected in the UK during the Eyjafjallajökull eruption in order to better understand

ash in the distal environment

Finally, Chapter 5 summarises the main conclusions from each chapter, and synthesises the major findings of the thesis. Recommendations for further work are provided.

Chapter 2

Remote sensing of volcanic ash

This chapter provides a broad overview and background to the remote sensing of volcanic ash in the atmosphere. It is based on:

Prata, F., & Prata, G. (2015). Remote sensing of volcanic ash and sulfur dioxide. In A. Schmidt, K. Fristad, & L. Elkins-Tanton (Eds.), ***Volcanism and Global Environmental Change*** (pp. 97-114). Cambridge: Cambridge University Press.

Author contributions: F.P. and G.P. each wrote 50% of the underpinning publication. G.P. processed and analysed the data used to produce Figure 2.1. The retrieval for Figure 2.4 was done by F.P. and was interpreted by G.P.

This chapter represents the part authored by G.P., which is an extract of the original publication, and has been expanded on to include additional figures (Figures 2.2 and 2.3) and a review of hyperspectral instruments relevant to the work presented in this thesis (Section 2.4.2).

Work from this chapter also contributed to the publication (included in Appendix A):

Prata, A. J. et al. 2016. Artificial cloud test confirms volcanic ash detection using infrared spectral imaging. ***Sci. Rep.*** **6**, 25620; doi: 10.1038/srep25620.

2.1 Introduction

Volcanic ash is the term given to anything ejected from a volcano that is less than 2 mm in diameter. Volcanic ash encompasses a wide variety of compositional types, size distributions and shapes. Particle size and the size distribution is related to the energetics

of the eruption (Heiken and Wohletz, 1985; Zimanowski et al., 2003). Sub-micron sized particles are present in every eruption and are often found adhering to larger particles. The style of magma fragmentation (e.g. magmatic vs. phreatomagmatic) influences the shape of the resulting ash particles (Sigurdsson et al., 2015). Ash particles are very rarely spherical, and shapes can range from equant blocky fragments to angular cusps formed from broken bubble walls. The composition of volcanic ash can be highly heterogeneous, and typically contains a mixture of glass and crystal fragments, and lithic (rock) components that were entrained in the magma, originating from, for example, the surrounding country rock or walls of the volcanic conduit (De Rosa, 1999). The glass particles may themselves contain phenocrysts (large crystals), microlites (micro-crystals) and bubbles formed by the exsolution of magmatic volatile phases. A backscattered electron (BSE) image of a volcanic ash sample from the May 2010 Eyjafjallajökull eruption (Figure 2.1) shows that the fragments vary in composition, have irregular shapes and occupy a variety of sizes from a few microns up to 0.5 mm.

All of these properties influence how ash is transported and how long it remains in the atmosphere. They also influence how electromagnetic radiation is transmitted, absorbed and scattered when it interacts with a cloud of ash particles. Having an understanding of this relationship allows us to retrieve information on these properties using various remote sensing techniques summarised in Prata (2016) .

2.2 Microphysical properties

The physical attributes relevant to remote sensing of fine ash, defined here as particles with diameters $< 63\ \mu$m, include the size distribution and composition, with less importance on shape. The spectral region between 8 and 12 μm has mainly been exploited to infer fine-ash properties, but limits the range of particle radii that can be retrieved to between 1–16 μm. There are few measurements of the size distribution of ash while resident in the atmosphere and so this often has to be determined from deposits on the

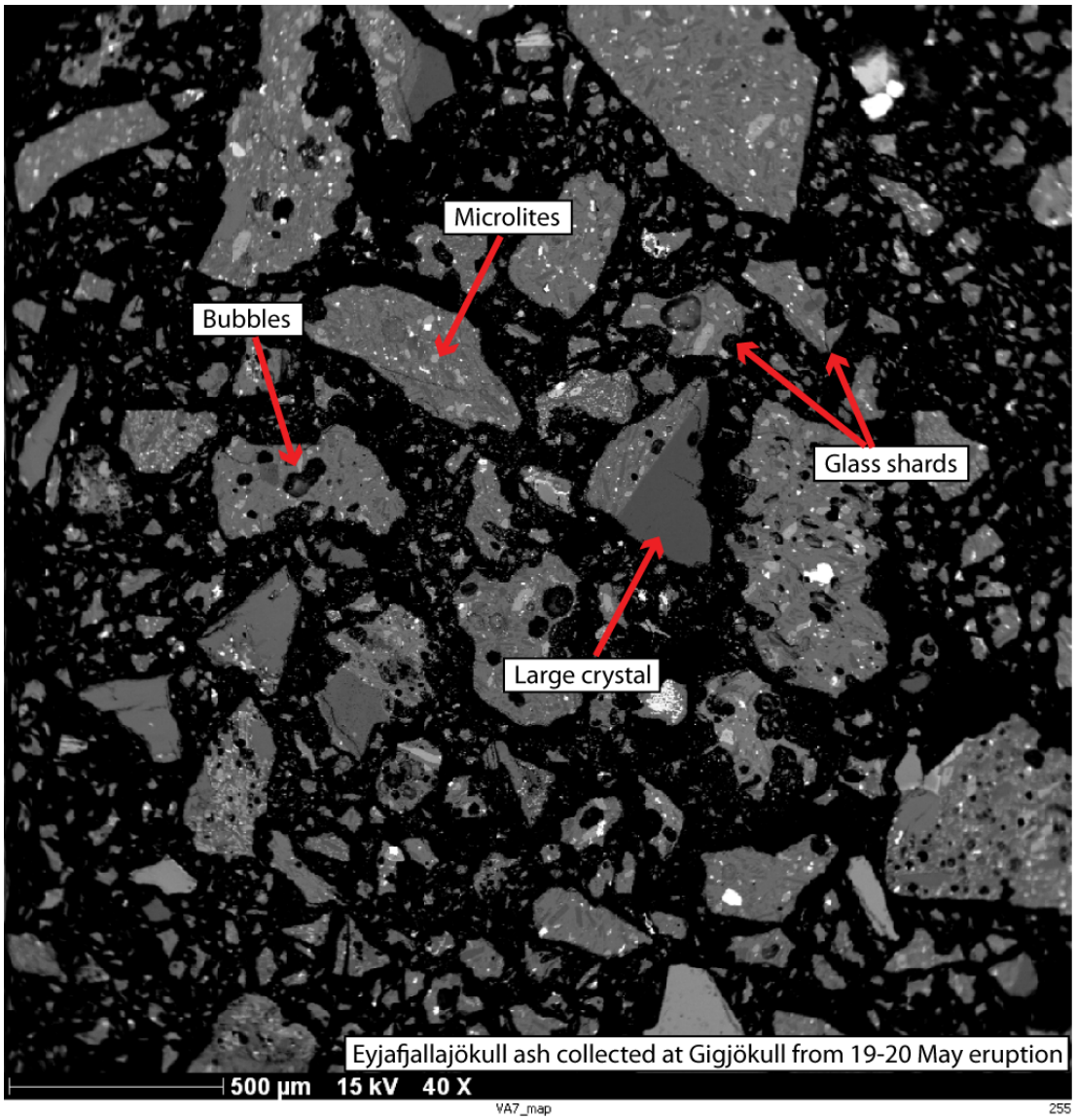

Figure 2.1: Backscattered electron image of volcanic ash from Eyjafjallajökull volcano from May 2010 showing the range of different components ash can be made up of. The greyscale level represents differing densities, with brighter shades indicating higher density (high atomic weight), and darker shades representing lower density (low atomic weight). ***This figure has been reproduced from Prata and Prata (2015).***

ground, which is not a satisfactory situation. Some airborne data exist from the Mt St Helens eruptions of May 1980 (Hobbs et al., 1981) and from the recent eruptions of Eyjafjallajökull (Schumann et al., 2011) and Grímsvötn (Vogel et al., 2012) in Iceland. These data suggest a bimodal size distribution with peaks near to 0.5 μm and 3–6 μm radius and have been modelled mathematically using gamma and log-normal distributions. There is very little experimental evidence of significant amounts of ash with particle radii > 50 μm. There are measurements of the composition of fine ash, e.g. Gíslason et al. (2011), Lieke et al. (2013); for the purpose of remote sensing in the infrared the most salient feature is the per cent composition of SiO_2, since this molecule exhibits characteristic absorption features through the range 8–12 μm. Shape does affect the radiative transfer of light interacting with particles. The error caused by assuming spherical particles, rather than more realistic ragged, agglomerates with asperities, is mostly seen in the retrieval of the mass loading.

The optical regime governing how radiation interacts with a particle depends on both the wavelength (λ) and particle size (r). Models of light scattering can be divided into different optical regimes depending on the size of the particle relative to the wavelength of light. To incorporate this, we describe particle size in terms of a dimensionless number known as the size parameter (X).

$$X = \frac{2\pi r}{\lambda} \tag{2.1}$$

where r is the particle radius and λ is wavelength. These optical regimes are:

- Rayleigh — the particle is small compared to the wavelength ($X < 1$)
- Mie — the particle is of comparable size to the wavelength ($X \approx 1$)
- Geometric — the particle is larger compared to the wavelength ($X > 1$)

As the size distribution of particles influences the way in which a cloud of particles interacts with radiation, it is necessary to characterise the shape of different size distributions and investigate how this affects optical parameters such as single scattering

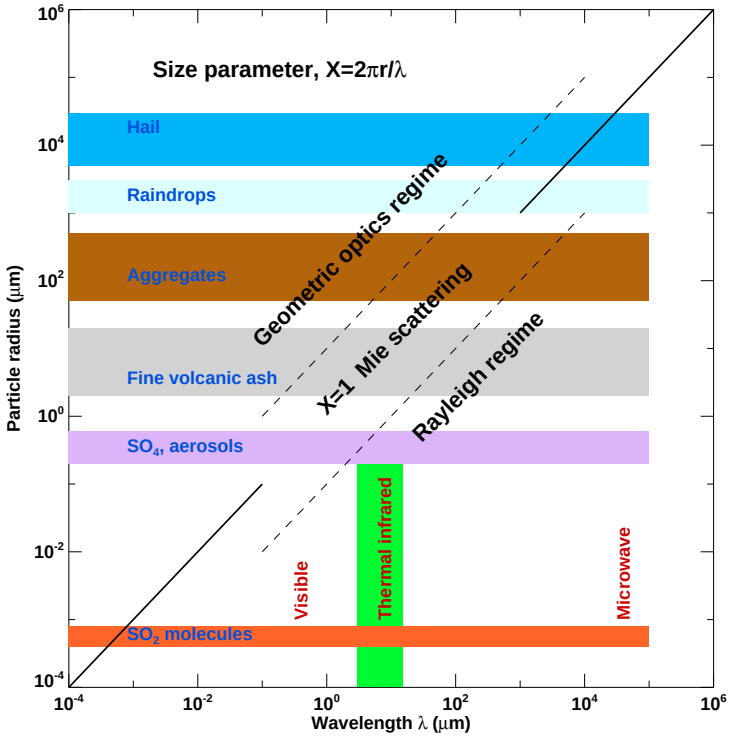

Figure 2.2: Illustration of the optical regimes governing how radiation interacts with a particle according to its size and the wavelength of radiation. ***Modified from Petty (2006)***.

albedo, mass absorption coefficient and phase function. The size parameter is useful for determining which optical regime describes how electromagnetic radiation will interact with the particles, and guides the choice of wavelength to use for retrievals of ash properties (Figure 2.2).

Distal particle size distributions rarely fit a log-normal distribution and are often polymodal. They typically show a coarser sub-population which shifts to finer sizes and decreases in proportion with increasing distance from the vent as the cloud is transported downwind due to coarser particles settling out. As distance from the volcano increases, settling transitions from inertia-dominated single-particle settling to aggregation-dominated settling of very fine (< 30 μm diameter) ash particles (Rose and Durant, 2009). Nevertheless, it is these particles that remain in the atmosphere for longer and present a hazard to air traffic and human health (Horwell and Baxter, 2006). The mass proportion of very fine ash (< 30 μm diameter) in explosive eruptions can vary from a few per cent (typical for basaltic eruptions) to greater than 50% (in some

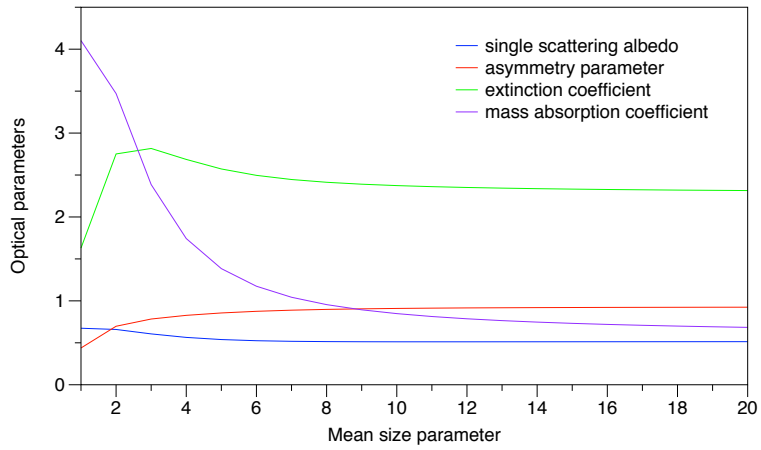

Figure 2.3: Optical parameters single scattering albedo, asymmetry parameter, extinction coefficient and mass absorption coefficient modelled for varying mean size parameter using Mie theory. Note: the units for mass absorption coefficient are m^2/g, which enables the retrieval of mass.

silicic eruptions). In distal regions, this finer sub-population typically retains consistent size characteristics but becomes proportionally dominant. The effect of size parameter (and therefore particle size) on various optical parameters can be modelled using Mie theory by varying the mean size parameter and standard deviation from the fitted distribution (Figure 2.3). This is analogous to shifting the size range of the distribution but maintaining its shape.

2.3 Optical properties

To retrieve fine-ash properties from remote sensing it is necessary to have knowledge of the spectral complex refractive index of ash. The amount of absorption of light by the particle is controlled by the imaginary part of the refractive index (k), which is strongly dependent upon wavelength and composition. The absorption coefficient α (m^{-1}) can be expressed as

$$\alpha = \frac{4\pi k(\lambda)}{\lambda} \tag{2.2}$$

The compositional effects are manifest through the spectrally dependent refractive index. Several efforts are underway to improve the measurement database of optical

properties of volcanic ash (e.g. Ball et al., 2015; Reed et al., 2018; Vogel et al., 2017; Rocha-Lima et al., 2014). These data feed directly into Mie scattering models that provide the relevant optical parameters such as the asymmetry parameter, the single-scattering albedo and extinction efficiencies that are needed as input to the radiative transfer codes.

2.4 Satellite retrievals

Infrared remote sensing of volcanic ash was first developed by Prata (1989) who recognised that two channels within the region 8–13 μm could be used to discriminate volcanic ash from meteorological water/ice clouds. Subsequent work by Wen and Rose (1994) showed how to determine mass loadings and effective particle size by using microphysical models and the optical properties of idealised (spherical) ash particles. Further refinements and improvements have been made by Prata and Grant (2001), Pavolonis et al. (2006), Pavolonis (2010), Clarisse et al. (2010) and Prata and Prata (2012). The determination of mass loading and effective particle radius relies essentially on two pieces of independent information, the brightness temperatures at two wavelengths (most often at 11 μm and 12 μm), and two ***a priori***—a microphysical model and a radiative transfer model. Different schemes have been proposed to invert the brightness temperature measurements into the required geophysical parameters and here we give a graphical explanation of the retrieval of ash from infrared measurements.

2.4.1 Methods

The panels of Figure 2.4 show the brightness temperatures* at 11 μm (T_{11}) and 12 μm (T_{12}) and the temperature difference, $\Delta T = T_{11} - T_{12}$ for a MODIS (MODerate resolution Imaging Spectrometer) Terra image acquired on 8 May 2010 during the eruption of Eyjafjallajökull. There is a plume emanating from Eyjafjallajökull dispersing southwards that can be seen in the T_{11} and T_{12} images and more clearly in the difference

*Brightness temperature is defined as the temperature obtained when using the monochromatic measured radiance in the inverse Planck function.

image (lower left panel). The last panel shows a retrieval of mass loading based on these data, a microphysical model of the ash and a radiative transfer model. Note that the retrieval is shown for just three levels: 0.2, 2 and 4 g/m^2.

The mass loading (and concentration for a 1-km-thick cloud) can be determined from the following simplified expression:

$$m_l = \frac{4}{3}\rho\frac{\tau(\lambda)r_e}{Q_{ext}(\lambda)}, \tag{2.3}$$

where τ is the infrared optical depth, r_e is the effective particle radius, ρ is the density of the ash, Q_{ext} is the extinction efficiency and λ is the wavelength. It is possible to simplify further by assuming that the optical depth is equal at the two infrared wavelengths used; then we may write,

$$\tau = -\ln\left[1 - \frac{T_s - T_b}{T_s - T_c}\right] \tag{2.4}$$

where T_c is the cloud-top temperature, T_s is the surface temperature and T_b is the brightness temperature in one of the channels. The term $T_s - T_c$ is often referred to as the thermal contrast and it can be seen that this should be large, while T_s should be larger than the cloud-top temperature. These conditions may be interpreted as implying that retrieval of τ is best for semi-transparent clouds where the ash cloud has a temperature different to that of the surface below. For very transparent clouds (i.e. dilute clouds), $T_b \to T_s$ and retrieval becomes problematic. Likewise, as $T_b \to T_c$ the cloud becomes opaque and $\tau \to \infty$. An infrared optical depth of ≈ 4 corresponds to $T_b - T_c \approx 0.5$ K and may be considered a limiting value for most infrared satellite sensors. For an optically thick ash cloud with $\rho \approx 2.5 \times 10^6$ g/m^3, $Q_{ext} \approx 2.5$, $r_e \approx 5\,\mu$m, the mass loading $m_l \approx 20$ g/m^2, while for an optically thin ash cloud, with $T_s - T_b \approx 0.5$ K, $\tau \approx 0.01$, and with the same values as before, $m_l \approx 0.15$ g/m^2. In practice, the lower limit has been found to have the slightly higher value of $m_l \approx 0.2$ g/m^2 (Prata and Prata, 2012). An important point to note here is that it is the infrared opacity that matters; ash clouds with large particles outside the sensitivity range are easily detected.

In summary, these simple calculations show that satellite infrared remote sensing of volcanic ash clouds can be used to determine mass loadings within the broad range of 0.2 to 20 g/m^2 and, for a 1-km-thick ash cloud, this covers the entire range of concentrations of concern to aviation (***viz.*** 0.2, 2 and 4 mg/m^3 and higher).

2.4.2 Hyperspectral techniques

Hyperspectral instruments measure radiances at thousands of narrow wavelength intervals, rather than in just a few broadband channels, resulting in much higher spectral resolution measurements. The advantage of the higher resolution spectral information is that gases and particles of interest can be targeted with less interference from other gases, such as water vapour. At present there are only four instruments in routine operation; the Atmospheric Infrared Sounder (AIRS), the Infrared Atmospheric Sounding Interferometer (IASI), the Tropospheric Emission Spectrometer (TES) and the Cross-track Infrared Sounder (CrIS), which is somewhat limiting, however this is likely to increase in the future (see Table 14.1 in Prata, 2016). To fully utilise the high resolution spectral information contained in the data collected by these instruments, more advanced physical and statistical ash detection methods have been developed. The various approaches are summarised in Clarisse and Prata (2016) and include: maximum likelihood singular value decomposition (SVD)/principle component analysis (PCA); linear discrimination analysis (LDA); and distance approaches, e.g. the concavity index (Gangale et al., 2010) and the ash correlation method (Clarisse et al., 2010). The higher resolution not only allows better detection and greater sensitivity to target gases and particles but has also revealed the possibility to discriminate between different ash types, i.e. compositional information. The concavity method, in particular, can essentially distinguish between basaltic, andesite and rhyolitic ash compositions by the shape of the brightness temperature spectra in the wavelength region of 8–12 μm. The more silicic end-members display a more concave shape than the mafic end-members. An advantage of the concavity method is that it works particularly well for optically thin

clouds, i.e. aged ash clouds, and so there may be a possibility to track the compositional evolution of a cloud in a qualitative sense. This was suggested at the ESA–EUMETSAT workshop on the 14 April to 23 May 2010 eruption at the Eyjafjöll volcano, South Iceland (ESA/ESRIN, 26–27 May 2010) (Zehner, 2012), although no work has yet been published demonstrating an observed change in the concavity index from remote sensing for this particular eruption.

Another advantage of utilising higher resolution data from hyperspectral sounders is the possibility to retrieve refractive index, and hence composition, from satellite measurements. This was recently demonstrated by Ishimoto et al. (2016) who were able to retrieve the imaginary parts of the refractive index for 10 ash clouds using hyperspectral AIRS data. The observed brightness temperatures depend on optical depth, cloud height and effective particle radius in addition to refractive index. Ishimoto et al. (2016) based their refractive index retrieval on forward modelling the radiative transfer of the complex refractive indices of samples from Pollack et al. (1973) and their mixtures. Thus, the accuracy of the retrieval is dependent on the assumption that those measurements are appropriate for volcanic ash. The success of this approach, in addition to the underlying assumption, provides further incentive to better characterise the refractive index of volcanic ash itself, which has been shown to have different optical characteristics than that of volcanic rock in the infrared region (e.g. Reed et al., 2018).

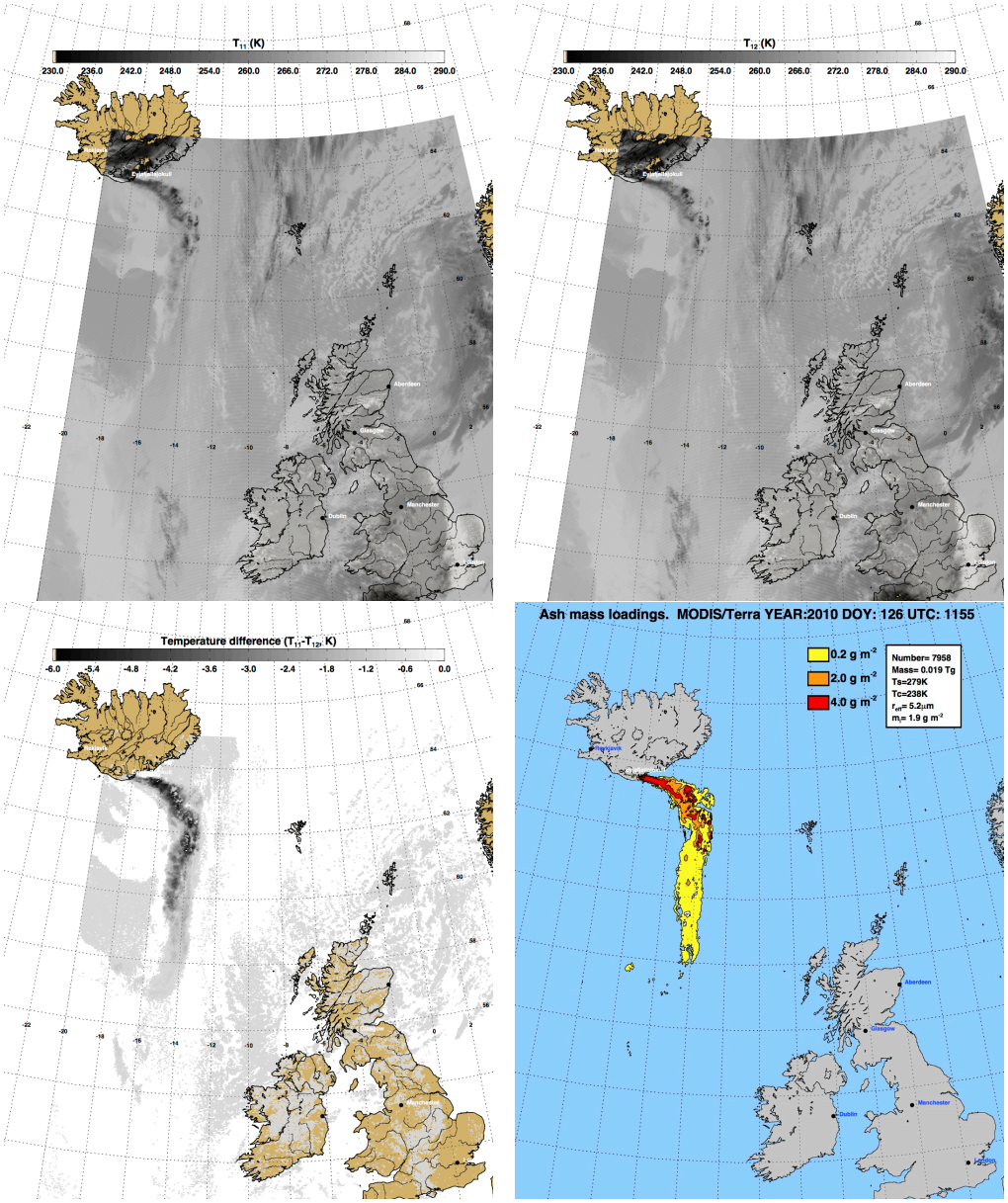

Figure 2.4: ***Top left:*** MODIS 11 μm brightness temperature image. ***Top right:*** MODIS 12 μm brightness temperature image. ***Bottom left:*** MODIS 11–12 μm brightens temperature difference image. ***Bottom right:*** Mass loading retrieval based on the MODIS brightness temperature data. The MODIS/Terra image acquired was acquired on 8 May 2010 at 11:55 UTC. ***This figure has been reproduced from Prata and Prata (2015).***

Chapter 3

Composition and the complex refractive index

This chapter presents a new dataset of volcanic ash compositions and explores their relationship with the spectral complex refractive index, the importance of which has been highlighted in the previous chapter. A new parameterisation of volcanic ash complex refractive index based on composition is proposed and tested in retrievals using satellite data from the Infrared Atmospheric Sounding Interferometer (IASI).

A manuscript based on this chapter has been submitted for publication and is currently under review:

Prata, G. S., Ventress, L. J., Carboni, E., Mather, T. A., Grainger, R. G. & Pyle, D. M. "A new parameterisation of volcanic ash complex refractive index based on NBO/T and SiO_2 content". ***Journal of Geophysical Research: Atmospheres***.

Author contributions: G.S.P. processed and analysed and the bulk and glass chemistry of the ash samples, and developed the parameterisation. Satellite retrievals were performed by L.J.V. and E.C., and G.S.P. interpreted the results. T.A.M., D.M.P. and R.G.G. advised on interpretation of results and gave input into drafts of the manuscript.

3.1 Introduction

Satellite retrievals of volcanic ash clouds are important for hazard assessment and the understanding of volcanic processes. At present, there are limited data available on the optical properties of different ash types, and no systematic way of predicting optical

properties for unknown samples. Fine volcanic ash (< 63 μm diameter) makes up between a few percent to over 50% of the mass proportion in explosive eruptions (Rose and Durant, 2009) and is typically composed of a mixture of silicate glass particles and crystals. The atmospheric residence time of fine ash, depending on its grain-size and atmospheric conditions, may range from hours to weeks or months (Cashman and Rust, 2016). Satellite observations from eruptions in the southern hemisphere (Barton et al., 1992; Klüser et al., 2013) have demonstrated that ash plumes can be transported for thousands of kilometres downwind. Long residence times and long-range transport of volcanic ash may have significant implications for aviation far from the volcanic source (Casadevall, 1994; Prata, 2009) and for this reason it is important to be able to reliably retrieve ash mass loading from remote sensing data. In order to detect and quantify the properties of an ash plume using satellite remote sensing, knowledge of the optical properties of volcanic ash is necessary. These optical properties are governed by the complex refractive index ($n + ik$). Both real (n) and imaginary (k) components are required to retrieve quantitative estimates of mass loading from satellite images and hence concentrations (if the cloud thickness is known or assumed). The top of atmosphere radiation, measured by imaging and sounding instruments on board satellites, is also dependent on the particle size distribution and the shape of the particles (Clarisse and Prata, 2016).

The refractive index of volcanic glass is principally controlled by its composition; a feature that has previously been utilised as a rapid way to characterise volcanic ash type (e.g. Keller et al., 1978). Pollack et al. (1973) reported complex refractive indices in the spectral range 0.21–50 μm using a combination of transmission and reflectivity measurements on polished rock slabs ranging in composition from basalt to obsidian (53.25–76.2 wt.% SiO_2). In the same year, Volz (1973) reported the complex refractive index for volcanic pumice in the spectral range of 2.5–40 μm. Previous studies of ash cloud properties using satellite retrievals from the eruption of Mt Spurr, Alaska in 1992 (Wen and Rose, 1994) and the eruption of Mt Ruapehu, New Zealand in 1996 (Prata

and Grant, 2001) found the 'andesite' refractive index of Pollack et al. (1973) to be the most suitable approximation. Most volcanic ash retrieval schemes use refractive index data from either the Pollack et al. (1973) or Volz (1973) dataset (Francis et al., 2012); however, as these are from measurements of rock slabs or pumice, neither of these are representative of natural ash particulate samples.

The challenge in measuring complex refractive indices based on transmission or reflectance spectra comes from the difficulty in estimating n, which influences scattering. Planar surfaces do not scatter as much as particles of the same material due to the presence of multiple scattering surfaces. Therefore, spectral reflectance measurements on polished slabs, such as those of Pollack et al. (1973) may significantly underestimate the influence of scattering and so underestimate the contribution of n. For this reason, measurements on dispersed particles are preferred, but this also requires accurate knowledge of the particle size distribution. Recently, new methods have been proposed which combine particle size distribution measurements to retrieve aerosol complex refractive indices from high resolution extinction spectra (Herbin et al., 2017; Reed et al., 2017).

Previous refractive index measurements of volcanic ash have been made on samples from Mt Mayon in the range of 1–16 μm (Patterson, 1975), Mt St Helens and El Chichón in the range 0.3–0.7 μm (Patterson, 1981; Patterson et al., 1983), and Eyjafjallajökull in the range 0.3–2.5 μm (Rocha-Lima et al., 2014). However, these only included the imaginary part of the complex refractive index. Measurements of both parts (n and k) have been made in the range 0.3–0.4 μm for Mt Spurr ash (Krotkov et al., 1999). Recently, Vogel et al. (2017) provided a new comprehensive dataset of volcanic ash optical and physicochemical properties in the range 0.3–1.5 μm. This dataset includes a broad range of compositions and provides a useful reference for complex refractive indices in the ultraviolet to near-infrared range, but does not include longer wavelengths (mid-infrared range) which are necessary for deriving mass loadings from the silicate absorption feature between 8–12 μm (Clarisse and Prata, 2016). Complex

refractive indices for the samples used in the present study have been presented in Grainger et al. (2013), Ball et al. (2015) and Reed et al. (2018) over a wide spectral range (0.33–20 μm). One of the main challenges in selecting an appropriate refractive index in the event of an eruption is that the volcanic ash composition is typically not known until afterwards, and composition of the cloud becomes more silicic downwind as denser crystals settle more rapidly than the glassy components (Cashman and Rust, 2016). With the exception of the new Vogel et al. (2017) dataset, to date, there are few systematic data that show how volcanic ash optical properties relate to composition The lack of a parameterisation of this kind is an important source of uncertainty in retrieval schemes (Francis et al., 2012; Mackie et al., 2014).

The spectral signature of silicates in the visible range is dominated by scattering, with only a small component of absorption; silica glass is typically transparent in this range (Kitamura et al., 2007). In the infrared, silicate absorption is dominated by a peak between 8–12 μm associated with resonances of the stretching vibration of the T–O^- bond (Kieffer, 1979; Clark, 1999; Kitamura et al., 2007; Clarisse and Prata, 2016), where T is a tetrahedrally-coordinated cation. The length of this bond determines the frequency at which radiation is absorbed, with longer bonds corresponding to lower frequencies (Kieffer, 1979; Walter and Salisbury, 1989). Bond length within the tetrahedral framework in silicate glass is influenced by the extent to which tetrahedral Si cations are substituted with other network-formers (Fe^{3+}, Al^{3+}, Mg^{2+}, P^{5+}), and by the addition of other divalent cations (Fe^{2+}, Ca^{2+}, Mg^{2+}) which act as network-modifiers breaking up the tetrahedral network (Mysen and Richet, 2005). Depolymerisation of the structure results in bond lengthening so the material absorbs radiation at progressively lower frequencies as its vibrational frequencies decrease, resulting in a shift of the T–O^- bond absorption feature towards longer wavelengths. Breaking up the tetrahedral network also results in the generation of non-bridging oxygens (NBO). The ratio of non-bridging oxygens to tetrahedrally coordinated cations (NBO/T), can be calculated from oxide weight percentages (Mysen et al., 1982). NBO/T has been shown to

be a good measure of depolymerisation (Mills, 1993; Di Genova et al., 2015) making it a useful parameter to investigate the relationship between composition and optical properties.

NBO/T has potential advantages over simply using SiO_2 content, which we will test in this study, as it allows further discrimination of absorption features between different silicate compositions. The dependence of the T–O^- bond absorption feature on the degree of silicate polymerisation has previously been used in remote sensing applications for determining rock composition in the infrared (e.g. Walter and Salisbury, 1989) and more recently in estimating composition using Raman spectroscopy (e.g. Di Genova et al., 2015). While silicate infrared absorption is the basis for the remote sensing of volcanic ash clouds, the ability to determine ash composition from infrared spectra is only beginning to be explored (Clarisse et al., 2010; Gangale et al., 2010).

In this study we characterise the compositions of a suite of volcanic ash samples and explore the relationship between composition (SiO_2 and NBO/T) and the complex refractive index measurements of the same samples reported in Ball et al. (2015) and Reed et al. (2018). We have used the Reed et al. (2018) dataset to develop an empirically based parameterisation of complex refractive index. Finally, we investigate the recent eruptions of Grímsvötn, Iceland (May 2011), Chaitén, Chile (May 2008), and Okmok, Aleutian Peninsula (July 2008) in order to assess the usefulness of our parameterisation in infrared satellite ash retrieval schemes.

3.2 Methods

3.2.1 Compositional analysis

Samples of dry-sieved volcanic ash (< 100 μm), with complex refractive index data available (Ball et al., 2015; Reed et al., 2018), were selected from a broad compositional range of eruptions (Table 3.1). Major elements for the bulk ash composition were determined by X-ray fluorescence (XRF) on fused glass beads prepared from ignited powders. Samples were analysed at the University of Leicester, Department of

Geology on a PANalytical Axios Advanced XRF spectrometer. The sample to flux ratio used was 1:5, with 80% Li metaborate: 20% Li tetraborate flux. Glass compositions were obtained by averaging electron probe microanalyses (EPMA) of glass shards with a spot size of 10 μm diameter. NBO/T was calculated for each sample from major oxide analyses according to Mysen and Richet (2005) and Giordano et al. (2008) by calculating the atomic proportions of oxygen (O) and tetrahedrally-coordinated cations (T) using the equation from Mysen et al. (1982):

$$\frac{NBO}{T} = \frac{(2 \times O)(4 \times T)}{T} \tag{3.1}$$

assuming that Si^{4+}, Ti^{4+}, P^{5+}, Al^{3+} and Fe^{3+} are in charge-balanced tetrahedral coordination. Proportions of Fe_2O_3 and FeO were estimated from total iron using ferric/ferrous iron ratios (f) suggested by Middlemost (1989) for each volcanic rock type as classified on the total alkalis versus silica (TAS) diagram. See the tables (& digital spreadsheet) provided in Appendix B for the calculation of NBO/T.

3.2.2 Refractive index measurements

The real and imaginary parts of the refractive index for these samples have been reported in Ball et al. (2015) and Reed et al. (2018). These studies used two different techniques in order to obtain the complex refractive index. Ball et al. (2015) used a direct method, the Becke Line method, to estimate the real part by immersing particles in oils of known refractive index. The particles suspended in oil are viewed through a transmitted light microscope through filters of a specific wavelength (450 nm, 546.7 nm and 650 nm). The light refracted at the edge of the particle moves into or out of the material as the stage is brought into focus; this way the real part of the refractive index can be estimated in comparison to the oil in which it is suspended. Once the real part is known, the particles can be suspended in an oil of matching refractive index and the imaginary part is estimated by measuring the intensity of the light passing through, as any attenuation will be due to absorption. See Ball et al. (2015) for a more detailed

Table 3.1: Description of Volcanic Ash Samples

Volcano	Eruption unit/date where known	Refractive index dataset
Askja[a]	Layer C 1875	1, 2
Aso	1993	1, 2
Augustine[b]	Jun 2006	1
Chaitén[c]	May 2008	1
Etna	1 Nov 2002	1
Eyjafjallajökull (a)	19–20 May 2010	2
Eyjafjallajökull (b)	15–16 May 2010	1, 2
Grímsvötn (a)	May 2011	2
Grímsvötn (b)	May 2011	1
Nisyros[d]	? > 44 Ka BP	1, 2
Okmok[e]	12 Jul 2008	1
Spurr[f]	Aug 1992	1, 2
Tongariro	2012	1, 2

Note: Samples used in Ball et al. (2015) are labelled as dataset 1, and those used in Reed et al. (2018) are labelled as dataset 2.
References where samples have previously been described are included: [a]Sparks et al. (1981), [b]Larsen et al. (2010), [c]Watt et al. (2009), [d]Longchamp et al. (2011), [e]Larsen et al. (2013) and [f]Harbin et al. (1995).

explanation. In contrast, Reed et al. (2018) used an indirect method to retrieve the complex refractive index by measuring the spectral extinction measurements over the range 0.33 – 19μm. This was done using a Fourier transform spectrometer (FTS), which covered the infrared wavelengths, and two diffraction grating spectrometers, covering the visible and ultra-violet wavelengths. The size distribution was measured concurrently using a scanning mobility particle sizer (SMPS). Knowledge of the particle size distribution allowed the complex refractive index of the particles to be obtained, once the H_2O and CO_2 gas absorption lines were removed from the extinction spectra. A detailed description of the retrieval method is given in Reed et al. (2017).

3.2.3 Parameterisation

We investigated the relationship between the complex refractive index (n and k) and bulk and glass composition (SiO_2 and NBO/T) at wavelengths 450 nm, 546.7 nm and 650 nm from Ball et al. (2015) and in the wavelength range 0.4–19 μm from Reed et al.

(2018). See Table 3.1 for the list of samples belonging to each dataset. It was not possible to separately determine the composition of the sieved < 10 μm diameter particles on which the refractive index measurements had been made, given the quantity of sample required for such measurements. Therefore, we determined the goodness-of-fit to a linear regression model using both bulk ash and glass compositions and compared the two.

3.2.4 Satellite retrieval test cases

In order to test the parameterisation, complex refractive indices (n and k) were calculated from the NBO/T of Grímsvötn, Chaitén and Okmok from our compositional dataset. These were then used to calculate optical parameters that allow the retrieval of ash mass loadings from the Infrared Atmospheric Sounding Interferometer (IASI) satellite data using the optimal estimation algorithm of Ventress et al. (2016). IASI is a nadir-viewing Fourier Transform Spectrometer measuring in the infrared (3.62–15.5 μm). Briefly, Ventress et al. (2016) implement an iterative optimal estimation retrieval algorithm to produce probable values for volcanic ash properties. Combining an infinitely thin (geometrically) ash plume with a fast radiative transfer model to simulate the ash plume, and analysing the spectra from IASI, the scheme is able to retrieve the following parameters: ash optical depth (at a reference wavelength of 550 nm), ash effective radius (μm), ash plume top height (km) and brightness temperature (K), which can be used to infer the mass loading of the plume. The results were compared with retrievals based on the Eyjafjallajökull ash refractive index used by Ventress et al. (2016). An objective cost function was used to determine whether using the calculated refractive indices provides an improvement over the use of a measured index of a different ash composition.

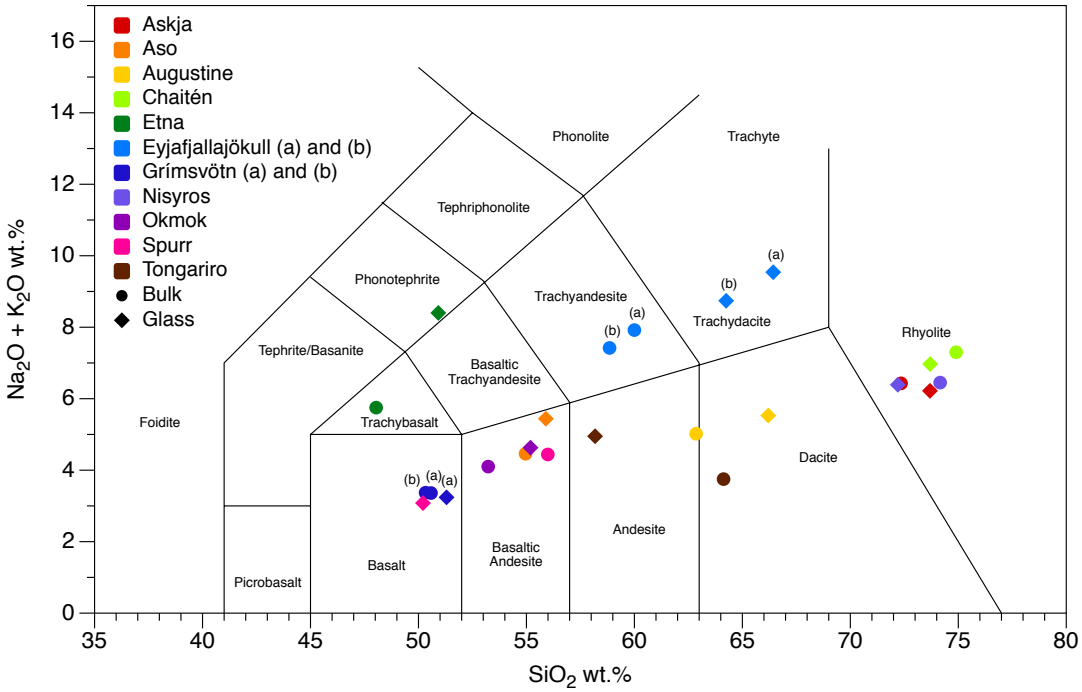

Figure 3.1: Total alkalis versus silica (TAS) diagram after Le Maitre et al. (2005). Bulk analyses for each sample are represented by circles and glass analyses are represented by diamonds. Sample details are presented in Table 3.1 and composition data in Tables 3.2 and 3.3.

3.3 Results and Discussion

3.3.1 Volcanic ash composition

Bulk ash major oxide compositions determined by XRF are reported in Table 3.2, together with the specific ferric/ferrous iron ratios (f) used for the NBO/T calculation. Glass major oxide compositions determined by EPMA are reported in Table 3.3. The suite of samples covers a wide compositional range from basalt to rhyolite (Figure 3.1). Bulk SiO_2 content ranges from 48.0–74.9 wt.% and total alkalis (Na_2O + K_2O) range from 3.36–7.92 wt.%. Bulk NBO/T ranges from 0.04–0.79. Glass SiO_2 content ranges from 50.2–73.7 wt.% and total alkalis (Na_2O + K_2O) from 3.08–9.54 wt.%. Glass NBO/T ranges from 0.03–0.76. This range is typical of the spectrum of volcanic ash compositions erupted from subduction-zone volcanoes, which are the dominant sources of volcanic ash globally (Cashman and Rust, 2016). Differences between bulk and glass compositions primarily reflect the mineral (crystal) content of the ash.

Table 3.2: Major Oxide Composition of Bulk Ash in wt.% Determined by XRF

Sample	SiO_2	TiO_2	Al_2O_3	Fe_2O_{3tot}	MnO	MgO	CaO	Na_2O	K_2O	P_2O_5	SO_3	LOI	Total	f	NBO/T
Askja	72.35	0.86	12.58	4.01	0.113	0.86	2.62	4.05	2.373	0.171	<0.003	1.02	99.10	0.50	0.13
Aso	54.96	0.85	18.30	7.95	0.126	3.48	8.55	2.77	1.699	0.239	1.083	2.88	99.34	0.30	0.43
Augustine	62.86	0.62	16.58	5.08	0.111	3.10	6.48	3.92	1.103	0.123	<0.003	0.16	100.44	0.35	0.26
Chaitén	74.90	0.16	14.15	1.47	0.063	0.35	1.54	4.28	3.025	0.063	<0.003	1.33	99.23	0.50	0.04
Etna†	48.04	1.79	17.80	10.43	0.175	5.28	10.08	3.67	2.087	0.585	0.058	-0.09	99.18	0.30	0.63
Eyjafjallajökull (a)	60.00	1.31	14.68	8.22	0.216	2.93	4.47	5.64	2.283	0.240	0.006	-0.08	98.28	0.40	0.38
Eyjafjallajökull (b)	58.85	1.46	14.96	8.51	0.209	3.32	5.01	5.36	2.059	0.260	<0.003	-0.16	99.39	0.40	0.40
Grímsvötn (a)	50.58	2.81	13.59	13.46	0.212	5.57	9.94	2.87	0.488	0.305	0.163	-0.93	98.21	0.20	0.74
Grímsvötn (b)	50.33	2.91	13.58	13.71	0.218	5.32	9.86	2.89	0.479	0.312	0.387	-0.42	98.67	0.20	0.75
Nisyros	74.16	0.33	14.01	2.24	0.096	1.02	1.59	2.65	3.803	0.087	0.016	4.85	99.02	0.40	0.05
Okmok	53.23	1.22	16.75	9.84	0.186	5.15	9.33	3.22	0.880	0.181	0.004	-0.13	100.06	0.30	0.54
Spurr	55.99	0.73	18.96	7.26	0.153	4.45	7.63	3.48	0.962	0.235	0.157	0.51	100.30	0.30	0.36
Tongariro	64.13	0.70	17.72	6.41	0.070	2.14	4.66	2.39	1.359	0.147	0.266	5.96	99.20	0.35	0.17

Note: Components with concentrations below the lower limit of detection reported as < LLD.
Original totals include loss on ignition (LOI).
Specific ferric/ferrous ratios (f) used to calculate NBO/T are reported.
Total iron expressed as Fe_2O_3.
†Sample underwent a two-stage ignition to avoid potential problems caused by the ash composition that may have engendered significant sintering or melting at 950°C. First stage ignition was undertaken at 750°C.

Table 3.3: Major Oxide Composition of Glassy Components in wt.% Determined by EPMA

Sample	SiO_2	TiO_2	Al_2O_3	FeO_{tot}	MnO	MgO	CaO	Na_2O	K_2O	P_2O_5	Total	n	f	NBO/T
Askja	73.69	0.77	12.79	3.24	0.10	0.60	2.46	3.81	2.406	0.136	98.35	24	0.5	0.10
Aso	55.90	0.96	19.23	7.15	0.15	2.22	8.69	3.26	2.182	0.274	98.90	57	0.3	0.32
Augustine	66.20	0.24	19.94	1.29	0.04	0.20	6.49	4.27	1.259	0.072	100.18	30	0.4	0.04
Chaitén	73.70	0.11	15.50	1.09	0.06	0.22	2.31	4.40	2.562	0.043	98.89	30	0.5	0.05
Etna	50.92	2.02	16.64	10.25	0.24	3.30	7.47	4.58	3.817	0.769	97.87	25	0.35	0.55
Eyjafjallajökull (a)	66.43	0.93	14.14	5.93	0.18	0.65	1.98	5.84	3.696	0.234	99.38	15	0.5	0.21
Eyjafjallajökull (b)	64.25	1.18	14.81	6.52	0.18	1.00	3.01	5.54	3.199	0.312	98.89	35	0.5	0.24
Grímsvötn (a)	51.30	2.80	13.37	13.33	0.23	5.56	9.81	2.75	0.483	0.363	98.48	14	0.2	0.76
Nisyros	72.20	0.23	16.34	1.48	0.05	0.15	3.14	3.00	3.390	0.027	96.29	10	0.5	0.10
Okmok	55.19	1.68	14.10	11.82	0.22	4.03	8.05	3.41	1.213	0.283	97.65	27	0.3	0.59
Spurr	50.21	0.10	29.53	1.56	0.04	1.44	13.92	2.97	0.107	0.112	99.28	30	0.2	0.10
Tongariro	58.18	0.16	25.55	1.08	0.03	0.30	9.67	3.80	1.150	0.087	99.34	33	0.35	0.03

Note: Results quoted as mean component oxide weight percent based on n number of analyses, normalised to 100% with original totals reported.
Specific ferric/ferrous ratio (f) used to calculate NBO/T are reported.

Total iron expressed as FeO.

3.3.2 Correlations with complex refractive index

3.3.2.1 Visible wavelengths

The real and imaginary components of the refractive indices of the Ball et al. (2015) dataset show a strong linear relationship with both the bulk and glass compositions (SiO_2 and NBO/T) at 450.0 nm, 546.7 nm and 650 nm. The strength of the correlation, represented by R^2, varies with wavelength, and shows differences between bulk and glass, and between SiO_2 content and NBO/T. The correlation of the real part with bulk composition is shown in Figure 3.2 and with glass is shown in Figure 3.3. The real part appears to be more strongly correlated with bulk compositions than glass, with R^2 values for bulk SiO_2 (0.899–0.916) greater than those for glass SiO_2 (0.756–0.789). This same trend can be seen for NBO/T, with R^2 values for bulk (0.963–0.969) greater than the R^2 values for glass (0.801–0.828). Figure 3.4 shows that the imaginary part has a stronger correlation with bulk SiO_2 (R^2 = 0.802–0.857) than with bulk NBO/T (R^2 = 0.643–0.811). Similarly, the glass SiO_2 (R^2 = 0.786–0.824) is better correlated with the imaginary part than the glass NBO/T (R^2 = 0.456–0.702), shown in Figure 3.5. The correlation for the imaginary part with NBO/T (glass and bulk) gets weaker as wavelength increases, whereas this trend is not observed for SiO_2. Correlation with the imaginary part appears to be weaker in general than with the real part and correlations with bulk compositions appear to be stronger than with glass, with the exception of glass SiO_2 for the imaginary part, which is similar to that of the bulk.

The higher R^2 for bulk composition is likely due to the measurement technique used by Ball et al. (2015). It was undertaken on a grain-by-grain basis with little discrimination between grain types and so it represents an average of the whole sample as opposed to just the glassy component. The key difference between SiO_2 and NBO/T as compositional parameters is that the latter is a measure of the depolymerisation of the tetrahedral structure within the melt, which affects the length of $T—O^-$ bonds. We do not expect to see much difference between SiO_2 and NBO/T correlations in the visible range because variations in bond length are only observable in the infrared region,

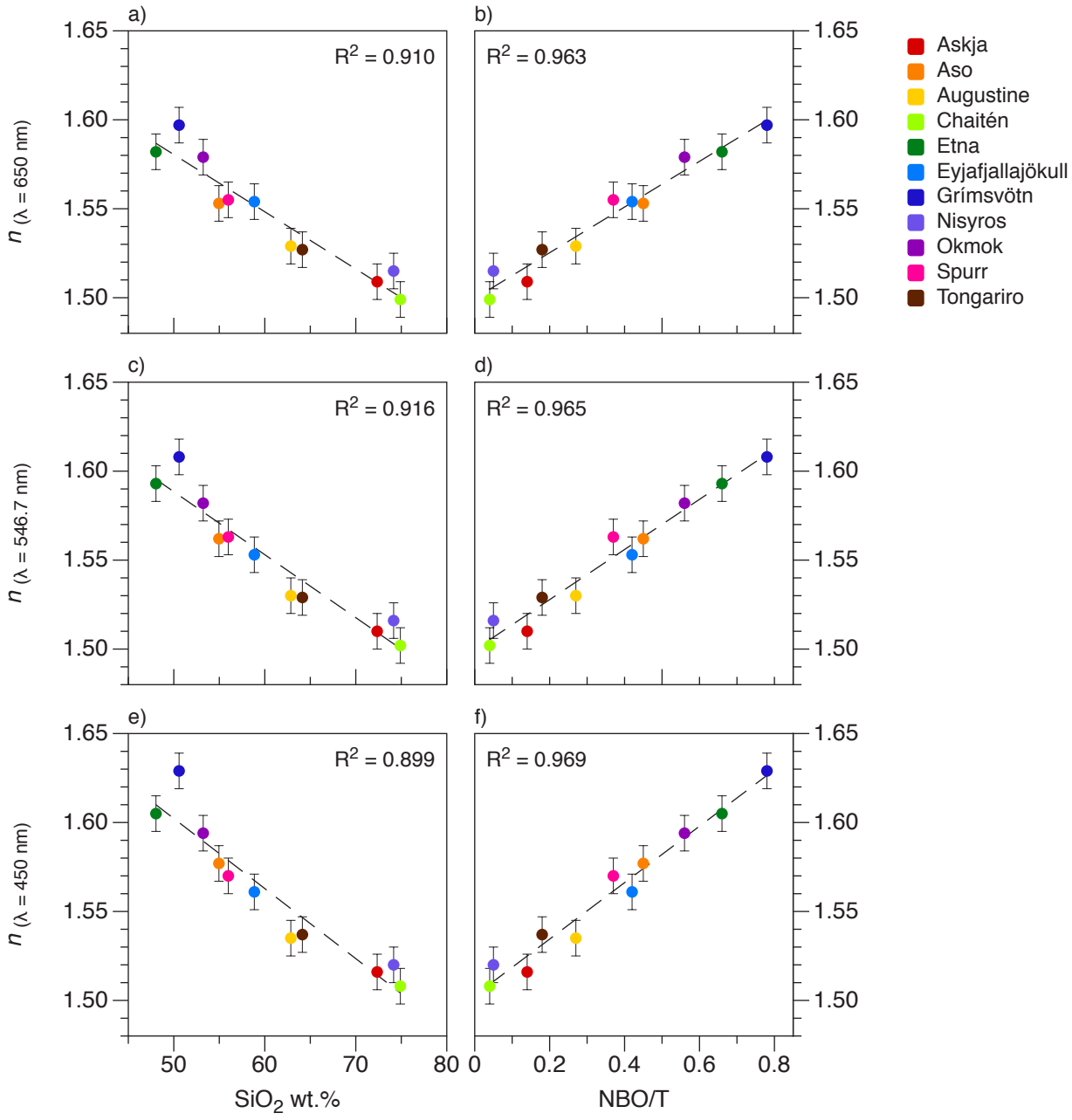

Figure 3.2: Real part of the refractive index (n) vs. ash sample bulk SiO_2 and bulk NBO/T. Plots a) and b) are for n measured at a wavelength of 650 nm, c) and d) are at 546.7 nm and e) and f) are at 450 nm.

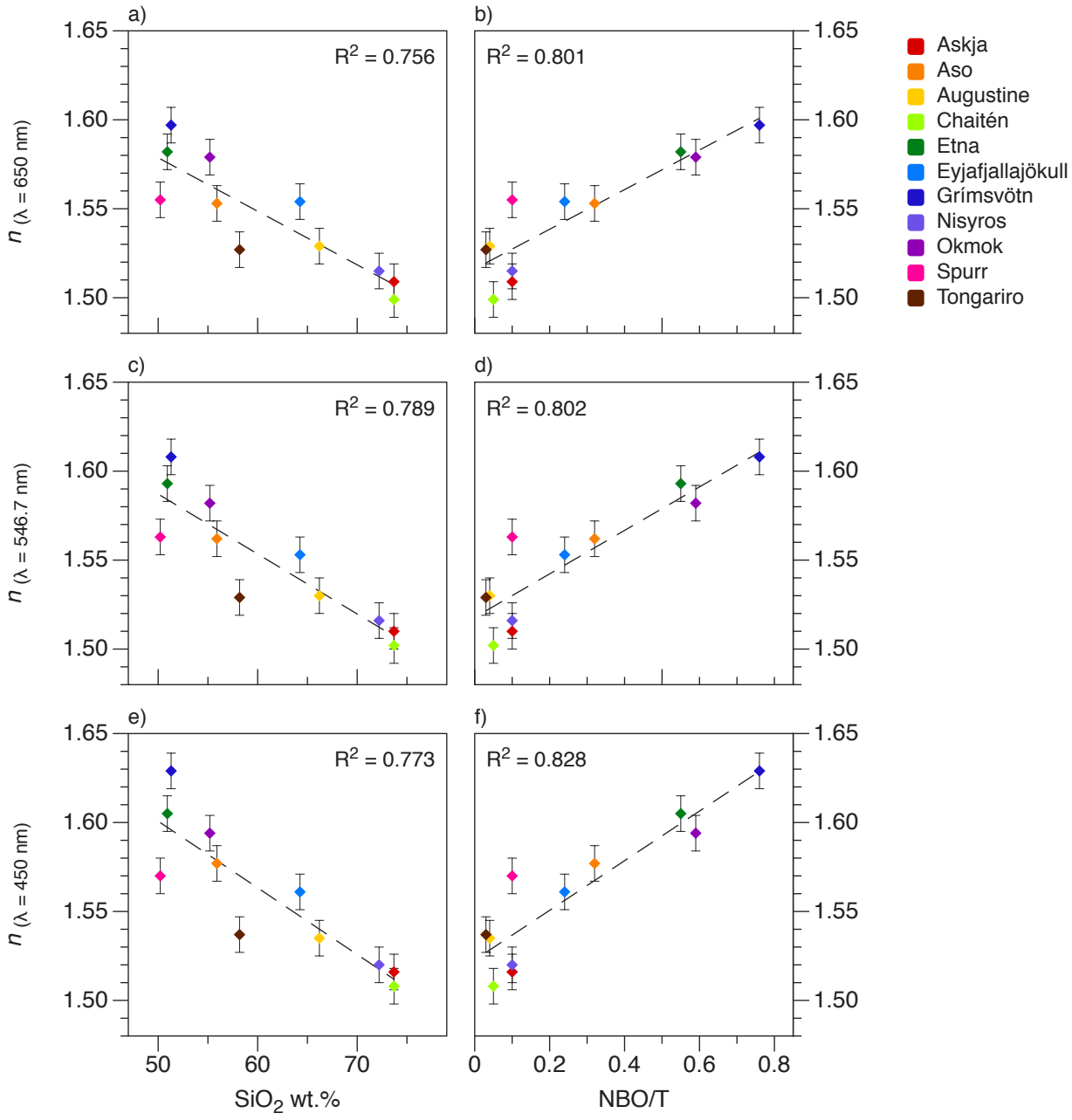

Figure 3.3: Real part of the refractive index (n) vs. ash sample glass SiO_2 and glass NBO/T. Plots a) and b) are for n measured at a wavelength of 650 nm, c) and d) are at 546.7 nm and e) and f) are at 450 nm.

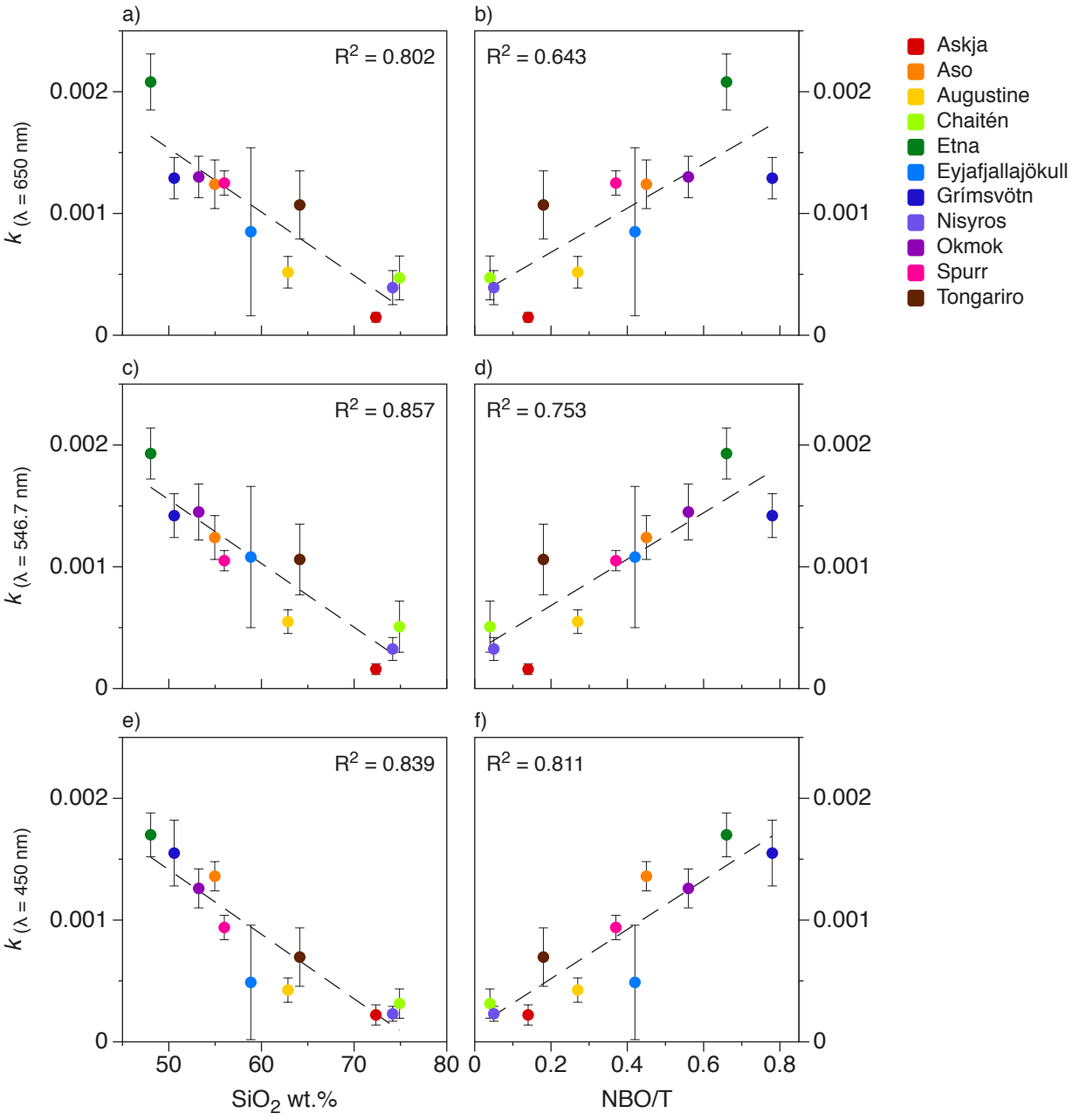

Figure 3.4: Imaginary part of the refractive index (k) vs. ash sample bulk SiO_2 and bulk NBO/T. Plots a) and b) are of k measured at a wavelength of 650 nm, c) and d) are at 546.7 nm and e) and f) are at 450 nm.

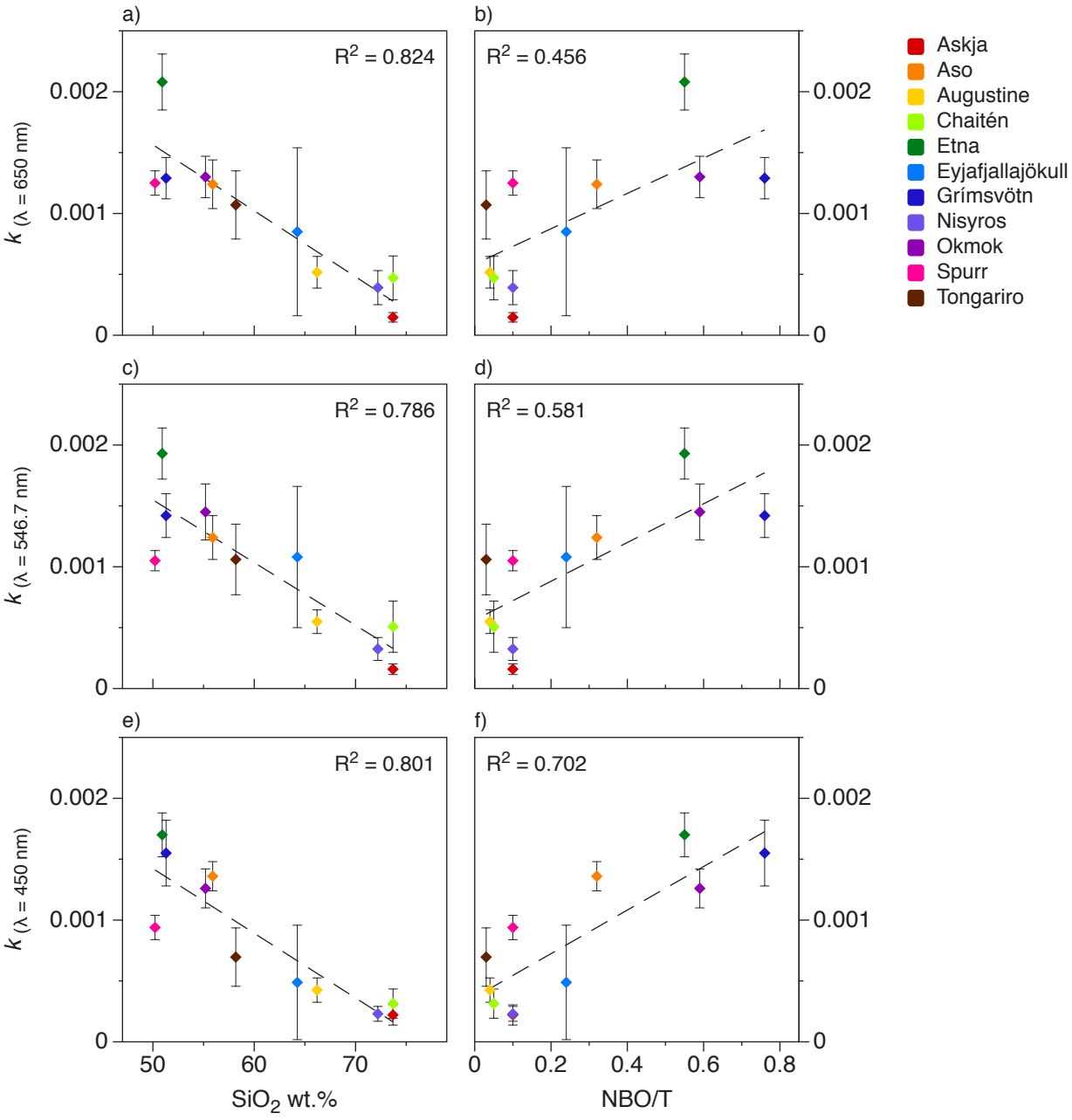

Figure 3.5: Imaginary part of the refractive index (k) vs. ash sample glass SiO_2 and glass NBO/T. Plots a) and b) are of k measured at a wavelength of 650 nm, c) and d) are at 546.7 nm and e) and f) are at 450 nm.

where silicate bond vibrations are detectable. The very high correlations with the real part indicate that SiO_2 content is primarily influencing the scattering. SiO_2 content is the main control on NBO/T because it is the most abundant tetrahedral cation, which explains why NBO/T is also strongly correlated with n. Poorer correlation with the imaginary part may be due to the fact that absorption in the visible region is influenced by electronic processes, such as crystal field effects (Clark, 1999) caused by unfilled electron shells of transition elements (Ni, Cr, Co, Fe etc.). It is not directly affected by the SiO_2 content or tetrahedral network. In addition, silicate glass is transparent in the visible range (Kitamura et al., 2007) meaning any absorption is due to other elements. The correlation is likely due to the indirect effect of SiO_2 content on the proportion of mafic minerals containing these transition metals.

3.3.2.2 Spectral correlations

To explore the relationships between refractive indices and composition at other wavelengths, we compared the complex refractive indices from Reed et al. (2018) with our composition measurements. A linear regression analysis at each measurement wavelength (0.4–19 μm) was used to determine R^2 for the correlation with bulk and glass composition in terms of SiO_2 and NBO/T (Figure 3.6). For the real part, this produces high R^2 values (Figure 3.6) in the visible to near-infrared range (0.4–3.5 μm) for each of the four compositional parameters; bulk SiO_2 ($R^2 > 0.8$), glass SiO_2 ($R^2 > 0.6$), bulk NBO/T ($R^2 > 0.9$) and glass NBO/T ($R^2 > 0.7$). In this region (0.4–3.5 μm), scattering dominates the interaction between light and particles. This is consistent with results from Section 3.3.2.1 and shows that the linear relationship extends to longer wavelengths. R^2 varies greatly in the mid-infrared range (3.5–18 μm) and decreases dramatically around 6 μm, where n begins to show greater structure (lower panel; Figure 3.6). Only glass SiO_2 R^2 remains above 0.5 between 6 and 8 μm. Within the IASI spectral range of 3.62–15.5 μm, local peaks in R^2 for each of the four compositional parameters occur around 8, 10, and 12 μm. Between 8 and 12 μm these precede

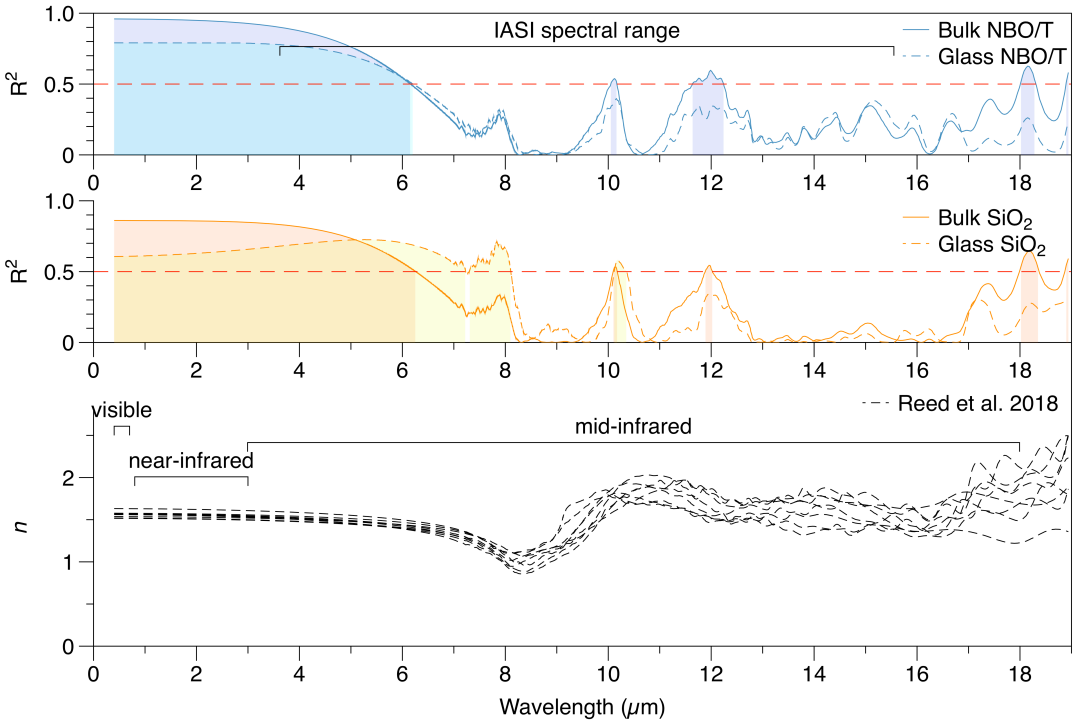

Figure 3.6: R^2 for the linear regressions between the real part of the refractive index (n) and ash sample NBO/T (upper panel) or SiO_2 (middle panel) vs wavelength of measurement. The n measurements are from Reed et al. (2018) and are represented by black dashed lines (lower panel). R^2 values for the correlation between n and bulk ash composition are represented by the solid lines and for the correlation between n and glass composition by the dashed lines. Shading under the curves shows the areas where $R^2 > 0.5$, with the darker shade representing bulk and lighter shade glass. The IASI spectral range is also indicated.

the turning points in n, occurring at slightly shorter wavelengths. The minima in R^2 correspond to the broader trough (8.5–9 μm) and peak (around 11 μm), where the measurements of n intersect one another, indicating that the relationship with composition at these wavelengths is non-linear. Bulk R^2 values (solid line; Figure 3.6) are higher than glass R^2 (dashed line; Figure 3.6) over most of the spectral range for the real part, except between 5–9.5 μm and 10–11 μm for SiO_2, where glass R^2 is higher.

The correlation is very poor (R^2 close to zero) for the imaginary part in the visible to near-infrared region (Figure 3.7), contrary to the findings in Section 3.3.2.1 with the visible measurements. This is likely due to the difference in measurement techniques between Ball et al. (2015) and Reed et al. (2018), who used much finer-grained samples with effective radii ranging from 0.574–1.16 μm. At wavelengths below 7 μm,

Reed et al. (2018) reported greater uncertainties on the measured mass extinction coefficient from which the complex refractive index was retrieved. At shorter wavelengths (0.4–7 μm) scattering dominates the interaction, but as the wavelength of the incident light becomes larger than the particle size (> 7 μm), scattering efficiency is reduced and absorption begins to dominate. This effect can clearly be seen in Figure 3.7 where R^2 begins to increase at wavelengths above 7 μm. The T—O^- bond absorption feature occurs at around 8–12 μm depending on its length (Kieffer, 1979), governed by the nature of cations forming the tetrahedral framework (Mysen and Richet, 2005). In this dataset, k peaks between 9–10 μm, corresponding to the asymmetric stretching resonance of the Si—O—Si bridge in silicates (Kitamura et al., 2007). This feature shifts to longer wavelengths as the bonds become longer so we would expect to see a lower frequency absorption peak in samples with a greater NBO/T. The dip in correlation (R^2) between 3.5–4 μm is in agreement with spectroscopic studies on silica glass which show that it is effectively opaque at this wavelength (Kitamura et al., 2007). R^2 peaks at around 8.3 and 11.5 μm, either side of this absorption peak. The peaks in k vary in width and intensity, and according to wavelength, so the linear relationship breaks down where the spectra intersect, and this detail is not captured in our parameterisation in Section 3.3.3. Bulk composition (solid line; Figure 3.7) produces higher R^2 values than glass (dashed line; Figure 3.7) for NBO/T and over most of the spectrum for SiO_2, except in the range 8–9 μm where glass SiO_2 has a higher R^2.

3.3.3 Parameterisation

The variability in R^2 across the spectrum and the location of the peaks in R^2 around the important spectral shape features (peaks and troughs) in both parts of the complex refractive index mean that there is enough information to allow us to make justifiable estimates of n and k based on composition alone. The broad-spectrum correlations indicate that using bulk ash composition gives overall higher R^2 values than using the glass composition, so we have based our parameterisation on bulk composition. The

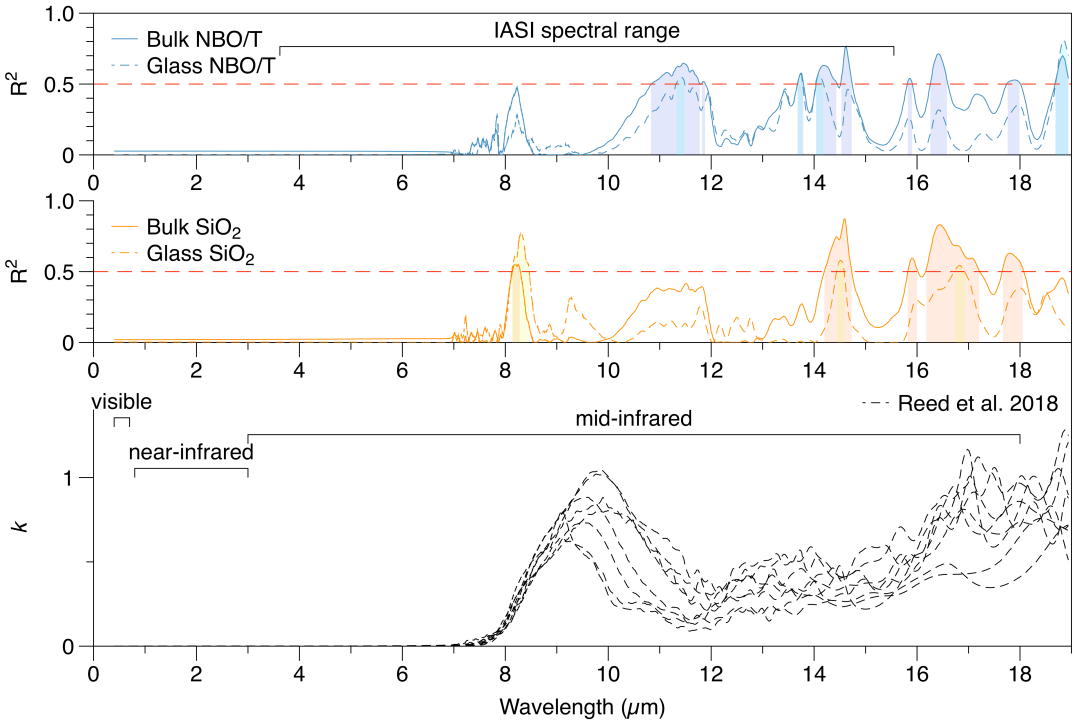

Figure 3.7: R^2 for the linear regressions between the imaginary part (k) and ash sample NBO/T (upper panel) or SiO_2 (middle panel) vs wavelength of measurement. The k measurements are from Reed et al. (2018) and are represented by black dashed lines (lower panel). R^2 values for the correlation between k and bulk ash composition is represented by the solid lines and glass composition is represented by the dashed lines. Shading under the curves shows the areas where $R^2 > 0.5$, with the darker shade representing bulk and lighter shade glass. The IASI spectral range is also indicated.

parameterisation used is a linear regression with bulk NBO/T and SiO_2 as the input variables and the real (n_i) and imaginary parts (k_i) of the complex index of refraction as the outputs. There are M wavelengths, spaced irregularly and the regression equations are:

$$n_{ij} = a_{ij} + b_{ij}X_j \tag{3.2}$$

and

$$k_{ij} = c_{ij} + d_{ij}X_j \tag{3.3}$$

where a_i, b_i, c_i and d_i are regression coefficients provided at discrete wavelengths i, where $i = 1...M$. X_j is the fraction NBO/T when $j = 1$ and the $\%SiO_2$ when $j = 2$. The coefficients are tabulated at each wavelength and provided as a spreadsheet in Appendix C.

Figure 3.8 shows the effect of varying the NBO/T and SiO_2 input parameters on the calculated complex refractive index. Using NBO/T (Figure 3.8a) in the parameterisation results in a slight dampening of the amplitude of the curve generated for n when compared with using SiO_2 (Figure 3.8b). Between 9.2–10.4 μm and 11.2–12.8 μm the variation of n with increasing SiO_2 content is greater than the variation in NBO/T, so the parameterisation is more sensitive to differences in SiO_2 than NBO/T in these regions. Similar effects are noted in the imaginary part, with a smaller variation in k between 10–11.8 μm for NBO/T (Figure 3.8c) than for SiO_2 (Figure 3.8d). Increasing the NBO/T results in a higher peak in k when compared with the variation in peak height for changing SiO_2 content. In the measurement dataset the height of the peak in k does not appear to vary according to SiO_2 or NBO/T, so there may be other factors, such as variations in particle shape between samples, which have affected the measurements (Reed et al., 2018). The peak in k in the parameterisation also shifts to longer wavelengths and broadens as SiO_2 content decreases and as NBO/T increases, which is consistent with what would be expected due to lengthening of $T—O^-$ bonds. The bulk NBO/T appears, on balance, to be the best parameter to represent composition,

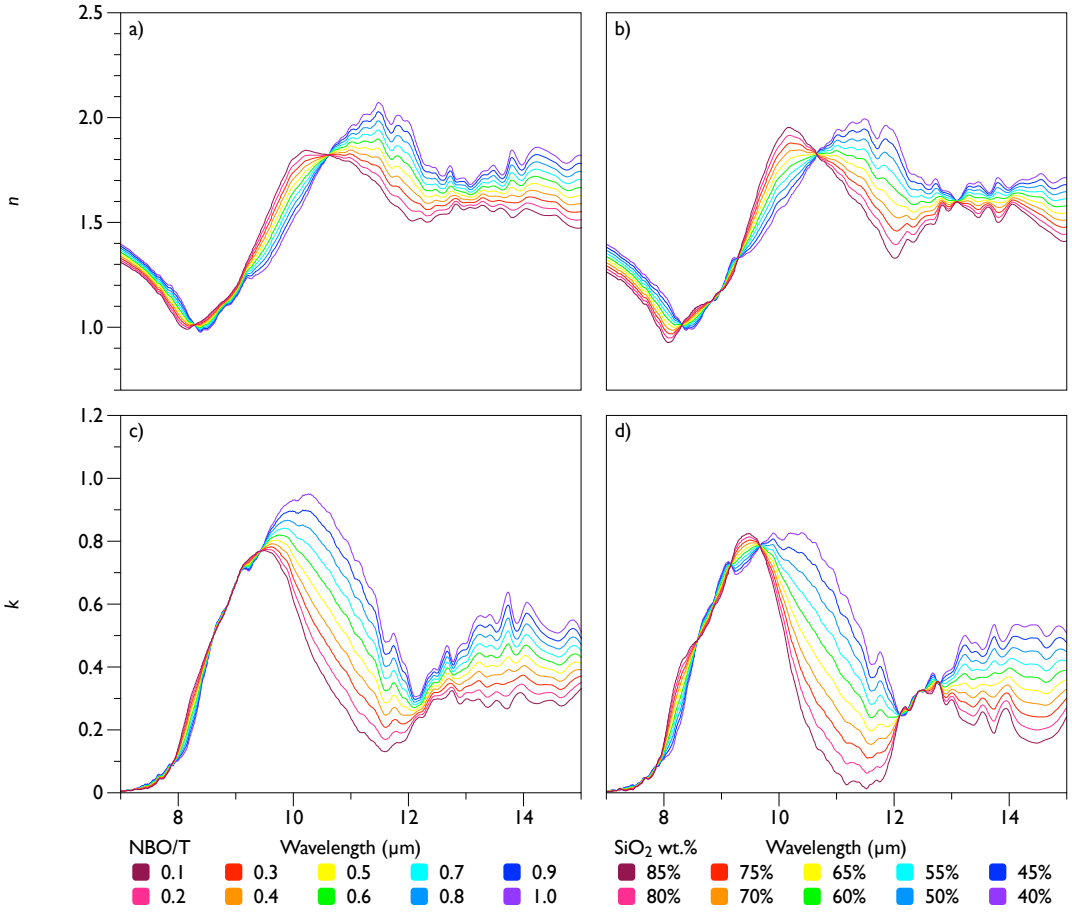

Figure 3.8: Modelled complex refractive indices showing the effect of varying parameters NBO/T and SiO_2. a) Modelled real part of the refractive index (n) based on NBO/T, and b) based on SiO_2 content. c) Modelled imaginary part of the refractive index (k) based on NBO/T, and d) based on SiO_2 content. Typical bulk volcanic ash samples are most likely to have SiO_2 contents from 48 - 77 wt%; higher SiO_2 contents would only be expected in samples that have been enriched in quartz grains.

as shown in Figure 3.6 and Figure 3.7. For this reason, and for ease of modelling, the subsequent analyses have been undertaken using the bulk NBO/T parameter.

In order to assess how well the parameterisation performs at reproducing an independent dataset, we compared it to the real and imaginary parts of the Pollack dataset. Compositional data from Pollack et al. (1973) was used to calculate the NBO/T for the five samples reported: "Obsidian Little Glass Mt." (Obsidian 1), "Obsidian Lake County" (Obsidian 2), "Basaltic glass" (Basalt 1), "Basalt" (Basalt 2), and "Andesite". The calculated indices generally show good agreement with the measurements for both parts of the refractive index, broadly capturing the shape and alignment of the curves

(Figure 3.9). The parameterisation underestimates the peaks and overestimates the troughs of n to varying degrees. This is more evident for the two obsidian samples, and agreement is better for the two basalt samples and the andesite sample. For the imaginary part the parameterisation underestimates the main peak between 8–12 μm. Again, this is more pronounced for the two obsidian samples than the basalt and andesite samples. At wavelengths greater than 12 μm, the calculated k fits the measurements better for the two obsidian samples than the other three samples.

The difference in peak-height in k may be due to differences in the nature of our samples compared with those of Pollack et al. (1973), with compositional heterogeneity between grains potentially affecting the measurements on which the parameterisation was based. Measurements made on slabs rather than particulates are not subject to the same grain-size and shape effects as in our dataset, and Reed et al. (2018) noted that variation particle shape between samples was not taken into account. As more ash refractive indices become available, their fit to the parameterisation should be assessed and if necessary, this new data should be added to the parameterisation spreadsheet to update the model (Appendix C). Linearly fitting the real and imaginary parts of the refractive index independently of one another may mean that the parameterisation does not obey the Kramers-Kronig relation (Bohren and Huffman, 1983). The Kramers-Kronig relation shows that the real part of the refractive index can be derived if the imaginary part is known or vice-versa. Our parameterisation is intended as a first approach to see if the method works and further development will include this constraint.

3.3.3.1 Impact on brightness temperatures

Passive remote sensing instruments measure radiances, which are a function of wavelength, from the atmosphere and surface. Radiative transfer through a substance in the atmosphere (e.g. volcanic ash cloud) is governed by the complex refractive index of that substance and this can be utilised to calculate its physical properties, such as mass loading. In order to compare measurements at different wavelengths, the radi-

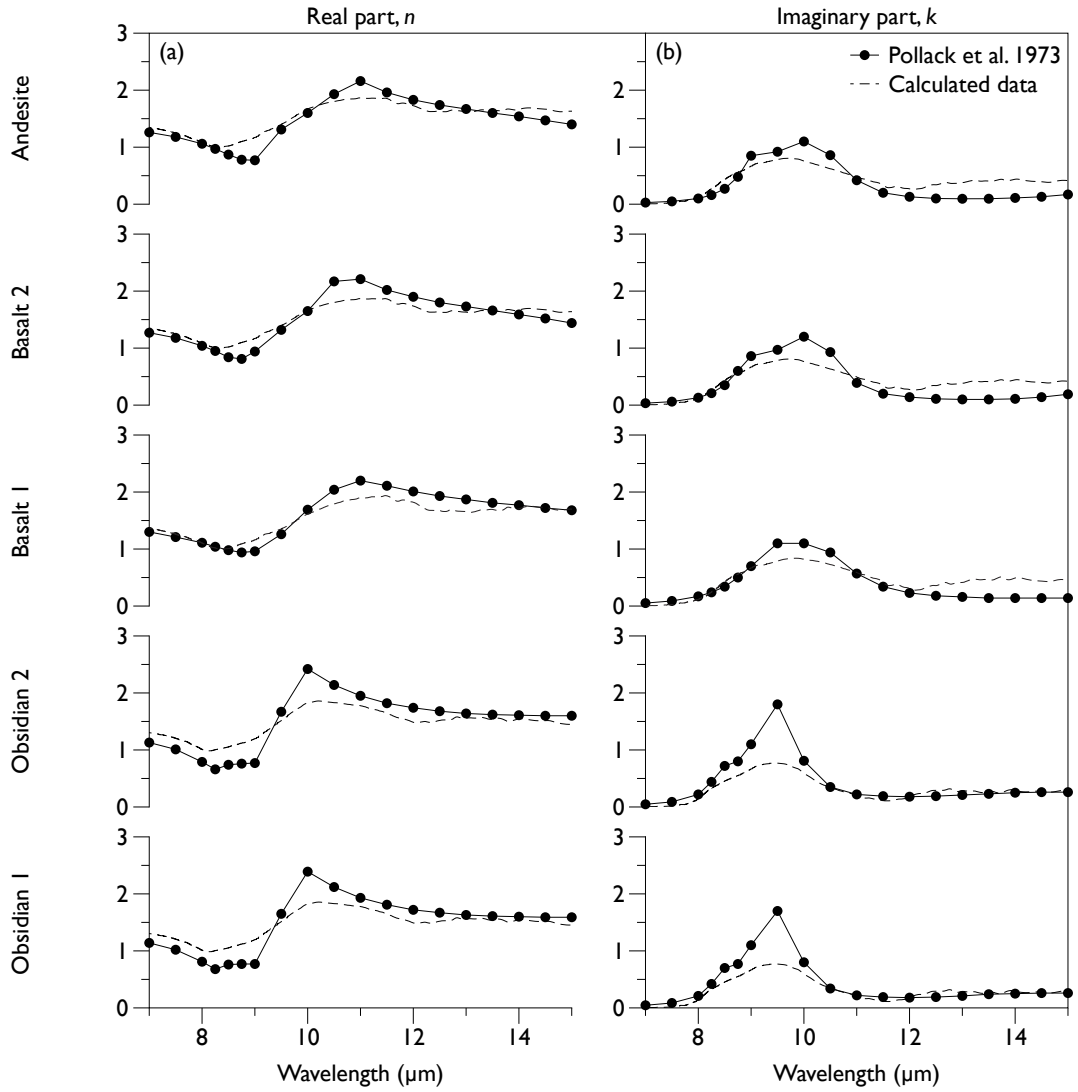

Figure 3.9: Complex refractive indices calculated from the parameterisation compared with the measured indices from Pollack et al. (1973) for five different rock types "Obsidian Little Glass Mt." (Obsidian 1), "Obsidian Lake County" (Obsidian 2), "Basaltic glass" (Basalt 1), "Basalt" (Basalt 2) and "Andesite". a) Real part (n) b) imaginary part (k).

ances must be converted to brightness temperatures, which are calculated by inverting the Planck function. Francis et al. (2012) showed that the choice of refractive index can have a significant effect on calculations of mass loading, derived from brightness temperature differences (Prata, 1989), so we have used our parameterisation to investigate this potential impact. Differences between the parameterisation and measured complex refractive indices at 10.5 and 11.5 μm of Pollack et al. (1973) are up to ±20%, as illustrated in Figure 3.9.

The impact on brightness temperature from errors in the estimation of k can be assessed using the expression for the brightness temperature difference provided by Equation 5 of Prata and Grant (2001):

$$\Delta T = \Delta T_c (X - X^{\beta}) \tag{3.4}$$

$$X = 1 - \frac{\Delta T_{11}}{\Delta T_c} \tag{3.5}$$

where ΔT is the brightness temperature difference, ΔT_c is the temperature difference between the cloud top and the surface (sometimes referred to as the thermal contrast), ΔT_{11} is the difference between the surface temperature and the brightness temperature measured at 11 μm, and β is the ratio of absorption coefficients (α) at two different wavelengths (λ), typically 12 and 11 μm. This expression relates the brightness temperature difference as a function of the ratio of absorption coefficients (α_{12}/α_{11}). Noting that k can be expressed in terms of α (Prata and Prata, 2012) and after a little manipulation,

$$\alpha = \frac{4\pi}{\lambda} k_i(\lambda) \tag{3.6}$$

$$\beta = \frac{11}{12} \frac{k_{12}}{k_{11}} \tag{3.7}$$

$$\delta(\Delta T) = \psi\delta\beta \tag{3.8}$$

where ψ is a scaling factor that includes the thermal contrast between the cloud top temperature and the brightness temperature at 12 μm, and $\delta\beta$ is proportional to the change in the ratio of the imaginary parts of the refractive index at 12 and 11 μm. The mean difference between the parameterisation and measured Pollack et al. (1973) ratios (k_{12}/k_{11}) is ±22%. An error analysis was performed using this model (Equation 3.8) by generating random samples (30,000 trials) of the ratios with perturbations in each k of ±20%. To account for measurement errors, an additional perturbation of ±3% was included. The standard deviation of the distribution of $\delta(\Delta T)$ due to measurement errors was found to be ∼0.2 K, which is close to the measurement noise of current infrared satellite-based sensors. The standard deviation of the distribution due to perturbations of ±20% in each k value was between 1.5–3 K, demonstrating that errors in the refractive indices significantly impact brightness temperature differences, and therefore also mass loading. The impact on the retrieval of mass loading is more complicated, but see Figure 10 of Clarisse and Prata (2016), which shows mass loading as a function of brightness temperature difference. This shows that precision errors in the parameterisation are within measurement noise, but accuracy, i.e. incorrect choice of refractive index, can have a significant impact on brightness temperature differences. This is in agreement with Mackie et al. (2014).

3.3.4 Satellite retrievals

Using the NBO/T parameterisation reported in Section 3.3.3, we calculated refractive indices for Grímsvötn (labelled A93 in Figure 3.10), Chaitén (A94) and Okmok (A95) ash. We selected these eruptions from our suite of samples to span a range of compositions (see Section 3.3.1) and because IASI data were available. In order to assess the potential effects of our new parameterisation on retrieval performance and outputs, we compared retrievals using our new refractive indices with those using the measured

Eyjafjallajökull refractive index (labelled A83 in Figure 3.10) as described in Ventress et al. (2016) using cost function as a minimisation parameter. When using the outputs of our new parameterisation, we observed good agreement with the measurement retrieval (A83) in terms of the shape and extent of the plumes in all three eruptions. Overall slightly higher mass loadings were observed with the calculated indices, and the change in cost function, the minimisation parameter used by Ventress et al. (2016), varied over different parts of the plume in each eruption (Figure 3.10a–f).

Retrievals for the May 2011 Grímsvötn eruption (Figure 3.10a and b) showed good agreement in the overall shape of the plume and similar range in mass loadings. The area of mass loadings greater than 5 g/m^2 expanded further west for A93 than the A83 retrieval. Positive changes in mass loading were observed over the southern part of the plume (Figure 3.10a), with little change to the north. The cost function mostly decreased in the middle part of the plume, where A93 showed increases in mass loading, and increased in the southernmost part (Figure 3.10b).

The shape of the eruption plume for Chaitén in May 2008 from A94 showed good agreement with the A83 retrieval. The mass loading increased in the south and decreased in the north (Figure 3.10c). Most significantly, mass loadings of greater than 2 g/m^2 were detected along the southern limb of the plume using the new parameterised refractive index A94, which were not detected using the A83 dataset. This is consistent with other observations of the Chaitén eruption plume indicating that most of the ash dispersed to the southeast over Argentina, with little or none to the north (Gangale et al., 2010). This change in distribution resulted in a decrease in cost function over the southernmost elongated part of the plume, and an increase in cost to the north (Figure 3.10d).

For the eruption of Okmok in July 2008, the plume was detected fanning out east-southeast away from the volcano. The parameterised retrieval A95 picked up a slight shift in the distribution of mass loading. Greater mass was observed towards the outer parts of the plume and less towards the middle when compared with the A83 retrieval

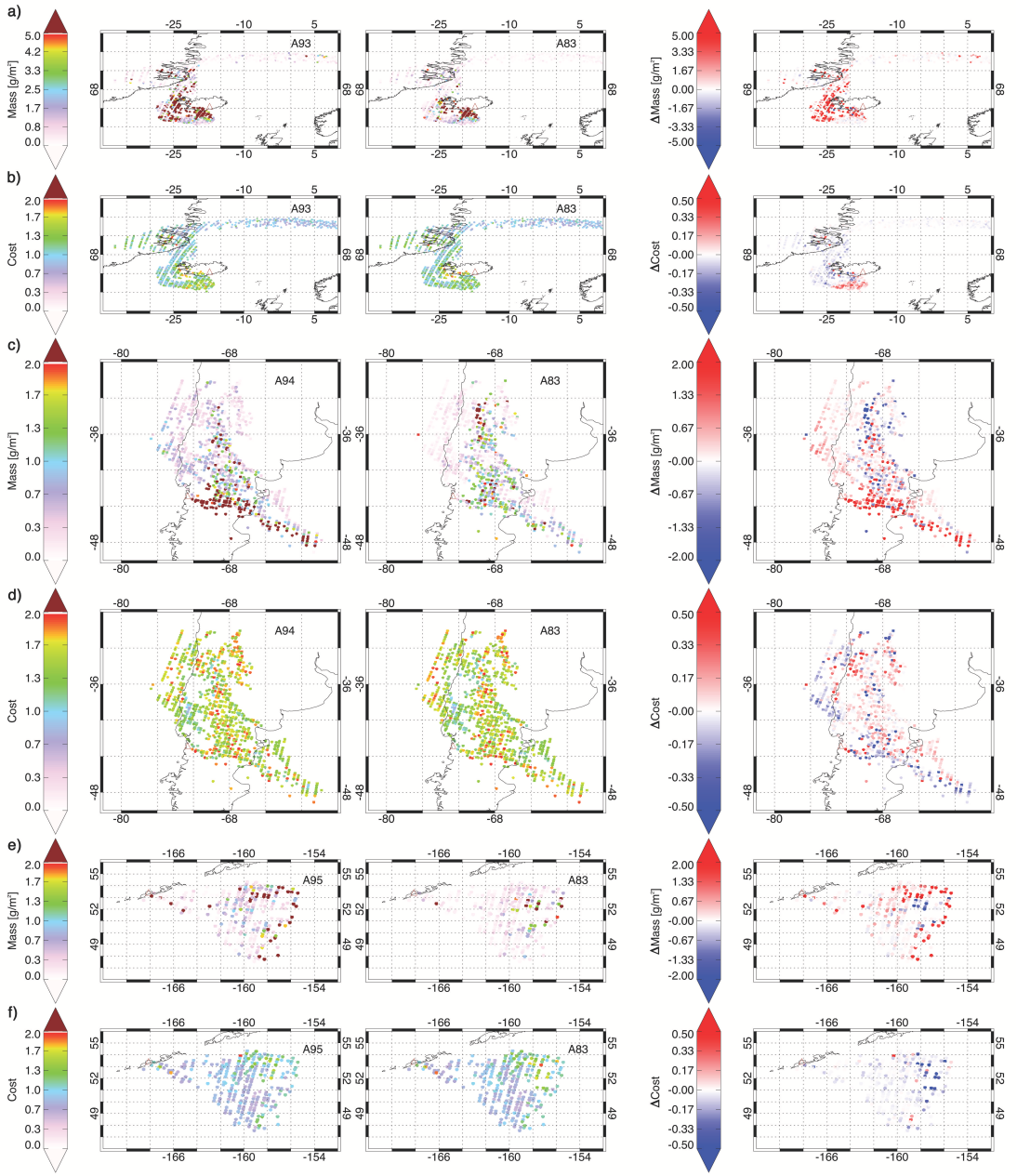

Figure 3.10: Satellite retrievals of mass loading from IASI data for the eruptions of Grímsvötn, Chaitén, and Okmok. The left-hand column is the retrieval using refractive indices calculated from our new parameterisation (Grímsvötn—A93, Chaitén—A94, Okmok—A95), the middle column uses a measured Eyjafjallajökull refractive index (A83) and the right-hand column is the difference between the two, i.e. first minus the second. a) Mass loading and b) cost function for Grímsvötn on 22nd May 2011 in the afternoon, c) mass loading and d) cost function for Chaitén on 3rd May 2008 in the morning, e) mass loading and f) cost function for Okmok on 13th July 2008 in the morning.

(Figure 3.10e). More pixels with mass loading greater than 2 g/m^2 were detected using the parameterised refractive index (A95) than with the Eyjafjallajökull measured refractive index (A83), and mass loadings were higher overall. The cost function decreased over the majority of the plume (Figure 3.10f), with the greatest reductions around the outer northeastern edge corresponding to the areas of increased mass.

One caveat with the retrieval algorithm is that it flags pixels containing either volcanic ash or SO_2 (previous works have used the presence of volcanic SO_2 as a proxy for the location of volcanic ash, e.g. Thomas and Prata, 2011) so the algorithm may be attempting to fit the radiative transfer model to a scene that does not actually contain ash (Ventress et al., 2016). This can lead to large cost function values. We know, for example, that the SO_2 plume from the Grímsvötn eruption separated and dispersed northwards while the majority of ash went southwards (Prata et al., 2017). Nevertheless, the parameterised refractive indices make a significant difference compared with the Eyjafjallajökull ash measurements, and in the case of the Okmok eruption, clearly reduce the cost function.

3.4 Conclusions and further work

We have developed a method to estimate the complex refractive index of a volcanic ash sample based on its composition, in terms of silica content and/or NBO/T. A spreadsheet to calculate the complex refractive index using this new parameterisation is provided in Appendix C. We find that it is sufficient to use wt. % SiO_2 to estimate refractive index, but recommend that it is better to use NBO/T if the data are available. This simple linear model is an improvement on the current procedure of using a single standard reference refractive index dataset, such as the Pollack 'andesite', for all types of volcanic ash. By using an analytical expression, we have shown that errors of ±20% in the calculated imaginary part can have a significant effect on brightness temperature difference. Using this approach, we are able to produce retrievals of mass loadings that can replicate the broad features observed from IASI data using actual measured

refractive indices of Eyjafjallajökull ash. We have also demonstrated that using a refractive index dataset based on the eruption-specific composition does have an impact on the mass loading retrievals. In all three test cases we analysed, the retrievals using our method were in good agreement, in terms of plume size and shape, with retrievals using the measured Eyjafjallajökull refractive index. However, slightly greater mass loadings were observed overall using our new ash refractive index parameterisations in the retrievals compared to using the Eyjafjallajökull refractive index, and the distribution of mass loadings and cost function varied significantly across the plumes. Mass loading is an important parameter used in volcanic ash dispersion modelling for estimating and forecasting ash concentrations downwind, which is a vital tool in assessing hazards for aviation (see Mackie et al., 2016, and references therein). The implication of our findings is that incorrect assumptions could lead to inaccurate mass loadings from satellite data, which is consistent with the findings of Francis et al. (2012) and Mackie et al. (2014). Our initial linear parameterisation is a first approach to see if the method works and future work would include further constraints, such as the Kramers-Krönig relation, which provides an analytic connection between the real and imaginary parts of the refractive index. Further testing of the parameterisation with new refractive index measurements as they become available in the mid-infrared range (7–15 μm) will greatly improve its utility. Further ground-truthing of quantitative satellite ash retrievals is also to be encouraged.

Chapter 4

Trace metal composition of distal ash

This chapter presents the compositions of leached aerosol samples collected in Oxford during the explosive summit eruption of Eyjafjallajökull in April and May 2010. The work presented here contributes to a large and multifaceted dataset on this eruption, which combines remote sensing with direct measurements of the atmospherically transported ash.

4.1 Introduction

Airborne aerosol trace metals in the environment can originate from both anthropogenic and natural sources. Characterising the levels of trace metals in the atmosphere is important for understanding their impact on air quality and health, their impact on the environment and for understanding global biogeochemical cycles (Chester, 2000). The size of aerosols is also important because it influences their atmospheric residence time, the extent to which they are transported, their environmental bioavailability and how deeply they can penetrate the respiratory system if inhaled (Horwell and Baxter, 2006; Kelly and Fussell, 2012). Volcanic emissions represent an important natural source of atmospheric trace metals (Browning et al., 2015). They contribute to the stratospheric aerosol load through large-scale explosive eruptions, and to the troposphere through smaller eruptions and sustained, magmatic and hydrothermal degassing (Mather et al., 2003). While the impact of stratospheric volcanic aerosol has been extensively investigated (Robock, 2015), the impacts of tropospheric volcanic aerosol are less well

understood (Mather et al., 2003).

In this study we present concentrations of a suite of selected trace metals (Mg, Al, Ca, Ti, V, Cr, Mn, Fe, Co, Ni, Cu, Zn Sr, Mo, Cd and Pb) in urban air in Oxford, UK during the period in which the Eyjafjallajökull ash cloud was thought to be overhead. We have compared the concentrations of Mg, Al, Ca and Ti to regional measurements of these elements across the UK, and made a direct comparison of V, Cr, Mn, Fe, Co, Ni, Cu, Zn, Sr, Mo, Cd and Pb to the size-segregated urban background in Oxford characterised by Witt et al. (2010). This comparison allows us to evaluate the extent to which a volcanic signal might be identifiable in different size fractions or for different metals. Any increases in these concentrations can be attributed to a contribution from the ash, which has implications for the environmental detection and impact of distal ash from this eruption.

4.1.1 The Eyjafjallajökull eruption

The eruption of Eyjafjallajökull, Iceland (63°37'12" N, 19°36'48" W, 1660 m above sea level) in the spring of 2010 was characterised by widespread ash dispersal and air traffic disruption across Europe. The initial magmatic eruption began on 20 March as effusive activity of alkali olivine basalt from two main fissures on the flank of the volcano at Fimmvörðuháls and lasted until 12 April (Karlsdóttir et al., 2012). On 14 April, activity shifted to the summit and a larger, more explosive eruption began, lasting 39 days. The switch to phreatomagmatic activity due to the interaction of magma with glacial melt-water produced vast quantities of fine ash. There were two particularly intense periods (14 – 18 April and 5 – 18 May) during which airborne ash was detected by satellite remote sensing over a wide region (Gudmundsson et al., 2012). Analysis of the composition of tephra from the summit eruption revealed a rapid mingling of two end-member compositions (Sigmarsson et al., 2011). The fallout during the first intense phase (Phase I; Gudmundsson et al., 2012) contained three different glass types: rhyolite, trachyte and benmoreite (SiO_2 60–70 wt%), indicating rapid mingling

of an evolved Fe-Ti-basalt with a silicic melt (Sigmarsson et al., 2011). Then, at the beginning of May, a fresh injection of Mg-rich basalt into the pre-existing silicic melt resulted in decreasing proportions of the mafic end-member (Sigmarsson et al., 2011) observed in the tephra erupted during the second intense phase (Phase III; Gudmundsson et al., 2012). The change in composition of the tephra was important in identifying and understanding the complexities of the magma mixing and mingling processes fuelling the eruption. During these explosive phases, at least 20% of the mass erupted contained ash with less than 10 μm diameter (Gíslason et al., 2011; Stevenson et al., 2012; Dacre et al., 2013), meaning that it could stay airborne for prolonged periods of time and be transported long distances. Satellite and ground-based remote sensing techniques were used to track the movement of the ash cloud generated by the eruption as it spread southwards over Europe and then elongated westwards over the UK (Campanelli et al., 2012; O'Dowd et al., 2012; Prata and Prata, 2012; Toledano et al., 2012; Pappalardo et al., 2013).

This eruption provided a unique opportunity to study the trace metal contribution of volcanic aerosols thousands of kilometres from the source and to assess whether any compositional changes could be detected. Airborne observations of the plume were made during a series of research flights which sampled the plume over parts of Europe (Schumann et al., 2011; Rauthe-Schöch et al., 2012; Weber et al., 2012) and by hot-air balloon (Petäjä et al., 2012). The chemical composition of the aerosol has been characterised at numerous sites across Europe: in Germany, France, Switzerland, Italy, Slovenia and the Iberian Peninsula (Bukowiecki et al., 2011; Colette et al., 2011; Schäfer et al., 2011; Beeston et al., 2012; Langmann et al., 2012; Lettino et al., 2012; Revuelta et al., 2012; Rossini et al., 2012; Schleicher et al., 2012; Sandrini et al., 2014). In addition, increased phytoplankton abundance was observed in the Iceland Basin following the eruption, resulting in enhanced major nutrient draw-down (Achterberg et al., 2013). Fortunately, trace metal levels in the urban background in Oxford, UK (located 1700 km from the volcano) had been characterised shortly before the eruption (Witt

et al., 2010). Thanks to some opportunistic aerosol sampling, we were able to generate a dataset that allowed the direct comparison of volcanic-contaminated air with the non-contaminated urban background. The key aspect that differentiates this study from others sampling the volcanic aerosol from the eruption, is that this study documents the impact in an urban setting near anthropogenic sources of atmospheric trace metals.

4.2 Methods

4.2.1 Sampling

Aerosol samples were collected in Oxford over a six-week period during the Eyjafjallajökull eruption (Eyja ash event). Collection started on 16 April 2010, two days after the initial explosive phase began, and continued through the rest of April and into the beginning of June 2010. Samples were collected on the roof of the former Department of Earth Sciences building (now at a different location), University of Oxford, located at 51°45'33.11" N, 1°15'20.26" W, 70 m above sea level. This location was the same as in Witt et al. (2010), who had characterised the aerosol trace metal concentrations in the urban background air in 2007 and 2008. A high-flow cascade impactor with five stages (MSP Corporation, Minneapolis, MN, USA) was used to collect total of 21 size-segregated samples (Table 4.1). During the initial period of collection in April, the air was typically sampled over a duration of around 24 hours, and for longer durations in May.

The cascade impactor is divided into five plates each with a single 76 mm polycarbonate filter. A pump driven by two continuously charged 12V batteries draws the surrounding air through the impactor. At each stage the velocity of the airflow increases, making it increasingly difficult for particles to stay in the airflow. Particles too large to stay in the airflow drop out and are deposited on the filter. The size of particles dropping out depends on the Stokes number, which is a ratio of the stopping distance of the particle to a characteristic dimension of the obstacle (impactor plate), and this can be controlled by varying the airflow rate. It is important that this airflow rate is known

Table 4.1: Oxford Aerosol Sample Collection Details

Sample #	Sample start (UTC)	Flow rate (L/min)	Sample stop (UTC)	Flow rate (L/min)	Sample duration (h)
OxAsh 1	**16/04/2010 15:00**	**107**	**17/04/2010 11:35**	**109**	**20.6**
OxAsh 2	17/04/2010 12:45	48	18/04/2010 16:09	32	27.4
OxAsh 3	18/04/2010 17:00	96	19/04/2010 13:20	0	20.3
OxAsh 4	**19/04/2010 15:25**	**100**	**20/04/2010 16:10**	**90**	**24.8**
OxAsh 5	**20/04/2010 16:40**	**101**	**21/04/2010 16:25**	**102**	**23.8**
OxAsh 6	**21/04/2010 17:00**	**100**	**22/04/2010 16:30**	**101**	**23.5**
OxAsh 7	**22/04/2010 17:00**	**105**	**23/04/2010 16:50**	**86**	**23.8**
OxAsh 8	**23/04/2010 17:23**	**100**	**26/04/2010 15:34**	**86**	**70.2**
OxAsh 9	**26/04/2010 16:05**	**101**	**27/04/2010 16:55**	**87**	**24.8**
OxAsh 10	**27/04/2010 17:20**	**100**	**28/04/2010 16:00**	**93**	**22.7**
OxAsh 11	28/04/2010 16:30	104	29/04/2010 14:40	94	22.2
OxAsh 12	29/04/2010 15:10	102	30/04/2010 16:15	94	25.1
OxAsh 13	30/04/2010 16:50	103	04/05/2010 15:50	108	95.0
OxAsh 14	04/05/2010 16:45	103	05/05/2010 16:35	107	23.8
OxAsh 15	05/05/2010 17:00	99	14/05/2010 16:30	70	215.5
OxAsh 16	16/05/2010 13:20	94	17/05/2010 16:30	93	27.2
OxAsh 17	17/05/2010 17:00	99	19/05/2010 16:10	85	47.2
OxAsh 18	19/05/2010 16:35	97	21/05/2010 16:30	84	47.9
OxAsh 19	21/05/2010 17:10	100	28/05/2010 16:45	91	167.6
OxAsh 20	**28/05/2010 17:48**	**99**	**03/06/2010 15:45**	**87**	**141.9**
OxAsh 21	03/06/2010 17:00	101	23/06/2010 12:00	0	475.0

Note: All times in UTC. Samples used for further analysis are in bold.

accurately for correct designation of size fractions. In addition, the flow rate must be known to calculate the amount of material that passes through the instrument in order to calculate the concentrations of various particles in the air mass. To produce the observed cut off diameters of 2.5 μm, 1.4 μm, 0.77 μm, 0.44 μm and 0.26 μm, a flow rate of 100 L/min is required. A magnehelic pressure gauge was used to monitor the inlet flow rate through the impactor and a control valve was fitted to adjust the speed of the vacuum pump, and thus control the flow rate. Whatman 76 mm, 0.2 μm polycarbonate filters were used on each stage to collect the deposited particles. A plastic hood was also used to provide protection from the weather and to fix the impactor to its sampling spot. Of the 21 samples collected, only nine of them were suitable for analysis (bold font; Table 4.1) as the remaining samples either did not achieve the desired flow rate or there were other issues with collection and storage.

4.2.2 Filter handling and preparation

The filters were used straight from the packaging without any pre-treatment due to the urgency of sample collection. All manipulation and handling of filters was carried out in a metal-free lab, and once exposed, the filters were carefully removed from the cascade impactor and left to dry out in a laminar flow clean hood for 24 hours at room temperature (20–25°C and 25% humidity). Once removed from the aerosol collector, each filter was placed into a petri dish and then placed in a sealed zip-lock bag to prevent any contamination. Clean powder-less vinyl gloves were worn at all times during the handling procedure. Prior to extraction, filters were quartered and weighed in order to determined the mass deposited.

4.2.3 Analysis

The extraction procedure was replicated from Witt et al. (2010), which was modified from Spokes et al. (2001). This was to ensure accurate comparison with background measurements of Oxford aerosol from Witt et al. (2010). The 0.1 M extract solution was made with trace metal grade HNO_3 and > 18 MΩ ultra-pure water. This allows the extraction of the readily soluble fraction and not aluminosilicates. Ceramic scissors and all glass and plastic-wear were cleaned and acid washed before use. The concentrations of Mg, Al, Ca, Ti, V, Cr, Mn, Fe, Co, Ni, Cu, Zn, Sr, Mo, Cd and Pb were measured in extract solutions using a Thermo Finnigan Element 2 Inductively Coupled Plasma Mass Spectrometer (ICP-MS). Samples were analysed by standard addition and diluted using a 2% HNO_3 solution with a 5x dilution. An internal standard of 1 ppb Rh & Re was used to normalise instrument drift and a multi-element calibration spike onto five replicate samples at increasing aliquot volumes was used in order to generate a calibration curve. Pulse-analog (PA) detector calibration was undertaken to ensure validity of linear calibration between two detectors in order to increase the linear working range of the instrument. This was because of the large variation in concentrations across the suite of elements under investigation. A second run using a 50x dilution was performed

on Mg, Al, Fe and Ni because the concentrations of these elements were above the linear calibration range during the first run (5x dilution). Elements were analysed at three different resolutions (low, medium and high) in order to resolve away any molecular or polymetallic (metals with oxides and/or hydrides) interferences.

4.2.4 Blank corrections and detection limits

As the concentrations of metals in the atmosphere are at trace levels, the procedure requires low and stable blanks for analysis. Uncertainties can arise from the type of filter used, formation of artefacts, contamination during handling, transport and storage. To determine the possible sources of contamination, blank filters (unexposed filters) were treated identically to and analysed alongside each batch of exposed filters, with procedural blanks tested throughout. Given that pre-washing of filters did not occur prior to sample collection, the extraction procedure was also performed on three unexposed filters in order to determine their potential contribution. The average trace metal concentrations (variation $\pm$ 20%) from the unexposed filters were subtracted from the sample leachate in order to obtain a more reliable concentration. The detection limits were calculated by using three standard deviations of a series of blanks. All detection limits were $\leq$ 10%.

4.2.5 Comparison to ambient air

The background aerosol trace metal concentrations had previously been characterised over a 4-month period from November 2007 to March 2008 by Witt et al. (2010) according to size distribution and source region of the air mass. For context, metal concentrations in the atmosphere above Oxford were found to be intermediate between typical rural and urban sites in the UK, and concentrations of Cd, Ni and Pb were within European guidelines (EC Framework Directive 96/62/EC). Evidence of carbonaceous material from scanning electron microscopy supported the conclusion that the samples were heavily influenced by traffic pollution on an hourly timescale. It was found that the trace metal profile varied significantly according the origin of the air mass sampled.

The source regions were defined as Sectors A, B and C in Witt et al. (2010), based on air mass back-trajectories calculated using the HYbrid Single-Particle Lagrangian Integrated Trajectory (HYSPLIT) model (Stein et al., 2015). The air mass was traced for 48 h prior to collection, using an initial height of 10 m above ground level (a.g.l.), with a new trajectory initialised every 6 h. Sector A is predominantly sourced from central England and north Wales. Sector B represents the southwest of England and Atlantic sources. Sector C represents southeast England and western European sources. According to Witt et al. (2010), the highest concentrations of metals were found in Sector C, which is sourced from industrialised western Europe, London, and the southeast of England.

Given the high variability of trace metal concentrations according to sector in the urban background air, the same procedure of source apportionment was adopted for our samples to make an appropriate comparison. HYSPLIT 48 h back-trajectories for each sample during the Eyja ash event were calculated using the same starting location, initial height (10 m a.g.l.) and with a new trajectory every 6 h to cover the sampling period. The samples were then assigned to one or more sectors as per Witt et al. (2010), and a ratio of sample to background concentration was calculated.

4.3 Results and discussion

4.3.1 Trace metal concentrations during the Eyja ash event

The concentrations of aerosol trace metals with a particulate matter aerodynamic diameter less than 2.5 μm ($PM_{2.5}$) in the air over Oxford during the Eyja ash event are summarised in Table 4.2. Totals were obtained by adding together the concentrations collected on filters from each stage (size fraction) on the impactor. Total aerosol $PM_{2.5}$ trace metal concentrations range from 62.83–229.58 ng/m^3, with OxAsh 1 (16 – 17 April) containing the greatest concentration and OxAsh 20 (28 May – 3 June) containing the lowest. The median values and ranges for the sampling period compared with those for ambient air in Oxford are presented in Table 4.3. Median values, rather

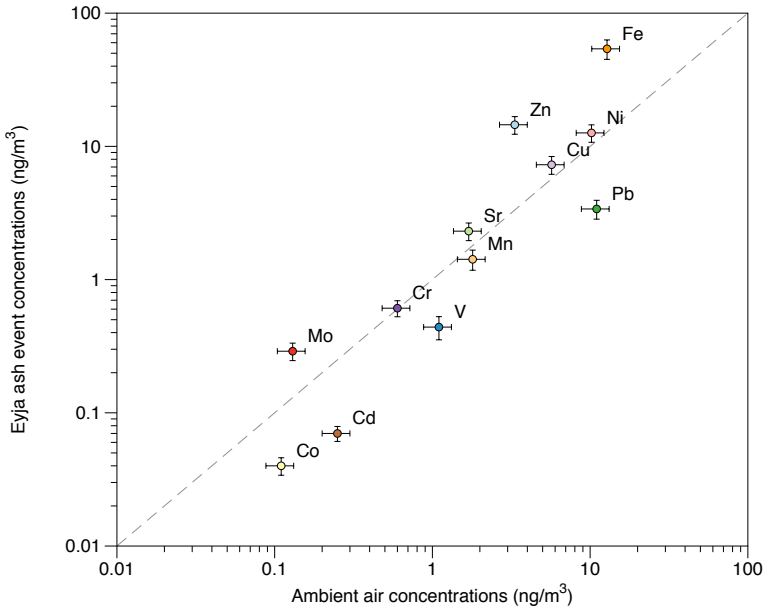

Figure 4.1: Median $PM_{2.5}$ trace metal concentrations during the Eyja ash event compared with ambient air concentrations from Witt et al. (2010). The 1:1 line is shown for reference, with those elements elevated in comparison to background concentration sitting above the line.

than the mean, have been compared due to the small sample size and wide range of the background measurements ($n = 7$; Witt et al., 2010). The concentrations in the samples from the Eyja ash event show less variability, despite a larger sample size ($n = 9$) than the background measurements (narrower range in Table 4.3), and Fe stands out as being much more elevated compared to the background concentration. Overall, Fe is the most abundant trace metal (53.97 ng/m^3), followed by Zn (14.53 ng/m^3), Ni (12.62 ng/m^3) and Cu (7.28 ng/m^3). Figure 4.1 shows that these elements are all elevated above background median concentrations. Median concentrations of Mo (0.29 ng/m^3) and Sr (2.31 ng/m^3), although lower in concentration, are also elevated above background, as displayed in Figure 4.1. The other elements are either equal to or below the median background concentrations.

4.3.2 Atmospheric crustal element concentrations

In addition to the 12 atmospheric trace metals measured in the Witt et al. (2010) study of Oxford urban background, we also measured the concentrations of Mg, Al, Ca and Ti, as these elements are abundant in crustal sources (i.e. volcanic ash). The total

Table 4.2: Total $PM_{2.5}$ Trace Metal Concentrations in Oxford, UK during the Eyja Ash Event

Sample #	OxAsh 1	OxAsh 4	OxAsh 5	OxAsh 6	OxAsh 7	OxAsh 8	OxAsh 9	OxAsh 10	OxAsh 20
Start date/time	16/04/2010 15:00	19/04/2010 15:25	20/04/2010 16:40	21/04/2010 17:00	22/04/2010 17:00	23/04/2010 17:23	26/04/2010 16:05	27/04/2010 17:20	28/05/2010 17:48
Air mass sector	A	A & C	A	A & C	A & C	B & C	B	B & C	All
V	0.40	0.71	0.12	0.39	1.42	0.75	0.44	1.33	0.40
Cr	0.36	0.61	0.50	0.48	0.69	0.31	0.96	0.64	0.75
Mn	2.84	1.13	0.93	2.13	2.91	2.97	0.79	0.78	1.42
Fe	187.12	83.04	40.05	41.84	77.75	65.85	45.72	53.97	27.62
Co	0.05	0.06	0.02	0.02	0.06	0.03	0.02	0.06	0.04
Ni	11.84	13.02	12.62	11.92	13.24	3.16	12.50	13.84	18.01
Cu	8.50	6.89	4.04	7.51	8.14	5.24	21.82	7.28	5.58
Zn	14.53	22.18	10.62	13.74	22.27	14.80	19.23	14.27	5.80
Sr	2.23	2.35	2.87	2.31	2.97	2.40	2.20	2.26	1.11
Mo	0.10	0.29	0.17	0.30	0.38	0.44	0.29	1.04	0.16
Cd	0.02	0.06	0.04	0.07	0.11	0.06	0.12	0.07	0.14
Pb	1.59	3.91	1.67	6.90	5.67	4.07	3.39	2.70	1.79
Total	229.58	134.24	73.65	87.62	135.62	100.09	107.49	98.23	62.83

Note: All times in UTC. All concentrations given in ng/m^3

Table 4.3: Median $PM_{2.5}$ Trace Metal Concentrations Compared with Ambient Air

	V	Cr	Mn	Fe	Co	Ni	Cu	Zn	Sr	Mo	Cd	Pb
Oxford Eyja Ash Event	**0.44**	**0.61**	**1.42**	**53.97**	**0.04**	**12.62**	**7.28**	**14.53**	**2.31**	**0.29**	**0.07**	**3.39**
	0.12–1.42	0.31–0.96	0.78–2.97	27.6–187.1	0.02–0.06	3.16–18.01	4.04–21.82	5.80–22.27	1.11–2.97	0.10–1.04	0.02–0.14	1.59–6.90
Ambient Air[a]	**1.10**	**0.60**	**1.80**	**12.80**	**0.11**	**10.20**	**5.70**	**3.33**	**1.70**	**0.13**	**0.25**	**11.00**
	0.2–4.1	0.3–1.7	0.5–6.5	2.1–32.7	0.03–0.62	6.9–196	1.8–18.6	0.33–63	1.3–2.5	0.1–0.8	0.02–1.1	3.9–39.6

Note: All concentrations given in ng/m^3. Median values in bold, with the range given below. [a]Witt et al. (2010)

Table 4.4: Total $PM_{2.5}$ Atmospheric Crustal Element Concentrations

Sample #	Mg	Al	Ca	Ti
OxAsh 1	143.94	166.34	328.95	3.54
OxAsh 4	103.56	134.18	472.19	1.91
OxAsh 5	151.39	109.38	447.08	1.31
OxAsh 6	89.84	91.88	467.89	1.22
OxAsh 7	139.28	116.21	608.24	1.62
OxAsh 8	71.90	52.45	411.10	0.95
OxAsh 9	101.24	105.98	356.92	0.98
OxAsh 10	86.54	108.57	389.43	1.08
OxAsh 20	58.39	351.89	162.22	0.50
Median	**101.24**	**109.38**	**411.10**	**1.22**
Birmingham, UK[a]	**20**	**8.7**	**42**	**0.31**
Whole UK[b]	20 – 100		5 – 80	

Note: All concentrations given in ng/m^3. Median values given in bold. [a]Birmili et al. (2006), [b]Werner et al. (2011)

concentrations for each of these elements are presented in Table 4.4, with data from Birmingham, UK and ranges for the whole of the UK for comparison. Data on the concentrations in Oxford urban background air were not available for these elements.

Werner et al. (2011) provided model estimates and measurements for air concentrations of base cations Na^+, Mg^{2+} and Ca^{2+} over the whole of the UK for the years 2003 and 2006. The median concentrations of Mg (0.10 μg/m^3) and Ca (0.41 μg/m^3) during the Eyja ash event are at the upper range of Mg concentration (0.02 – 0.10 μg/m^3) and exceed the upper range of Ca concentration (0.005 – 0.08 μg/m^3) by a factor of four. Measurements of urban background concentrations of Mg, Ca, Al and Ti in Birmingham, UK indicate average PM_3 values of 0.020 μg/m^3, 0.042 μg/m^3, 8.7 ng/m^3 and 0.31 ng/m^3 respectively (Birmili et al., 2006). Given that the median concentrations of these elements in our samples far exceeded the averages at other sites in the UK, it is reasonable to assume that they were elevated above background levels in Oxford because of the presence of Eyja ash. Additionally, previous studies of background trace

metal concentrations in the UK typically use more aggressive acidic solutions to leach metals from aerosol filters than used here. Therefore, for comparative purposes, the concentrations reported here are likely to be systematically lower relative to these previously measured background concentrations (Birmili et al., 2006; Witt et al., 2010). We have used a weak acidic solution (0.1 M HNO_3, pH 1) in order to quantify the fraction of trace metals that would be readily soluble in rainwater and, thus, able to have an environmental impact.

4.3.3 Source apportionment

In order to compare the samples to ambient air of the same source region (sector), HYSPLIT back-trajectories were calculated for each sample and used to assign samples to one or more sectors (Table 4.2). A ratio of the sample metal concentration to the average background metal concentration within each sector was then calculated. The air masses sampled during the Eyja ash event mostly originate from Sectors A and B, or from two or more sectors; none originate solely from Sector C (Figure 4.2). The back-trajectories of OxAsh 5 (20 – 21 April) and OxAsh 6 (21 – 22 April) (see Appendix D.3 & D.4) show that the air masses sampled were sourced directly from Iceland and so are likely to have intersected parts of the ash plume. Plots of the HYSPLIT back-trajectories calculated for each sample are also included in Appendix D.

The concentration ratios to background within each sector are shown in Figure 4.3, with values greater than one representing elevations above background, and values less than or equal to one representing concentrations at, or around, ambient levels. Figure 4.3 shows that Fe levels were significantly elevated above ambient concentrations in all samples, ranging from 1.2 to 7.3 times the average background concentration based on air-mass sector. This is consistent with other observations of elevated aerosol trace metals across Europe during the Eyja ash event (Bukowiecki et al., 2011; Schäfer et al., 2011; Lettino et al., 2012; Revuelta et al., 2012; Rossini et al., 2012; Schleicher et al., 2012; Sandrini et al., 2014). Levels of Sr and Mo were elevated in most samples,

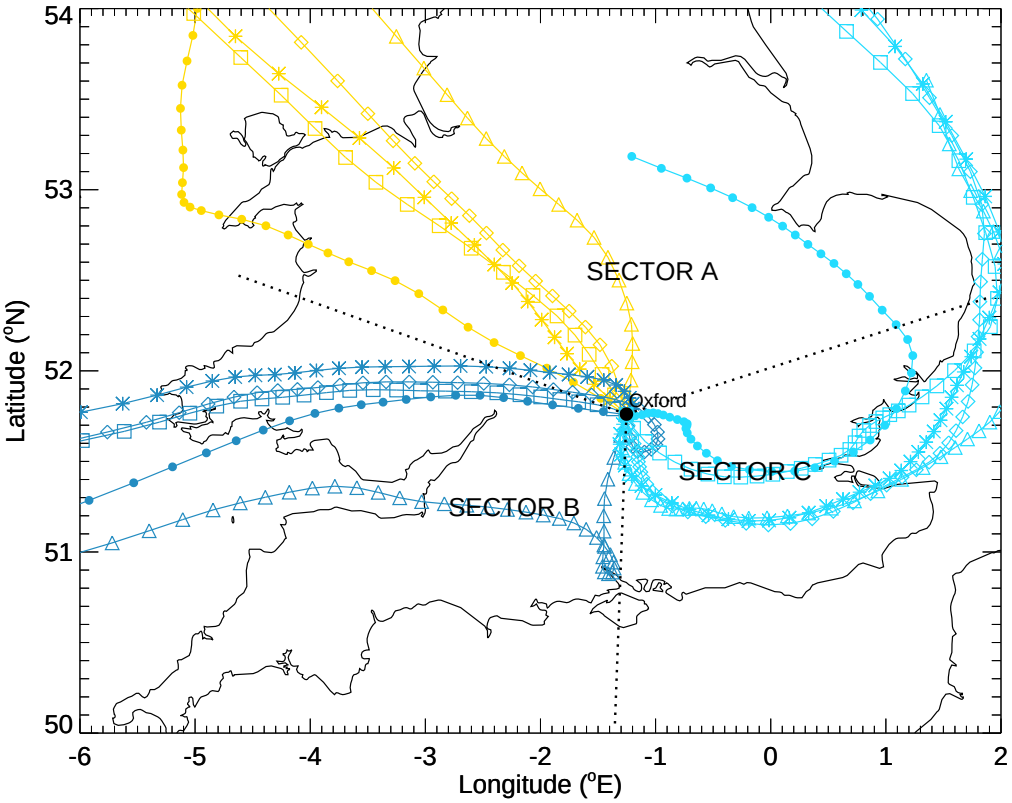

Figure 4.2: Map of the southern part of the UK showing source regions of air masses passing over Oxford (51°45'33.11" N, 1°15'20.26" W) and the delineation of each Sector (A, B & C), as defined by Witt et al. (2010). HYSPLIT back-trajectories have been plotted for three representative samples from each sector: OxAsh 5 (yellow), OxAsh 7 (light blue) and OxAsh 9 (dark blue). The back-trajectories are labelled from initiation time 0 h (triangles), -6 h (diamonds), -12 h (asterisks), -18 h (squares) and -24 h (circles). Symbols are separated by 1 h in time. The HYSPLIT back-trajectories for all samples can be found in Appendix D.

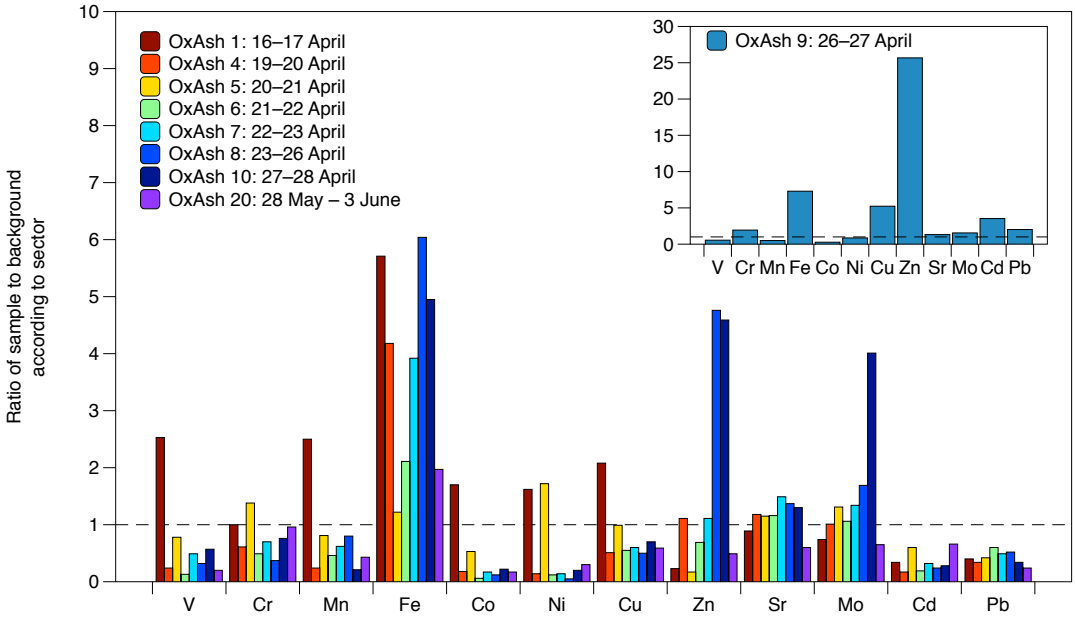

Figure 4.3: Median atmospheric $PM_{2.5}$ trace metal concentration ratios of sample to the median background values measured by Witt et al. (2010) for the appropriate air mass sector (see Figure 4.2). OxAsh 9 has concentrations far exceeding background for Zn, so is presented as an inset so as not to skew the plot.

except OxAsh 1 & 20. Elevated concentrations of V, Mn, Co, Ni and Cu were observed in OxAsh 1 (16 – 17 April), and elevated concentrations of Cr and Ni were observed in OxAsh 5. The samples OxAsh 7–10 (22 – 28 April) also contained elevated concentrations of Zn (in addition to Fe, Sr and Mo), and OxAsh 9 also had elevated Cr, Cu, Cd and Pb. Our observations of increased Cr in OxAsh 5 and 9 and Ni in OxAsh 1 and 5 are consistent with similar of observations in the composition of fallout over Rimini, Italy at around the same time (Rossini et al., 2012).

The concentration ratios of Zn > 25 times the background level in OxAsh 9 (inset; Figure 4.3) may be due to incorrect source apportionment from Sector B, which has low Zn levels (Witt et al., 2010). The HYSPLIT back-trajectory for OxAsh 9 (Figure 4.2; Appendix D.7) shows that at least some of the air swept over the boundary with Sector A, characterised by higher levels of Zn relative to the other two sectors, suggesting that there may actually be higher concentrations of Zn in the ambient air. It is also important to note that many heavy metals have shown significant decreasing trends in ambient air concentration over the period from 1980 – 2005 (Brown et al., 2008). Concentrations

of V, Mn, Fe, Zn, Ni, Cd and Pb have been falling in the years prior to the background measurements, so this may explain the lower concentrations in some of the samples which were measured two years after measurements of the ambient air in Oxford.

4.3.4 Trace metal size distributions

The size-segregated samples from Witt et al. (2010) allow a comparison with the size-segregated samples analysed in the present study. Figure 4.4 shows the size distribution of aerosol trace metals during the Eyja ash event compared with the ambient air size distributions. The trace metals were arranged into groups based on similar distributions, with those containing a coarse mode categorised as Type 1 (Fe, Sr, Mn and Cu), those with a fine mode as Type 2 (V, Ni, Cd and Pb) and those with a multimodal distribution as Type 3 (Zn, Co, Mo and Cr). In general, the size distributions of our samples are very similar to those of ambient air. The differences in the samples during the Eyja ash event are: an increase in the coarse-modes of Mn (Figure 4.4b) and Co (Figure 4.4f), an increase in the fine-modes of V, Cd (Figure 4.4d) and Mo (Figure 4.4f), and a flattening out of the distribution of Cu (Figure 4.4b), Ni (Figure 4.4d) and Zn (Figure 4.4f). The increase in Mn in the 2.5 μm fraction is consistent with observations of aerosol trace metal size distributions associated with the Eyjafjallajökull ash in Slovenia (Beeston et al., 2012). Beeston et al. (2012) also reported a peak at 1.4 μm in the size distribution of Zn. This is consistent with the observation of the flattening out of the Zn distribution in our samples compared with background. In particular, the proportion of Zn in the 1.4 μm fraction increased with a corresponding decrease in the 0.26 μm fraction relative to the ambient air size distribution. We are not aware of any observations of size distributions of V, Ni, Co and Mo in aerosol samples of the Eyjafjallajökull plume.

4.3.5 Temporal variation in aerosol composition

The concentrations of crustal elements in the aerosol samples alongside the concentration ratios to background of selected atmospheric trace elements are shown in Figure 4.5. Concentrations of the crustal elements Ca, Mg and Ti appear to be elevated

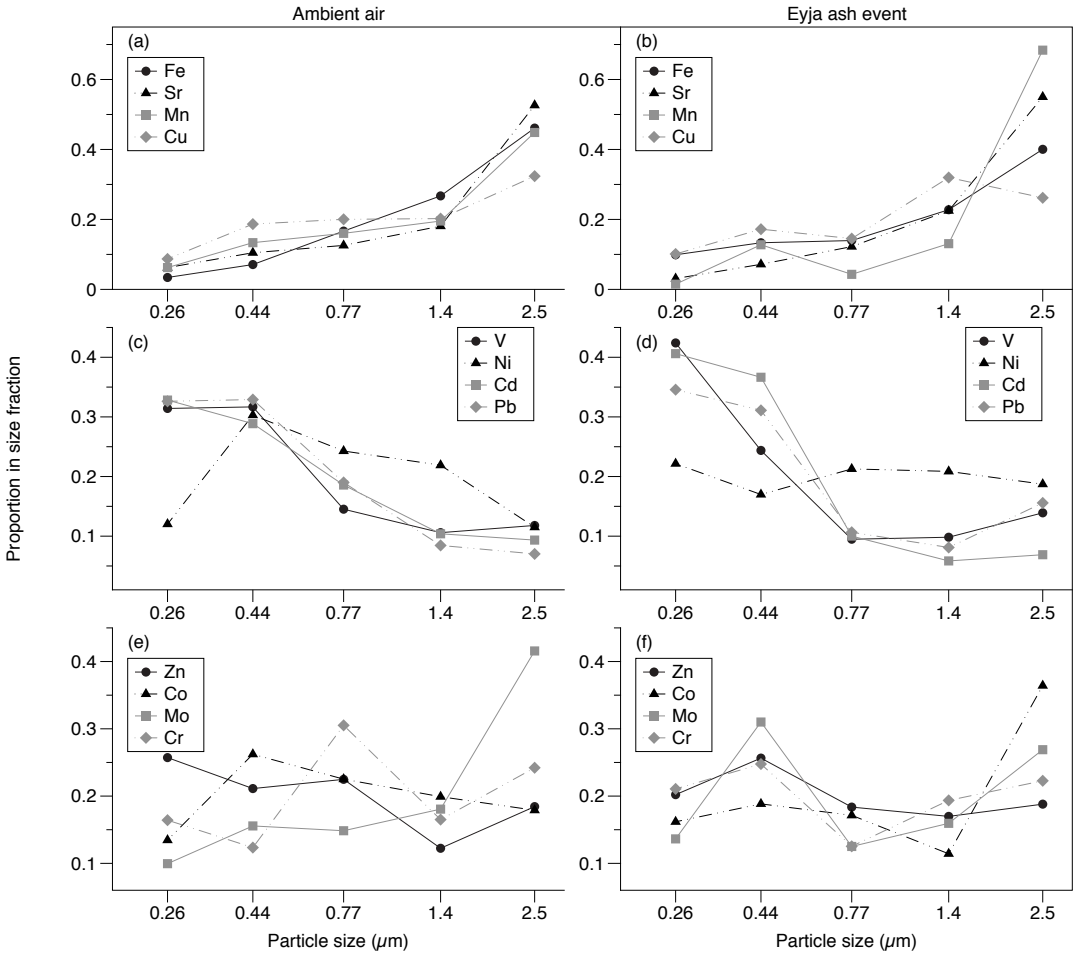

Figure 4.4: Average proportions of aerosol trace metals in size-segregated samples. Ambient air is presented on the left, with samples collected during the Eyja ash event presented on the right. Type 1 metals are shown in plots (a) and (b), Type 2 metals are shown in plots (c) and (d), and Type 3 metals are shown in plots (e) and (f).

relative to their concentration by the end of May, which is assumed to be closer to the background concentration. Without recent data on the background concentration of these elements the results can only be interpreted in a qualitative sense, but see Section 4.3.2 for a broad comparison to UK averages. Some temporal variation appears to be captured in the concentration ratios of Fe, Zn, Sr and Mo (Figure 4.5) with increasing trends through the month of April. The time series for other elements is inconclusive (see Appendix E). Interestingly, a drop in concentration ratio is observed between 19 – 21 April (OxAsh 5 & 6) in Fe, Zn and Sr. The back-trajectories for these samples show air masses source from near Iceland, however, they are very low altitude (see Figures D.3 and D.4). Samples OxAsh 7–9 (22 – 27 April) show a marked increase in the concentration ratios of Fe, Zn, Sr and Mo, where the HYSPLIT back-trajectories show air masses sourced from over Europe and the Atlantic (see Figures D.5, D.6 and D.7). This suggests that any ash falling over Oxford may have been transported via Europe. This is consistent with the satellite observations of the plume during Phase I in April being transported east of the UK (Gudmundsson et al., 2012) and with modelling experiments suggesting the plume later swept northwest over the southern part of the UK (Stohl et al., 2011).

The Eyjafjallajökull eruption provided an ideal opportunity to study the compositional evolution of a plume over large distances and using a variety of approaches with the potential to validate remote sensing methods. Geochemical and petrological analyses of the proximal tephra showed that the composition of the plume changed from a mafic end-member (benmoreite) to a more silicic end-member (trachyte) between the two intense phases Phase I & III (Sigmarsson et al., 2011; Gudmundsson et al., 2012). There was also some suggestion (Zehner, 2012) that this change may have been detected via hyperspectral remote sensing instruments using the 'concavity' index of Gangale et al. (2010). However, there is no work published to confirm this. Unfortunately, the time interval over which this change occurred (Phase III, 5 – 18 May) is not captured in our samples. In the absence of data from this phase, it is not possible to

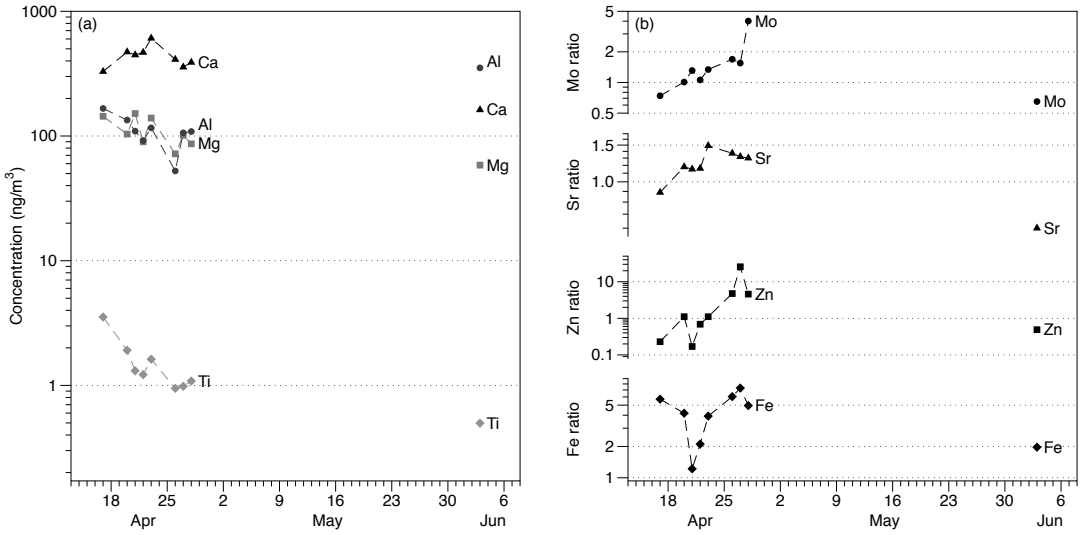

Figure 4.5: (a) Time series of atmospheric crustal element concentrations of Al, Ca, Mg and Ti. Background concentrations have not been quantified, so these can only be taken qualitatively. (b) Concentration ratios to background for Fe, Zn, Sr and Mo. Points > 1 indicate the samples are elevated above background.

further constrain the influence of differing ash type (composition) on the trace metal profile of the leachates of transported ash. The temporal component observed here can only be taken as a likely indication that the samples contain ash, further discrimination is not possible using this dataset alone.

4.3.6 Comparison with Eyjafjallajökull ash

In order to investigate the hypothesis that elevated concentrations of trace metals were the result of contamination from Eyjafjallajökull ash, we compared our samples to the composition of the ash erupted between 14 – 19 April. As element ratios are more robust than single element concentrations in unambiguously identifying a source, we have compared the ratios to Fe of our samples with those of the ash to investigate whether a volcanic signal can be detected. The relative proportions of elements in ash are likely to change during transport as a result of fractionation and sedimentation (Cashman and Rust, 2016), however, Andersson et al. (2013) found that the composition of the airborne aerosol samples collected by Rauthe-Schöch et al. (2012) was remarkably similar to that of the proximal fallout (Sigmundsson et al., 2010). The aerosol

leachate is likely to be different to the ash composition itself due to some elements being more mobile than others. Therefore, we have compared our leached aerosol samples with leachate from Eyjafjallajökull ash (Bagnato et al., 2013) as well as the bulk ash chemistry (sample SRG 2b from: `http://earthice.hi.is/eyjafjallajokull_2010_chemical_composition`; Sigmundsson et al., 2010). As would be expected, Figure 4.6 shows that the relative elemental ratios to Fe in the aerosol leachate are more similar to the ash leachate than the bulk ash.

Many of the elements fall below the equal-ratio line when compared to leached ash (Figure 4.6a), suggesting that the proportion of these elements compared to Fe are greater in the leached ash than the leached aerosol. This could be due to the influence of some contribution of background Fe in the leached aerosol samples. The proportions of Ni, Cu and Zn in the leached aerosol compared to Fe are much higher than in the bulk ash chemistry (Figure 4.6b) but are remarkably similar when compared to the ash leachate, indicating preferential leaching of these elements. This is consistent with the findings of Bagnato et al. (2013) who concluded that gas-aerosol interaction in the Eyjafjallajökull plume promoted selective leaching of cation species (Ca, Cu and Zn). These elements are likely to have been transported in the plume as halide and S-compounds on the surfaces of ash particles.

4.4 Conclusions

We have analysed a suite of size-segregated aerosol samples from Oxford, UK during the eruption of Eyjafjallajökull between 16 – 27 April and 28 May to 3 June 2010. From these samples, we were able to characterise the composition of the readily soluble trace metal components in the $PM_{2.5}$ aerosol fraction. All samples showed clear elevations in the concentrations of Mg, Al, Ca, Ti and Fe above ambient air. Additionally, we have identified increases in the concentrations of Ni, Cu, Zn, Sr and Mo above background concentrations. The size distributions of Mn and Co showed increases in the 2.5 μm fraction, while there was an increase in the fine fractions (0.26 – 0.44 μm) of V, Cd and

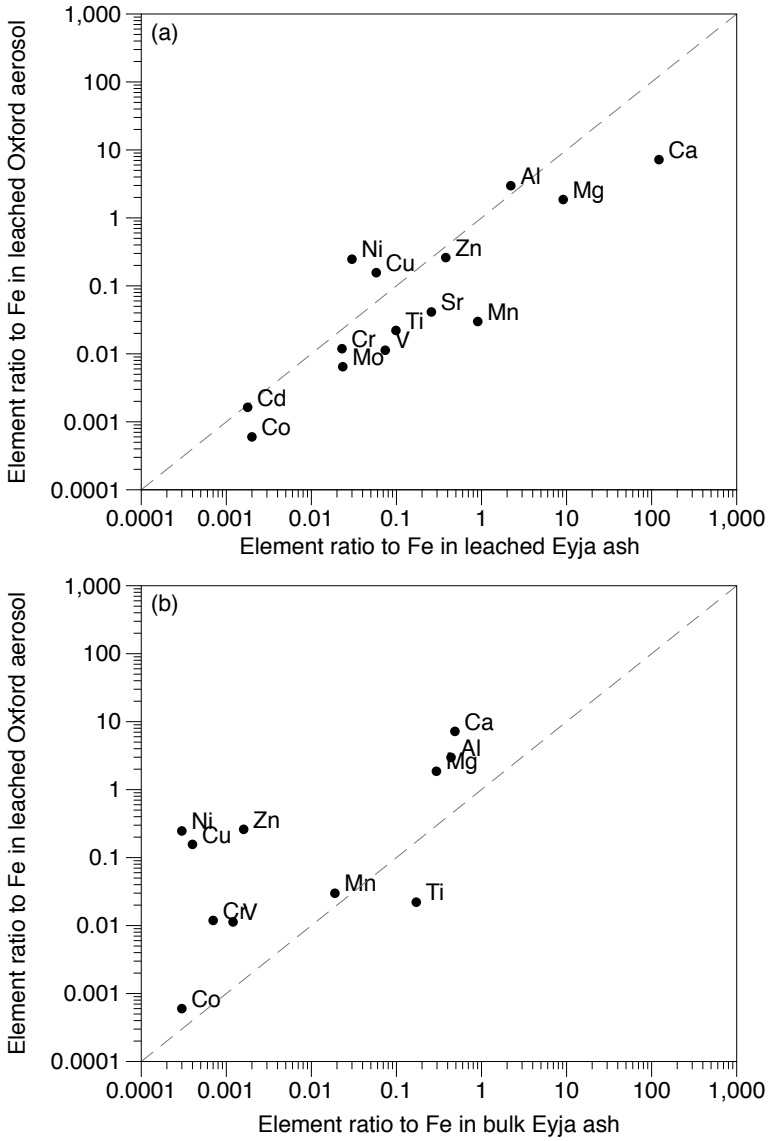

Figure 4.6: Element ratios to Fe in leached aerosol on a log-log scale compared to (a) leached Eyja ash (Bagnato et al., 2013) and (b) bulk Eyja ash (SRG 2b; Sigmundsson et al., 2010) from 14 – 19 April. Dashed line represents an equal ratio. The bulk ash chemistry can be accessed at: `http://earthice.hi.is/eyjafjallajokull_2010_chemical_composition`

Mo and an increase in the 1.4 μm fraction of Zn, which we attribute to the influence of ash. The temporal component of the dataset reveals elevated concentrations of Mg, Ca and Ti, and increasing concentrations of Fe, Zn, Sr and Mo above background through the month of April, which is likely due to the increasing influence of ash in the samples. This is consistent with satellite (Gudmundsson et al., 2012) and modelling (Stohl et al., 2011) observations over this time period. The time series is inconclusive for other elements. The similarity of the trace element profile with respect to Fe concentration compared to that of ash leachates from Eyjafjallajökull is a strong indication that the samples were affected by the ash. While other studies have shown that the plume was chemically detectable in rural or remote locations across Europe (e.g. Stevenson et al., 2012; Sandrini et al., 2014), our results indicate that the dilute ash plume was still identifiable above urban air pollution in the UK.

This event highlights the potential impact an eruption of this sort can have many thousands of kilometres from the source. Changes in composition may also be detectable and possibly able to be correlated with hyperspectral remote sensing measurements (see Section 2.4.2), however, further work to constrain the trace metal profile of leachates from different ash types is needed. Additionally, the high concentrations of Fe detected in the readily soluble aerosol fraction emphasise the importance of acidic in-plume processing to enhance availability of trace metals to the micronutrient supply in the oceans.

Chapter 5

Conclusions

This chapter synthesises the major conclusions drawn based on the research presented in Chapters 3 and 4. Recommendations for future research and suggestions for improving and extending the current research are provided.

This thesis set out to address three main aims:

1. To investigate the relationship between volcanic ash composition and its optical properties—this was addressed in Chapters 2 and 3.

2. To develop a parameterisation to estimate the spectral complex refractive index using ash composition and test its application to some satellite retrieval cases—addressed in Chapter 3.

3. To investigate the atmospheric trace metal contribution of volcanic ash to the distal environment—addressed in Chapter 4.

The major findings of Chapters 3 and 4 are summarised below.

5.1 Chapter 3: Composition and refractive index

We analysed the composition of a suite of volcanic ash samples and explored their relationship with the spectral complex refractive index. The compositional heterogeneity of our samples allowed us explore two different compositional parameters—SiO_2 content and NBO/T—and how they influence both the real (n) and imaginary (k) components

of the refractive index. The bulk ash and glass component compositions of the suite of samples investigated were compared to recent measurements of refractive index of the same samples, allowing us to better understand the controls on optical properties. By investigating the refractive index in the visible wavelength range and over a broader spectrum (0.3–19 μm) we were able to conclude the following:

1. The relationship between composition and the real part (n) of the refractive index is linear in the visible wavelength range; the composition has negligible influence on the imaginary part (k). As the wavelength increases, the strength of the linear relationship begins to weaken as the wavelength-dependency of the spectral signal becomes apparent due to absorption by bond resonances in the silicate structure.

2. We have used R^2 to elucidate areas of the electromagnetic spectrum in which a linear relationship might exist. Plotting this against wavelength, therefore, shows enough detail to be able to reconstruct the refractive index curve (n and/or k) as a function of wavelength. While it is sufficient to use wt.%SiO_2 as an input for the parameterisation, it is better to use NBO/T if the data are available, and using bulk composition is better than glass composition. This was evidenced by higher R^2 values for NBO/T and for bulk composition over a broader wavelength range. The NBO/T parameter can be used as a measure of the depolymerisation of the silicate tetrahedral network of a glass. This directly relates to the length of bonds within the structure, which manifest as absorption peaks at wavelengths that increase with the length of the bond. For silicates the salient feature is the stretching vibration of the Si—O—Si bridge between 8–12 μm.

3. We developed a new parameterisation of volcanic ash spectral refractive index over the wavelength range relevant to satellite remote sensing, 7–13 μm. Current procedures for the retrieval of quantitative volcanic ash properties rely on measurement datasets for just a few samples, which aren't necessarily appropriate

for all ash types. The parameterisation developed allows the user to choose an ash composition and generate both n and k to derive optical constants for use in radiative transfer models.

4. Using the refractive index estimates from our parameterisation, we were able to retrieve plume properties from IASI data. In comparison to the retrievals using a measured Eyjafjallajökull refractive index, the calculated indices produced generally higher estimates of ash mass loading and broadly captured a similar plume geometry. The distributions of mass loading differed to the measured index mass loadings, and generally had an associated decrease in cost function, the minimisation criterion used to assess retrieval quality.

5.2 Chapter 4: Trace metal composition of distal ash

We have characterised the readily soluble trace metal composition of ash-contaminated $PM_{2.5}$ air during the period in which the Eyjafjallajökull plume was over the UK. We used a dilute pH 1 nitric acid extraction in order to compare the readily soluble fraction of trace metals with ambient concentrations in the urban background. The major findings of this chapter were:

1. Elevated concentrations of Mg, Al, Ca, Ti, Fe, Ni, Cu, Zn, Sr and Mo were detected in the air during the period immediately following the first explosive phase of the eruption.

2. The high concentrations of Ca, Cu and Zn in the aerosol leachates point to metal sulphide scavenging processes in the eruptive plume, thereby altering the original composition of the transported ash. These elements are interpreted to be leaching from metal salts on the surfaces of the ash particles.

3. The proportions of trace metals in relation to the amount of Fe present in the aerosol samples indicated likely contamination with Eyja ash as it was remark-

ably similar to that of the known ash leachate. This "volcanic-signature" was identifiable over the urban background concentrations of $PM_{2.5}$ trace metals.

5.3 Recommendations for future work

This study focused on characterising a suite of natural volcanic ash samples, and was an important first step in understanding how composition is related to the refractive index of ash. However, in order to explore this further, an experimental study of the relationship between composition and refractive index is recommended. Laboratory-generated "volcanic ash", created through fragmentation experiments with precisely controlled compositions, could be used to investigate the effects of varying parameters on the measured refractive index. The advantage of this is that many of the variables which influence the radiative properties could be tightly controlled, including the SiO_2 content, NBO/T and crystallinity.

It is clear that volcanic particles transported through the atmosphere are not merely analogues of their equivalent deposits. The parameterisation developed in this study is based on the bulk composition of volcanic ash from deposits. This, therefore, opens up new questions as to the appropriateness of assuming a similar composition of airborne ash. The findings from Chapter 4 imply that the chemistry of airborne ash particles may be significantly different to that of the deposited ash, so further work on understanding the influence of the surface chemistry of very fine ash particles on their optical properties is recommended. Nevertheless, a parameterisation of spectral complex refractive index based on ash composition appears to be an improvement on using a standard reference refractive index, such as the Pollack 'andesite', irrespective of ash type. One possible way to immediately utilise this parameterisation would be to generate a database of spectral complex indices for the most commonly erupted compositions and/or for volcanoes which may be about to erupt. This would be a relatively quick process using the parameterisation spreadsheet provided in Appendix C.

Finally, the parameterisation developed here could be improved by adding more samples of volcanic ash with known composition and refractive indices to the database. Further work would aim to incorporate the Kramers-Krönig relation as a constraint, which would allow n to be calculated from k and vice versa. Other models, i.e. non-linear models, could also be explored for specific wavelength ranges.

5.4 Final remarks

The main outcome of this thesis has been to provide a new method to estimate the spectral complex refractive index for the quantitative remote sensing of volcanic ash. It is hoped that this tool will be used in future to provide more accurate estimates of ash mass loading. In doing this, the tool can be tested and improved on. Integrating direct sampling techniques, such as chemical analysis of airborne ash, with remote sensing techniques (ground-based or satellite) will provide vital ground-truthing and be an essential step in closing the gap in our understanding of volcanic ash in the atmosphere.

Appendix A

Artificial cloud test confirms volcanic ash detection using infrared spectral imaging

Author Contributions

A.J.P. developed AVOID and designed the airborne ash trial. A.J.P. also devised the ash detection algorithm and performed the radiative transfer calculations. F.D. led the AIRBUS project team and together with I.D., M.B. and M.W. provided the logistics for conducting the airborne experiment. K.W. and A.V. conducted and analysed the OPC measurements, and coordinated the DA42 flights. The electronics, software and hardware for AVOID were developed by C.B. and A.J.P. A.J.P., D.M. and H.E.T. processed the AVOID data. Avionics data analysis was conducted by D.M. and M.W. **The ash sample was** collected by I.D. and **analysed by G.S.P.** and T.A.M. J.C. and M.B. designed the mechanism for dispersing the ash from the A400 M. The lead author and all co-authors participated in the the experimental trials, except for T.M.

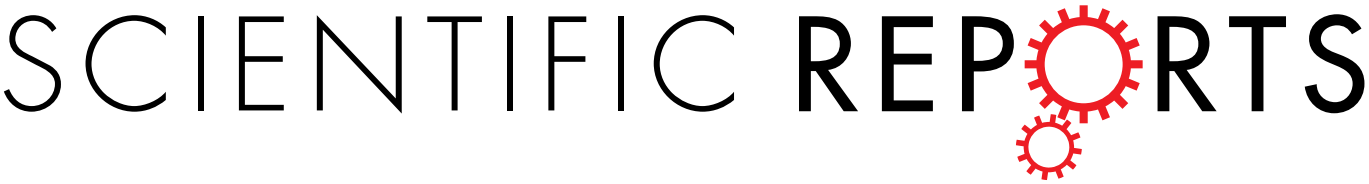

OPEN

Artificial cloud test confirms volcanic ash detection using infrared spectral imaging

Received: 27 November 2015
Accepted: 19 April 2016
Published: 09 May 2016

A. J. Prata[1,2], F. Dezitter[3], I. Davies[4], K. Weber[5], M. Birnfeld[6], D. Moriano[1], C. Bernardo[1], A. Vogel[5,7,8], G. S. Prata[9], T. A. Mather[9], H. E. Thomas[1,10], J. Cammas[6] & M. Weber[3]

Airborne volcanic ash particles are a known hazard to aviation. Currently, there are no means available to detect ash in flight as the particles are too fine (radii $< 30\ \mu$m) for on-board radar detection and, even in good visibility, ash clouds are difficult or impossible to detect by eye. The economic cost and societal impact of the April/May 2010 Icelandic eruption of Eyjafjallajökull generated renewed interest in finding ways to identify airborne volcanic ash in order to keep airspace open and avoid aircraft groundings. We have designed and built a bi-spectral, fast-sampling, uncooled infrared camera device (AVOID) to examine its ability to detect volcanic ash from commercial jet aircraft at distances of more than 50 km ahead. Here we report results of an experiment conducted over the Atlantic Ocean, off the coast of France, confirming the ability of the device to detect and quantify volcanic ash in an artificial ash cloud created by dispersal of volcanic ash from a second aircraft. A third aircraft was used to measure the ash *in situ* using optical particle counters. The cloud was composed of very fine ash (mean radii ~10 μm) collected from Iceland immediately after the Eyjafjallajökull eruption and had a vertical thickness of ~200 m, a width of ~2 km and length of between 2 and 12 km. Concentrations of ~200 μg m^{-3} were identified by AVOID at distances from ~20 km to ~70 km. For the first time, airborne remote detection of volcanic ash has been successfully demonstrated from a long-range flight test aircraft.

Fine (radii $< 30\ \mu$m) airborne volcanic ash is composed of irregular shaped minerals and glass components with an SiO_2 content ranging from 40% to 80%[1]. Copious amounts of ash can be emitted high into the atmosphere from even moderate-sized volcanic eruptions, where the atmospheric circulation can transport it 100 s to 1000 s km, intersecting commercial air routes and presenting a major hazard to aviation[2–5]. During the April and May 2010 eruption of Eyjafjallajökull, European aviation was grounded for five days causing large economic and societal impacts with estimated losses of US$5bn to the global economy[6,7]. Volcanic ash damages jet engines as the glassy components undergo a phase transition between temperatures of 700 and 1100 °C[8], becoming plastic in the hot sections of the turbine[9]. Upon liquefying, the glass sticks to metallic surfaces, reducing engine efficiency and potentially clogging inlets/outlets. Although a reduction in engine temperature will result in the glass solidifying, fracturing and clearing the metal surfaces, this is still an extremely undesirable occurrence. Volcanic ash particles can also migrate through the engine without liquefying, blocking inlets/outlets and abrading engine components. Other deleterious effects that have been identified include: clogging the air bleed filter system with consequent loss of pressurisation, short circuit and intermittent failure of electronic components, and obstructing the pitot-static system leading to unreliable speed indications[2,3]. Some, or all, of these effects can lead to an in-service event causing engine damage or engine power loss and potential loss of aircraft, passengers and crew. At least two incidents[9,10] due to volcanic ash encounters, have led to loss of power to all engines but, as yet, no air crashes have been attributed to a volcanic ash encounter. General aviation has been concerned with the hazard from airborne ash for at least 30 years, and following the June 1991 eruption of Pinatubo, Philippines, the International Civil

[1]Nicarnica Aviation AS, Vollsveien 9-11, N-1366 , Lysaker, Norway. [2]Visiting scientist, Department of Atmospheric, Oceanic and Planetary Physics, University of Oxford, UK. [3]AIRBUS Operations SAS, Toulouse, France. [4]easyJet plc, Luton, UK. [5]Department for Mechanical Engineering, Düsseldorf University of Applied Sciences, Düsseldorf, Germany. [6]AIRBUS SAS, Toulouse, France. [7]Section for Meteorology and Oceanography, Department of Geoscience, University of Oslo, Norway. [8]Atmosphere and Climate Department, Norwegian Institute for Air Research, Kjeller, Norway. [9]Department of Earth Sciences, University of Oxford, UK. [10]Visiting Scientist, School of Earth Sciences, University of Bristol, BS8 1RJ. Correspondence and requests for materials should be addressed to A.J.P. (email: fp@nicarnicaaviation.com)

Aviation Organisation (ICAO) established nine Volcanic Ash Advisory Centres (VAACs), located within meteorological watch offices to guide global aviation. These centres utilize data from ground-observers, volcano observatories, pilot reports, satellite, ground and airborne instruments (where available) and dispersion model forecasts to provide volcanic ash advisories for civil aviation[11]. Ash clouds are difficult or impossible to detect by eye[12]. The unpredictability of volcanic eruptions and the lack of information on the quantity, size distribution, composition, shape and height distribution of ash emitted to the atmosphere during eruptions mean that quantitative information on ash concentrations is uncertain[12]. The significant hazard that ash presents to aviation coupled with poor knowledge of ash concentrations has led to a very cautious approach to the problem, with significant disruption to air traffic during ash incursions on airspace.

An airborne, fast sampling (~1 Hz), dual-wavelength (spectral) uncooled infrared imaging camera system has been developed to test its ability to detect and quantify ash in the atmosphere from distances of up to 100 km. The Airborne Volcanic Object Imaging Detector (AVOID) is designed for use at typical cruise altitudes (34,000–42,000 ft or 10–16 km) and speeds (~900 km hr^{-1}) and views the atmosphere ahead of the aircraft. The system utilises two wavelength regions to detect the signature of SiO_2 in the ash particles, and permit discrimination from other meteorological clouds of water vapour, water droplets and ice crystals. The basis of the method has been described in several publications[13–16] and a similar detection scheme using satellite measurements is employed by the VAACs. A prototype system was tested using a light aircraft at Mt Etna and Stromboli volcanoes, Italy during November 2011, where it was taken to 12,000 ft altitude and eruption clouds from both volcanoes were imaged. In July 2012 the system was pod mounted on the side of the fuselage of an AIRBUS A340 flight-test aircraft. During these tests, AVOID was flown at speeds of up to 960 km hr^{-1} and reached altitudes of 38,000 ft. Imagery of meteorological clouds was acquired at 1 Hz frequency from the forward looking cameras and an algorithm used to determine the nature of the clouds. Specifically, the system was being tested to identify water and ice clouds, and perform sensitivity analyses to quantify detection limits based on the noise equivalent temperature differences (NEΔTs of 50–200 mK) of the uncooled microbolometers. The ability to identify thin layers at great distances (~100 km) and to identify clouds at night was verified. A false detection rate (incorrectly identifying pixels as ash) of 7% was determined in the ash-free atmosphere. This rate can be easily reduced to 0% by selecting different thresholds in the algorithm, however without a test in an ash environment, altering thresholds may reduce positive detection of ash. Also, during these tests, the system was flown on a long traverse towards the Canary Islands, where a boundary layer windblown desert sand was correctly identified using the same algorithm that exploits the 'reverse absorption' effect[13] due to SiO_2 at the two AVOID wavelengths. Desert sand presents a signature that is similar to volcanic ash in the AVOID system, because of its high SiO_2 content. While AVOID cannot distinguish airborne ash from windblown sand, both are hazardous to aviation and windblown sand is mostly found at much lower altitudes than volcanic ash.

Following these successful trials, it was decided that the system should be tested at an ash producing volcano. However, the logistical constraints on the A340 aircraft and availability of reliable ash producing eruptions with columns reaching heights of 10,000 ft or higher made it extremely difficult to plan and conduct such an experiment. Instead, a desk study showed that it was feasible to generate a small ash cloud in the atmosphere at a predetermined place and time without compromising air safety or affecting the environment. Approximately 1000 kg of fine ash with a size distribution having a mean radius of 10 μm and geometric standard deviation $\sigma = 1.8$ was injected into the atmosphere at an altitude of ~12,000 ft from an AIRBUS A400M flight-test aircraft executing an upward spiral flight path, over a small region of sea in the Bay of Biscay (Fig. 1). The ash formed a thin layer ~200 m deep and quickly dispersed horizontally to form an ash cloud approximately 2 km wide and 12 km long, but was not visible to the eye or to visible wavelength cameras (Fig. 1a). Within 30 minutes of the ash cloud layer forming, the A340 aircraft carrying the AVOID instrument flew towards it from approximately 80 km distance at an altitude of 15,000 ft (Fig. 1b, flight run 1). The aircraft turned at approximately 20 km from the location of the ash layer. Three further approaches were made toward the ash layer from altitudes of 10,000 ft (flight run 2), 5,000 ft (3) and 5,000 ft (4). The purpose of these flight runs was to image the ash from above, along the limb and from below. During the injection of the ash into the atmosphere, the ash layer was initially visible to the naked eye, but within a few minutes it was no longer possible to identify the layer. In order to obtain verification of the AVOID measurements of the ash layer, a small aircraft (a Diamond DA42 MPP) equipped with optical particle counters (OPCs) flew into the ash layer and made *in situ* measurements of the ash.

Ash was identified by the AVOID system on three of the four flight runs; no ash was detected from 15,000 ft because the ash layer was too low to be within the field of view of the cameras. On flight runs 3 and 4 (5,000 ft) it was possible for AVOID to identify the small aircraft flying within the ash layer. AVOID first reliably identified the layer from a distance of ~67 km. At that distance individual camera pixels measure ~10×10 m^2, giving approximately 20 vertical pixels for the layer ~200 m deep. Mass loadings along the line of sight of the instrument were calculated (see Methods) and ranged from 0.1 g m^{-2} to 1.6 g m^{-2}. These convert to concentrations of ~200–3200 μg m^{-3}, using an ash cloud width of ~2 km, as measured by the DA42. Figure 2, Panel (a) shows the times when ash was detected during flight run 3. Detections are only possible when the field of view of the instrument, indicated by the hatched region, intersects the location of the ash cloud centred at ~11,000 ft. Because the attitude of the aircraft is changing, the field of view coverage changes and corrections must be applied to the mass loading retrieval to account for optical path changes. Panel (b) shows a single processed image frame from AVOID (movie loops for all four runs are provided in the Supplementry Materials), indicating the location and mass loading of the ash layer. The DA42 *in situ* measurements, shown as solid circles, have been collocated onto the image and their size is proportional to the mass concentrations measured by the OPC. Panel (c) shows a summary of detections from three flight tracks at ranges from 10–65 km. Assuming a homogeneous ash layer ~200 m deep by ~2 km wide and ~12 km long (see Methods), we can calculate the theoretical detection probability for the imaging device at varying distances from the cloud. This can be compared with the actual detection, expressed

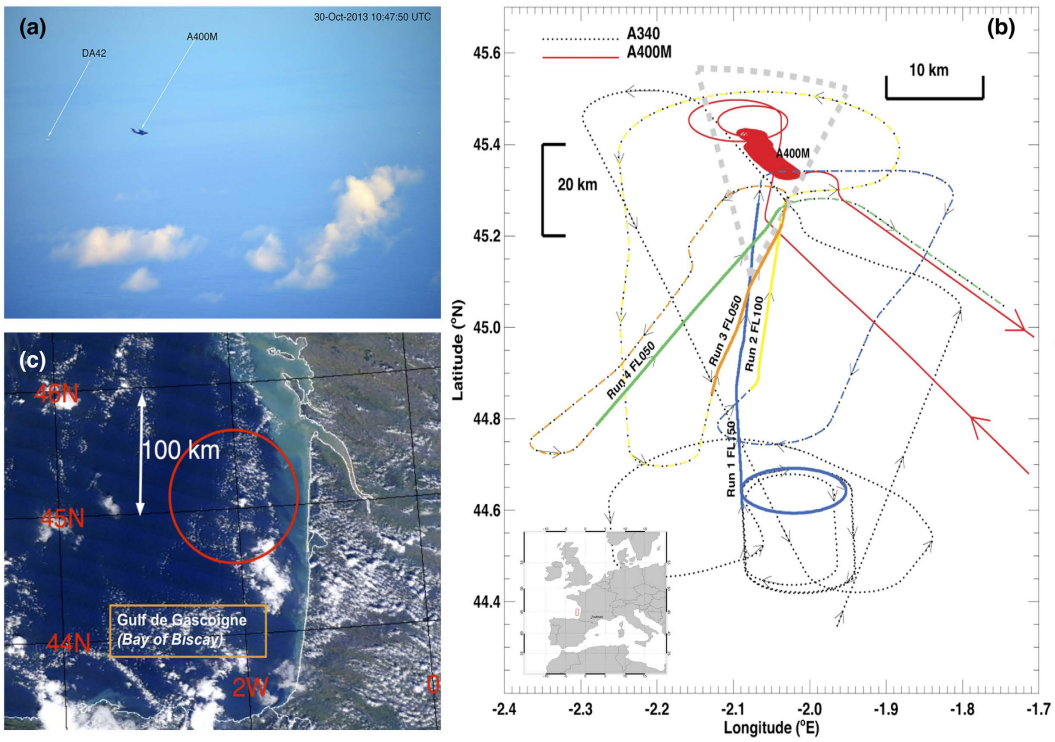

Figure 1. (**a**) Photograph taken from the A340 showing the A400M dispensing ash into the atmosphere. The DA42 can also be seen sampling part of the dispersing ash layer. (**b**) Locations of the A340 aircraft runs. The track of the A400M, dispensing the ash, is shown as a red solid line; the A340 tracks are shown as broken lines and colour coded as follows: blue = run 1, flight level 150 (15,000 ft); yellow = run 2, flight level 100 (10,000 ft); orange = run 3, flight level 050 (5,000 ft); green = run 4, flight level 050. The arrows indicate the direction of travel of the aircraft. The grey-coloured thick-dashed lines show the approximate horizontal field-of-view of the AVOID cameras. Inset map shows the geographic location of the experiment. (**c**) Satellite image (MODIS/Aqua: http://rapidfire.sci.gsfc.nasa.gov/cgi-bin/imagery/realtime.cgi?date=2013303) acquired ~30 minutes after the ash was first inserted into the atmosphere. The ash layer was not detectable at the spatial resolution (250 m) of the visible channels of the MODIS instrument. The map was drawn using the IDL v8.2 software package (www.exelisvis.com). The MODIS data are courtesy of NASA/GSFC and processed using IDL v8.2.

as a percentage of the total number of pixels within the field of view of the cameras. The results indicate very good detection (compared to the theoretical curve) for distances from ~25 to 60 km. The theoretical detection threshold takes no account of inhomogeneities in the ash cloud or changes in the pitch of the instrument that affect the path length and hence mass loading sensitivity. As the aircraft approached within 20 km of the cloud, the imager began to observe the cloud from increasingly large viewing zenith angles, reducing the path length and also observing through the centre of the ash cloud, which contained concentrations below the limit of detection of AVOID, $<\sim 100\ \mu g\,m^{-3}$ for ash cloud thicknesses of ~2000 m. Hence at distances of ~20 km from the cloud ash detection was problematic.

The vertical depth of the ash layer was verified by descending and ascending the DA42 until negligible particles were counted. The AVOID measurements suggest a descent of the ash layer of $\sim 0.3\ m\,s^{-1}$ (Fig. 3a), broadly consistent with terminal velocities for spherical particles of density $\sim 2600\ kg\,m^{-3}$. The distribution of mass determined from the OPC measurements indicates two peaks: a background peak near $70\ \mu g\,m^{-3}$ and a second peak near $400\ \mu g\,m^{-3}$, associated with the ash cloud (Fig. 3b). These measurements (Fig. 3c) also show that the layer was not more than ~300 m deep. The OPCs measured ash concentrations between $100\ \mu g\,m^{-3}$ to $6000\ \mu g\,m^{-3}$ with a very high degree of heterogeneity in the cloud (Fig. 3c). The smaller range of concentrations (~100 to $\sim 600\ \mu g\,m^{-3}$) measured by AVOID compared to the OPCs may be a consequence of the averaging process of the imager and is also due to the assumption of a uniform width of the ash cloud.

The sensitivity of the AVOID system depends on the mean effective radius of the ash size distribution and the composition of the ash. We measured the ash size distribution before and after the experiment and found no discernible difference in the mean radius (~10 μm). The composition of the ash was measured before the experiment; the sample had a complex structure (Fig. 4a) and contained a significant glassy proportion (Fig. 4b). The composition was dominated by SiO_2 (Fig. 4c).

The identification of an ash layer embedded within an atmosphere containing meteorological clouds from distances of up to ~60 km, provides a warning time of 4 minutes for an aircraft travelling at $900\ km\,hr^{-1}$. This is sufficient time to make a gradual change in course direction and avoid intersecting the ash layer. Using the Caliop (Cloud-Aerosol Lidar with Orthogonal Polarisation) lidar and AIRS (Atmospheric Infrared Sounder) satellite instrument data, it was found that during the Eyjafjallajökull, Chaitén (May 2008), Sarychev Peak (June, 2009),

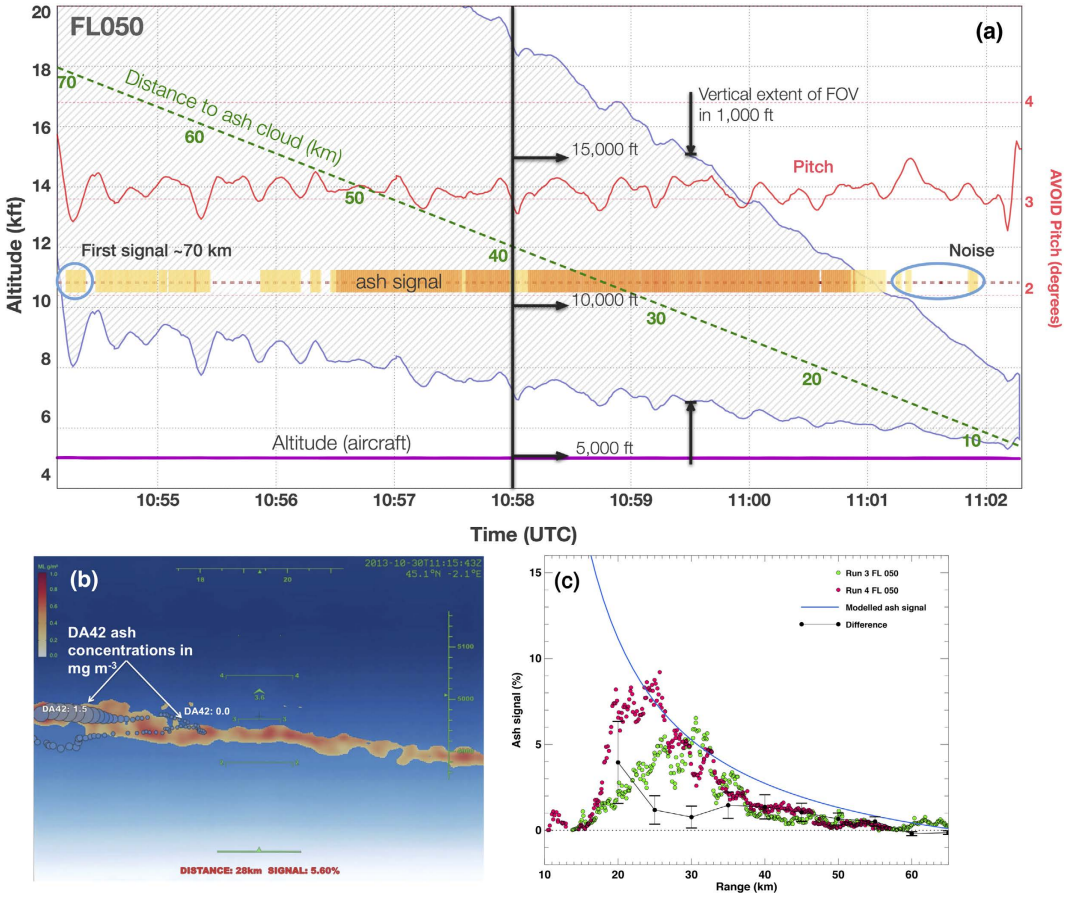

Figure 2. (**a**) Ash signal observed by the dual infrared camera imaging system, AVOID on board the A340 test aircraft from 5000 ft (FL050) viewing the ash cloud at ~11,000 ft from distances of ~70 km. The vertical field-of-view of the system is shown as the hatched coloured region, the A340 altitude is constant at 5000 ft, while the pitch of the instrument (shown in red) undergoes small changes. The total time interval is ~8 minutes. The ash signal is shown in shades of yellow (weaker signal) and orange (stronger signal). The solid vertical line at 10:58 UT corresponds to the time when the DA42 was sampling inside the ash cloud and a vertical profile at this time is shown in Fig. 3(a). (**b**) A single AVOID image frame showing the ash detection signal (yellow/orange) and coincident ash concentrations measured by the DA42 (filled circles). The background shows brightness temperatures from the reference channel in shades of blue to white (cold to warm). (**c**) Ash signal (in %; filled circles) as a function of distance (km) from the ash cloud, shown for two flight runs. The signal is defined as the ratio of the number of pixels identified as ash to the total number of pixels, expressed as a percentage. The solid blue curve shows a theoretical detection limit based on the geometry of the cloud, the pixel resolution (distance dependent) and perfect detection of ash regardless of the amount. The difference between the measured signal and the theoretical estimates is shown every 5 km (black circles) with the standard deviation over 5 km also shown. Beyond 25 km the difference is at or below 1%.

Puyehue-Cordón Caulle (June, 2011) and Calbuco (April 2015) eruptions the ash layers were thin; ranging from 500 m to 3000 m deep[17,18]. Ground-based[19,20] and airborne[21,22] lidar measurements and modelling[23,24] of dispersing ash layers also support this finding.

Near real-time satellite detection of ash clouds is currently used by VAACs and dispersion and transport models are used to forecast their concentration and movement. However, dispersing ash clouds forming in thin layers (<~2000 m) may not be detected by satellite instruments, and may not be vertically resolved by current dispersion models. While satellite data and model forecasts can provide strategic information for airlines to plan their operations[5], uncertainties in eruption source parameters coupled with uncertainties in forecast wind measurements lead to errors in the forecast ash cloud location[11]. Furthermore, the recent eruption of Kelut volcano, Indonesia on 13 February 2014 demonstrated that even with good information on the location and timing of the eruption, it did not prevent a commercial aircraft from encountering an ash layer and damaging its engines. In this case, the encounter occurred in low light, in an ash layer that was hidden from the satellites' view by a larger ash umbrella cloud. Modelling[25] showed that the aircraft likely encountered this cloud for several minutes and that ash concentrations ranged from 2000 $\mu g\,m^{-3}$ to 9000 $\mu g\,m^{-3}$. An airborne detection system would have alerted the aircraft and allowed a timely and safe routing option for the aircraft to avoid an encounter with the ash cloud.

The results from this experiment successfully demonstrate remote detection of ash clouds using thermal imaging cameras. An earlier experiment in skies containing no ash gave a false detection rate of ~7%, but with some

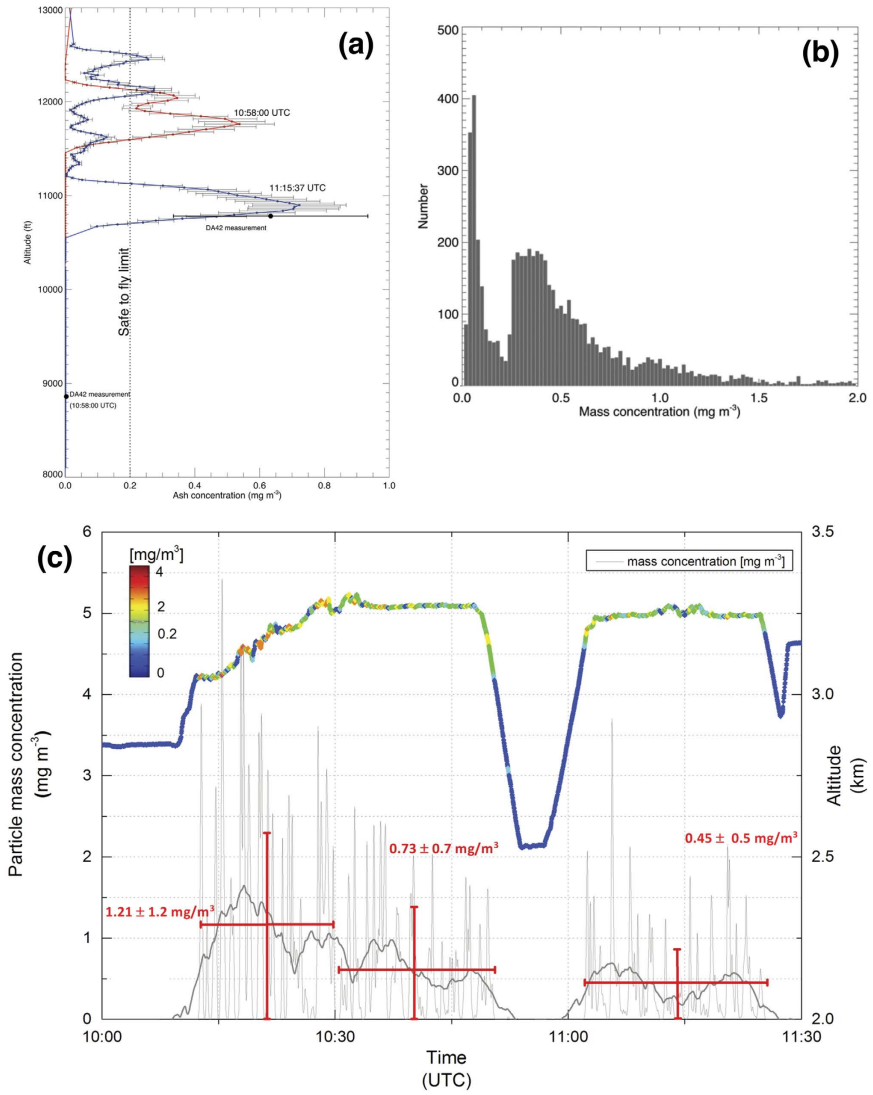

Figure 3. (**a**) AVOID measurements at two times: 10:58:00 UTC when the DA42 aircraft had descended below the ash layer, and 11:15:37 UTC when the DA42 was flying within the ash layer. The ash layer was thin (<300 m deep) and multilayered. (**b**) Histogram of the mass concentration measured by the OPC showing a peak at around ~70 $\mu g\,m^{-3}$ representing the background particulate concentration and a broader peak between 250 and 450 $\mu g\,m^{-3}$ representing the ash layer concentration. (**c**) *In situ* OPC measurements of the airborne ash made during the experiment. The upper line shows the altitude of the DA42 aircraft, with colours representing the particle mass concentration. Particle mass concentration ($mg\,m^{-3}$) is plotted as a function of time for a period when the AVOID system was viewing the ash layer. Between 10:50 and 11:00 UTC the aircraft descended until negligible particles could be counted, and the layer depth at this time is estimated to be ~280 m. Over a period of ~1 hour the mean concentration dropped from 1200 to 450 $\mu g\,m^{-3}$.

fine tuning of the thresholds used in the algorithm, improvements in the sensitivity of uncooled bolometric detectors and judicious choice of the bandpasses used for filtering the radiation this rate can be reduced to below 3%. This experiment used a very small ash cloud (<10% of pixels contained ash) and when compared with the expected theoretical signal, we have shown that if >1% of pixels contain ash then a positive detection can be made. It is stressed however, that this experiment was conducted at the relatively low altitude of ~11,000 ft; at higher altitudes atmospheric conditions will be different and the bandpasses for the two cameras will require optimisation. The composition of the ash is also an important factor affecting the sensitivity of detection in the thermal infrared, since the silicate content and 'glassiness' of the ash determine the variation of extinction of radiation as a function of wavelength[26]. The mineral composition of the Eyjafjallajökull sample used in this experiment was measured and had a high SiO_2 content (Fig. 4c). Some of the particles were highly irregular, possibly due to interaction with water during the fragmentation process (Fig. 4a,b). Radiative transfer modelling is currently underway to determine the optimal filter positions to ensure maximum ash detection for a range of ash compositions and shapes for thin ash layers in the altitude range of 5,000 ft to 45,000 ft, while also minimising the false detection rate.

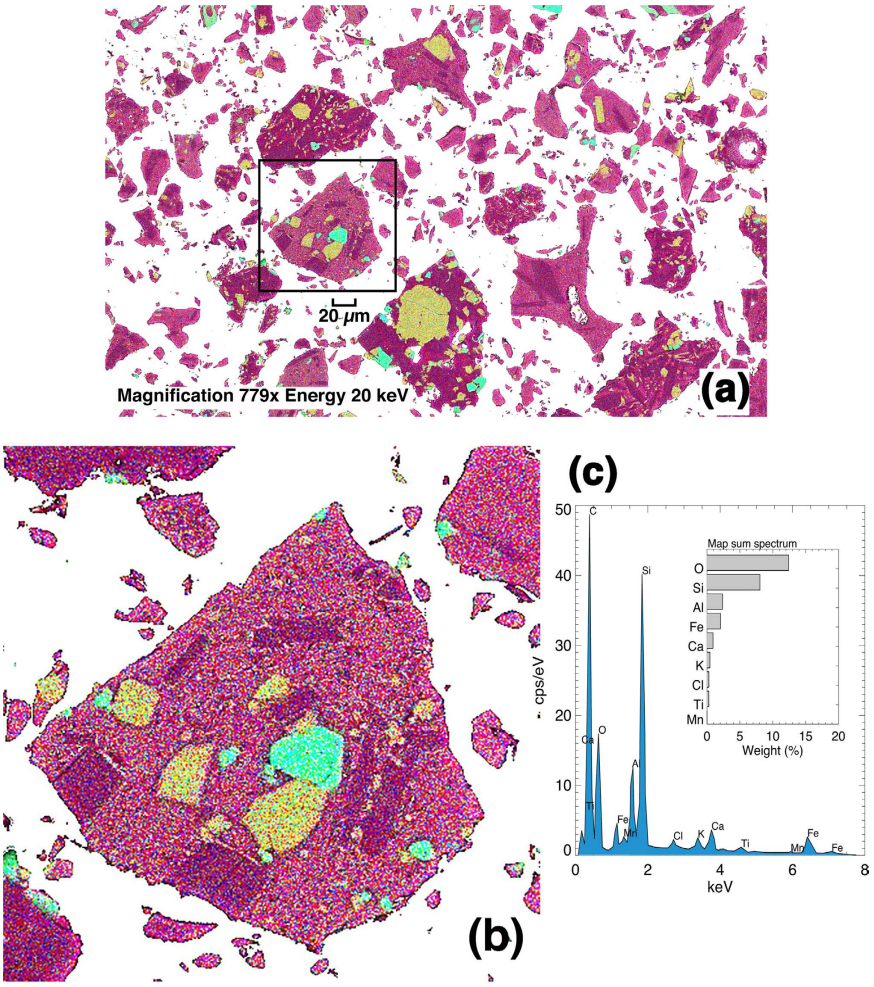

Figure 4. (**a**) Energy Dispersive X-ray Spectroscopic (EDS) elemental map of the Eyjafjallajökull ash sample. The influence of water during fragmentation has resulted in the blocky and irregular shapes of the particles. (**b**) A magnified portion of the image showing the highly complex mixture of elements contained in the various crystalline and glassy structures. The colours represent counts of each of the following elements in order of abundance: red = Si, blue = Al, green = Fe, yellow = Ca, magenta = K, and cyan = Ti. The crystals dominated by Ca (yellow) are Ca-rich pyroxene (augite), crystals dominated by Fe and Ti (green and cyan) are ilmenite, crystals highlighted by a lack of Ca (yellow) and presence of Al (blue) and K (magenta) are most likely a Al-K-rich plagioclase (orthoclase). These crystals are set in an amorphous groundmass of glass. (**c**) Spectrum of counts per second per electron volt. These energies allow identification of elements and their semi-quantitative proportions.

Methods

Volcanic ash. In March 2013 1000 kg of fine ash was sourced from deposits of Eyjafjallajökull ash collected by the University of Iceland shortly after the 15 April, 2010 eruption. The ash was transported to Toulouse, France and stored in 25 kg containers. The ash was milled to remove larger particles, more representative of ash transported over long distances (>~1000 km). Samples of this ash were analysed at the University of Oxford to provide composition (Fig. 4) and size distribution information.

AVOID installation. The AVOID system was deployed in an aerodynamic pod, mounted on the port side of an AIRBUS A340 flight-test aircraft specially equipped to conduct experimental trials. The pod was secured onto metal plates replacing two forward windows and attached using struts. The head of the AVOID system consists of two fast sampling (~50 Hz) infrared cameras with F/1.2 optics and interference filters placed behind the lenses. Dry air is passed through the pod, but no temperature stabilisation (heater) was deployed because previous tests had shown that the pod remains warm (> −10 °C) due to heat from the cameras and associated electronics. The pod was lined internally with aluminium foil insulation pads and its humidity and temperature were monitored continuously. The cameras were protected from windblown material damage using a hard carbon coated Germanium window of 5 mm thickness. Prior to flying, the system was pre-calibrated in the laboratory using a standard blackbody and an environmental chamber to simulate the expected cold temperatures during flight at high altitude. All of the important instrumental functions were monitored continuously during the flights, including the temperature of the optics (in four locations), the focal plane array (FPA) temperature, the internal pod temperature and

humidity and the accelerations of the pod during flight using pressure transducers. Aircraft attitude data were also acquired by the AVOID system, but more accurate data from the A340 avionics system were used in the post analysis. Data were received in real time onto a control computer housed inside the aircraft and displayed onto a screen. Only an indication of the ash layer was provided during the flights; detailed analysis and corrections for aircraft attitude were applied in a post analysis. As it was impossible to visually sight the ash layer, the first indications of it were made using the AVOID data displayed on the system on the aircraft in real time. However, proper identification and analysis, including conversion of the brightness temperature measurements to mass loadings required use of a radiative transfer model and a microphysical ash model (see Radiative Transfer in Methods).

Ash deposition experiment. The generation of the ash cloud was conducted from an AIRBUS A400M flight-test aircraft. Two specially designed nozzles were used with hosepipes feeding ash from 25 kg containers mounted on racks inside the aircraft. Operators moved the hosepipes to a fresh ash container as each one was emptied into the atmosphere. The ash was forced from inside the aircraft to the outside by making use of the differential pressure. Flow rates of ~0.8 kg s^{-1} were achieved using two nozzles, and a total of 975 kg was injected into the atmosphere in 20 minutes. The ash was dispersed as the A400M climbed vertically in a tight spiral track, leaving a cloud that resembled a torus with an internal radius of ~1000 m. By the end of the measurement period (approximately 40 minutes from the start) the ash layer generated was ~200 m deep, ~2 km wide and ~12 km long, with a "hole" at its centre. Integrating over this volume the total mass estimated by AVOID is ~900 kg, while the mass estimated by integrating the OPC measurements is ~950 kg. Both estimates compare favourably with ~975 kg that was released from the A400M.

Radiative transfer. We consider a plane-parallel cloud consisting of a distribution of spherical particles within a scattering layer, and solve the following radiative transfer equation (RTE)[27]:

$$\mu \frac{\partial I_\lambda}{\partial \tau}(\tau, \mu) = I_\lambda(\tau, \mu) - (1 - \varpi_\lambda) B_\lambda(T) - \frac{\varpi_\lambda}{2} \int_{-1}^{1} P_\lambda(\mu; \mu') I_\lambda(\tau, \mu') d\mu' \quad (1)$$

where $I_\lambda(\tau, \mu)$ is the radiance measured by the sensor at wavelength λ in the direction μ. τ is the optical depth, μ is the cosine of the zenith angle, ϖ_λ is the single scattering albedo and P_λ is the axially-symmetric phase function. The cloud layer has a geometrical depth s in the direction μ. This equation can be solved numerically using appropriate boundary conditions that depend on the viewing geometry, and the radiation incident at the front and back surfaces of the ash cloud[28,29]. The parameters ϖ_λ, P_λ and β_λ, depend on the complex refractive index of the ash particles, the size distribution and their shape. We use a Mie scattering program[29] to calculate these parameters as a function of λ, using a log-normal size distribution fitted to our measurements, assuming spherical particles and refractive index data for Eyjafjallajökull ash. Once these parameters have been calculated for the bandpasses used by the AVOID cameras, the mass loading in the direction μ can be found from:

$$M_l = \frac{4}{3} \frac{\rho \tau r_e}{Q_\lambda}, \quad (2)$$

where ρ is the density of the ash, r_e is the effective particle radius, $r_e = \frac{\int_o^\infty r^2 n(r)\, dr}{\int_o^\infty r^3 n(r)\, dr}$, Q_λ is the non-dimensional Mie extinction coefficient (wavelength dependent), and $n(r)$ is the size distribution. The concentration C, (in kg m^{-3}) is the mass loading divided by the the total path $L\,(=\int_s ds/cos(\mu))$, traversed by the radiation through the cloud. For trachyandesite ash ($\rho = 2.6 \times 10^{-3}$ kg m^{-3}) in a homogeneous cloud of 100 μg m^{-3} concentration, $r_e \sim 10\,\mu$m, $Q \sim 2.5$, the vertical optical depth per kilometre $\tau/s \approx 10^{-2}/\cos\mu$. It can be seen that AVOID is sensitive to thin ash layers where $L \to 0$ because of the limb viewing capability.

***In situ* particle measurements.** The optical particle counter (OPC) was equipped in an aerodynamic measurement pod configuration for a Diamond Airborne Sensing aircraft (DA42-MPP). The measurement pod was installed on the nose of the aircraft to avoid turbulence or other aerodynamic unfavourable effects on the particle inlet. The OPC was connected to an isokinetic straight metal sample inlet tube that was constantly heated up to 10 °C. The OPC, a modified Grimm SkyOPC Model 1.129, was pre-calibrated for volcanic ash particles and consists of a focused laser beam with a fixed wavelength ($\lambda = 655$ nm) and an optical measurement cell. OPCs combine the principles of light scattering of small particles with single particle counting. By the interaction of particles with this laser band, a light pulse travels in a specific direction that depends on the size of the particle. A pin diode detects the scattered radiation signal from each particle and the downstream pulse height analyser classifies the scattered light pulse into a size distribution (0.25 to 40 μm), based on the optical and physical properties of ash particles. This particle size distribution is converted into a mass concentration of total suspended particle mass (TSP) by assuming size dependent material densities that were derived by the manufacturer. The instrument operates at a volumetric flow rate of 1.2 l/min and a time resolution of 1 s. The accuracy of these airborne particle measurements systems is $\pm$10% and is related to the measurement principle and the saturation level of up to 2.0×10^3 particles/cm^3.

References

1. Rose, W. I. & Durant, A. J. Fine ash content of explosive eruptions. *J. Volcanol. Geothermal Res.* **1(2),** 32–39 (2009).
2. Casadevall, T. J. Ed. Volcanic ash and aviation safety. *Proc. of the Firts International Symposium on Volcanic Ash and Aviation Safety* US Geological Survey Bulletin **2047**, Seattle, Washinghton, July, 1991 (1991).
3. Guffanti, M., Casadevall, T. J. & Budding, K. Encounters of Aircraft with Volcanic Ash Clouds: A Compilation of Known Incidents, 1953–2009, US Geological Survey Data Series 545, ver. 1.0, 12 p., plus 4 appendixes including the compilation database, Date of access: 5 March, 2016, (http://pubs.usgs.gov/ds/545/) (2010).

4. Prata, A. J. & Rose, W. I. Volcanic hazards to aviation. In *Encylopedia of volcanoes* 2nd Edition, Ed. Sigurdsson, H., Houghton, B., McNutt, S., Rymer, H., Stix, J. Academic Press, 1421pp. (2015).
5. Prata, A. J. Satellite detection of hazardous volcanic clouds and the risk to global air traffic. *Nat. hazards* **51(2),** 303–324 (2009).
6. Oxford Economics, The economic impacts of air travel restrictions due to volcanic ash, report, 12 pp., Abbey House, Oxford, UK (2010).
7. European Union (EU), Volcano crisis report: Report on the actions undertaken in the context of the impact of the volcanic ash cloud crisis on the air transport industry, report, 11 pp., Eur. Comm., Brussels. Available at (date of access: 18 March 2016): http://ec.europa.eu/transport/doc/ash-cloud-crisis/2010_06_30_volcano-crisis-report.pdf. (2010).
8. Kueppers, U. *et al.* The thermal stability of Eyjafjallajökull ash versus turbine ingestion test sands. *J. Appl. Volcanol.* **3,** 4 (2014).
9. Przedpelski, Z. J. & Casadevall, T. J. Impact of volcanic ash from 15 December 1989 Redoubt volcano eruption on GE CF6-80C2 turbofan engines, *In Volcanic ash and aviation safety: Proc. of the First International Symposium on Volcanic Ash and Aviation Safety*, US. Geological Survey Bulletin **2047**, 129–135, Seattle, Washington, July, 1991 (1994).
10. Hanstrum, B. N. & Watson, A. S. A case study of two eruptions of Mount Galunggung and an investigation of volcanic eruption cloud characteristics using remote sensing techniques. *Aust. Met. Mag.* **31,** 131–177 (1983).
11. Stohl, A. *et al.* Determination of time- and height-resolved volcanic ash emissions and their use for quantitative ash dispersion modeling: the 2010 Eyjafjallajókull eruption. *Atmos. Chem. Phys.* **11,** 4333–4351, doi: 10.5194/acp-11-4333-2011 (2011).
12. Wienzierl, B. *et al.* On the visibility of airborne volcanic ash and mineral dust from the pilot's perspective in flight. *Phys. Chem. of the Earth* **45–46,** 87–102 (2012).
13. Prata., A. J. Radiative transfer calculations for volcanic ash clouds. *Geophys. Res. Lett.* **16(11),** 1293–1296 (1989).
14. Prata, A. J., Barton, I. J., Johnson, R. W., Kamo, K. & Kingwell, J. Hazard from volcanic ash. *Nature* **354(6348),** 25 (1991).
15. Wen, S. & Rose, W. I. Retrieval of sizes and total masses of particles in volcanic clouds using AVHRR bands 4 and 5. *J. Geophys. Res.* **99(D3),** 5421–5431 (1994).
16. Pavolonis, M. J. Advances in Extracting Cloud Composition Information from Spaceborne Infrared Radiances: A Robust Alternative to Brightness Temperatures. Part I: Theory. *J. Appl. Meteor. Climatol.* **49,** 19922012, doi: http://dx.doi.org/10.1175/2010JAMC2433.1 (2011).
17. Winker, D. M., Liu, Z., Omar, A., Tackett, J. & Fairlie, D. CALIOP observations of the transport of ash from the Eyjafjallajökull volcano in April 2010. *J. Geophys. Res.* **117,** D00U15, doi: 10.1029/2011JD016499 (2012).
18. Prata, A. T., Siems, S. T. & Manton, M. J. Quantification of volcanic cloud top heights and thicknesses using A-train observations for the 2008 Chaitén eruption. *J. Geophys. Res. Atmos.* **120,** doi: 10.1002/2014JD022399 (2015).
19. Pappalardo, G. *et al.* Four-dimensional distribution of the 2010 Eyjafjallajökull volcanic cloud over Europe observed by EARLINET. *Atmos. Chem. Phys.* **13(8),** 4429–4450, doi: 10.5194/acp-13-4429-2013 (2013).
20. Gasteiger, J., Groß, S., Freudenthaler, V. & Wiegner, M. Volcanic ash from Iceland over Munich: mass concentration retrieved from ground-based remote sensing measurements. *Atmos. Chem. Phys.* **11(5),** 2209–2223, doi: 10.5194/acp-11-2209-2011 (2011).
21. Schumann, U. *et al.* Airborne observations of the Eyjafjalla volcano ash cloud over Europe during air space closure in April and May 2010. *Atmos. Chem. Phys.* **11(5),** 2245–2279, doi: 10.5194/acp-11-2245-2011 (2011).
22. Weber, K. *et al.* Airborne *in-situ* investigations of the Eyjafjallajʼókull volcanic ash plume on Iceland and over North-Western Germany with light aircrafts and optical particle counters. *Atmos. Environ.* **48,** 2012, 9–21, doi: 10.1016/j.atmosenv.2011.10.030 (2011)
23. Marenco, F. *et al.* Airborne lidar observations of the 2010 Eyjafjallajókull volcanic ash plume. *J. Geophys. Res.* **116,** D00U05, doi: 10.1029/2011JD016396 (2011).
24. Dacre, H. F. *et al.* Volcanic ash layer depth: Processes and mechanisms. *Geophys. Res. Lett.* **42,** 637–645, doi: 10.1002/2014GL062454 (2015).
25. Kristiansen, N. I., Prata, A. J., Stohl, A. & Carn, S. A. Stratospheric volcanic ash emissions from the 13 February 2014 Kelut eruption. *Geophys. Res. Lett.* **42,** 588–596, doi: 10.1002/2014GL062307 (2015).
26. Grainger, R. G. *et al. Measuring volcanic plume and ash properties from space* Geological Society, London, Special Publications, 380(1), 293320, doi: 10.1144/SP380.7 (2013).
27. Liou, Kuo-Nan *An introduction to atmospheric radiation*. Vol. 84. Academic press (2002).
28. Stamnes, K. & Swanson, R. A. A new look at the discrete ordinates method for radiative transfer calculations in anisotropically scattering atmospheres. *J. Atmos. Sci.* **38,** 387–399 (1981).
29. Evans, B. T. N. An interactive program for estimating extinction and scattering properties of most particulate clouds. *Department of Defence Report* MRL-R-1123, Defence Science and Technology Organisation, Materials Research Laboratory, P.O. Box 50, Ascot Vale, Victoria 3032, Australia (1988).

Acknowledgements

G.S.P. and T.A.M. acknowledge funding from the NERC SHIVA project NE/J023310/1 and the NERC Centre for the Observation and Modelling of Earthquakes, Volcanoes and Tectonics (COMET). We thank the University of Iceland for help with, and provision of the Eyjafjallajökull ash. We also gratefully acknowledge the contributions of the aviators and support engineers at AIRBUS and easyJet. We acknowledge the use of data products or imagery from the Land, Atmosphere Near real-time Capability for EOS (LANCE) system operated by the NASA/GSFC/Earth Science Data and Information System (ESDIS) with funding provided by NASA/HQ.

Author Contributions

A.J.P. developed AVOID and designed the airborne ash trial. A.J.P. also devised the ash detection algorithm and performed the radiative transfer calculations. F.D. led the AIRBUS project team and together with I.D., M.B. and M.W. provided the logistics for conducting the airborne experiment. K.W. and A.V. conducted and analysed the OPC measurements, and coordinated the DA42 flights. The electronics, software and hardware for AVOID were developed by C.B. and A.J.P. A.J.P., D.M. and H.E.T. processed the AVOID data. Avionics data analysis was conducted by D.M. and M.W. The ash sample was collected by I.D. and analysed by G.S.P. and T.A.M. J.C. and M.B. designed the mechanism for dispersing the ash from the A400 M. The lead author and all co-authors participated in the the experimental trials, except for T.M.

Additional Information

Supplementary information accompanies this paper at http://www.nature.com/srep

Competing financial interests: The authors declare no competing financial interests.

How to cite this article: Prata, A. J. *et al.* Artificial cloud test confirms volcanic ash detection using infrared spectral imaging. *Sci. Rep.* **6**, 25620; doi: 10.1038/srep25620 (2016).

Appendix B

Calculation of NBO/T

The calculation of NBO/T for the samples described in Chapter 3 is presented here in table format over a number of steps.

1. Proportions of FeO and Fe_2O_3 were calculated as per Middlemost (1975) by assigning rock types according to their positioning on the TAS diagram (Figure 3.1) in Chapter 3.

2. The analyses were re-normalised to 100% by excluding loss on ignition (LOI).

3. Molecular proportions were calculated using the molecular masses of each oxide listed in Table B.1.

4. Atomic proportions were calculated by multiplying by the number of cations present in each oxide.

5. The ratio of non-bridging oxygens (NBO) to tetrahedrally coordinated cations (T) was calculated using Equation 3.1 following Mysen et al. (1982).

The calculation spreadsheet can be accessed via the digital version of this thesis.

Table B.1: Molecular Masses used in Calculation

Element oxide	Molecular mass
SiO_2	60.084
TiO_2	79.865
Al_2O_3	101.961
Fe_2O_3	159.687
FeO	71.844
MnO	70.937
MgO	40.304
CaO	56.077
Na_2O	61.979
K_2O	94.195
P_2O_5	141.943
SO_3	80.062

Table B.2: Major Element Oxides for Bulk Analyses

Sample name	Askja	Aso	Augustine	Chaitén	Etna	Eyjafjallajökull (a)	Eyjafjallajökull (b)	Grímsvötn (a)	Grímsvötn (b)	Nisyros	Okmok	Spurr	Tongariro
SiO_2	72.35	54.96	62.86	74.90	48.04	60.00	58.85	50.58	50.33	74.16	53.23	55.99	64.13
TiO_2	0.86	0.85	0.62	0.16	1.79	1.31	1.46	2.81	2.91	0.33	1.22	0.73	0.70
Al_2O_3	12.58	18.30	16.58	14.15	17.80	14.68	14.96	13.59	13.58	14.01	16.75	18.96	17.72
Fe_2O_3	1.24	1.69	1.22	0.46	2.22	2.17	2.25	2.05	2.09	0.70	2.09	1.54	1.70
FeO	2.49	5.63	3.48	0.91	7.39	5.44	5.63	10.26	10.45	1.39	6.97	5.15	4.24
MnO	0.113	0.126	0.111	0.063	0.175	0.216	0.209	0.212	0.218	0.096	0.186	0.153	0.070
MgO	0.86	3.48	3.10	0.35	5.28	2.93	3.32	5.57	5.32	1.02	5.15	4.45	2.14
CaO	2.62	8.55	6.48	1.54	10.08	4.47	5.01	9.94	9.86	1.59	9.33	7.63	4.66
Na_2O	4.05	2.77	3.92	4.28	3.67	5.64	5.36	2.87	2.89	2.65	3.22	3.48	2.39
K_2O	2.373	1.699	1.103	3.025	2.087	2.283	2.059	0.488	0.479	3.803	0.880	0.962	1.359
P_2O_5	0.171	0.239	0.123	0.063	0.585	0.240	0.260	0.305	0.312	0.087	0.181	0.235	0.147
SO_3	0.003	1.083	0.003	0.003	0.058	0.006	0.003	0.163	0.387	0.016	0.004	0.157	0.266
LOI	1.02	2.88	0.16	1.33	-0.09	-0.08	-0.16	-0.93	-0.42	4.85	-0.13	0.51	5.96
Sum (ex. LOI)	99.72	99.37	99.61	99.90	99.18	99.39	99.37	98.86	98.84	99.85	99.22	99.43	99.53

Note: FeO and Fe_2O_3 calculated using f from Middlemost (1989)

Table B.3: Major Element Oxides for Glass Analyses

Sample name	Askja	Aso	Augustine	Chaitén	Etna	Eyjafjallajökull (a)	Eyjafjallajökull (b)	Grímsvötn (a)	Nisyros	Okmok	Spurr	Tongariro
SiO_2	73.69	55.90	66.20	73.70	50.92	66.43	64.25	51.30	72.20	55.19	50.21	58.18
TiO_2	0.77	0.96	0.24	0.11	2.02	0.93	1.18	2.80	0.23	1.68	0.10	0.16
Al_2O_3	12.79	19.23	19.94	15.50	16.64	14.14	14.81	13.37	16.34	14.10	29.53	25.55
Fe_2O_3	1.12	1.69	0.38	0.38	2.73	2.04	2.25	2.26	0.51	2.79	0.26	0.29
FeO	2.23	5.63	0.95	0.75	7.79	4.09	4.49	11.30	1.02	9.31	1.32	0.82
MnO	0.099	0.147	0.037	0.063	0.235	0.180	0.176	0.235	0.053	0.218	0.041	0.026
MgO	0.60	2.22	0.20	0.22	3.30	0.65	1.00	5.56	0.15	4.03	1.44	0.30
CaO	2.46	8.69	6.49	2.31	7.47	1.98	3.01	9.81	3.14	8.05	13.92	9.67
Na_2O	3.81	3.26	4.27	4.40	4.58	5.84	5.54	2.75	3.00	3.41	2.97	3.80
K_2O	2.406	2.182	1.259	2.562	3.817	3.696	3.199	0.483	3.390	1.213	0.107	1.150
P_2O_5	0.136	0.274	0.072	0.043	0.769	0.234	0.312	0.363	0.027	0.283	0.112	0.087
SO_3	0.000	0.000	0.000	0.000	0.000	0.000	0.000	0.000	0.000	0.000	0.000	0.000
LOI	0.00	0.00	0.00	0.00	0.00	0.00	0.00	0.00	0.00	0.00	0.00	0.00
Sum (ex. LOI)	100.11	100.17	100.04	100.04	100.27	100.20	100.23	100.23	100.05	100.28	100.03	100.03

Note: FeO and Fe_2O_3 calculated using f from Middlemost (1989)

Table B.4: Normalised Major Element Oxides for Bulk Analyses

Element oxide	Askja	Aso	Augustine	Chaitén	Etna	Eyjafjallajökull (a)	Eyjafjallajökull (b)	Grímsvötn (a)	Grímsvötn (b)	Nisyros	Okmok	Spurr	Tongariro
SiO_2	72.55	55.31	63.11	74.98	48.44	60.37	59.22	51.17	50.93	74.27	53.65	56.31	64.43
TiO_2	0.86	0.86	0.63	0.16	1.80	1.32	1.47	2.85	2.94	0.33	1.23	0.73	0.71
Al_2O_3	12.61	18.42	16.65	14.16	17.95	14.77	15.06	13.75	13.74	14.03	16.88	19.06	17.80
Fe_2O_3	1.25	1.70	1.22	0.46	2.24	2.19	2.27	2.08	2.11	0.70	2.11	1.55	1.70
FeO	2.50	5.67	3.49	0.91	7.46	5.47	5.66	10.38	10.57	1.39	7.03	5.18	4.26
MnO	0.113	0.127	0.111	0.063	0.176	0.217	0.210	0.215	0.221	0.096	0.188	0.154	0.070
MgO	0.87	3.50	3.12	0.35	5.33	2.95	3.34	5.64	5.39	1.02	5.19	4.47	2.15
CaO	2.63	8.61	6.51	1.54	10.17	4.50	5.05	10.06	9.98	1.59	9.40	7.67	4.69
Na_2O	4.06	2.78	3.93	4.28	3.70	5.67	5.40	2.90	2.92	2.65	3.25	3.50	2.40
K_2O	2.380	1.710	1.108	3.028	2.104	2.297	2.072	0.494	0.485	3.809	0.887	0.968	1.365
P_2O_5	0.171	0.240	0.123	0.063	0.590	0.242	0.261	0.309	0.316	0.087	0.182	0.237	0.147
SO_3	0.003	1.089	0.003	0.003	0.058	0.006	0.003	0.165	0.391	0.016	0.004	0.158	0.267
Sum	100	100	100	100	100	100	100	100	100	100	100	100	100

Table B.5: Normalised Major Element Oxides for Glass Analyses

Element oxide	Askja	Aso	Augustine	Chaitén	Etna	Eyjafjallajökull (a)	Eyjafjallajökull (b)	Grímsvötn (a)	Nisyros	Okmok	Spurr	Tongariro
SiO_2	73.60	55.81	66.17	73.67	50.78	66.29	64.11	51.19	72.16	55.03	50.20	58.16
TiO_2	0.77	0.95	0.24	0.11	2.01	0.92	1.18	2.79	0.23	1.67	0.10	0.16
Al_2O_3	12.78	19.20	19.93	15.49	16.60	14.11	14.78	13.34	16.33	14.06	29.52	25.54
Fe_2O_3	1.12	1.69	0.38	0.38	2.72	2.04	2.24	2.25	0.51	2.79	0.26	0.29
FeO	2.23	5.62	0.95	0.75	7.77	4.08	4.48	11.27	1.02	9.28	1.32	0.82
MnO	0.099	0.147	0.037	0.063	0.235	0.180	0.176	0.234	0.053	0.217	0.041	0.026
MgO	0.60	2.21	0.20	0.22	3.29	0.65	1.00	5.55	0.15	4.02	1.44	0.30
CaO	2.46	8.67	6.49	2.31	7.45	1.97	3.00	9.79	3.13	8.03	13.92	9.67
Na_2O	3.81	3.25	4.27	4.40	4.57	5.83	5.53	2.75	3.00	3.40	2.97	3.80
K_2O	2.403	2.179	1.259	2.561	3.806	3.689	3.192	0.482	3.388	1.210	0.107	1.149
P_2O_5	0.136	0.274	0.072	0.043	0.766	0.233	0.311	0.362	0.027	0.282	0.112	0.087
SO_3	0.000	0.000	0.000	0.000	0.000	0.000	0.000	0.000	0.000	0.000	0.000	0.000
Sum	100	100	100	100	100	100	100	100	100	100	100	100

Table B.6: Molecular Proportions of Major Element Oxides for Bulk Analyses

Molecular proportion	Askja	Aso	Augustine	Chaitén	Etna	Eyjafjallajökull (a)	Eyjafjallajökull (b)	Grímsvötn (a)	Grímsvötn (b)	Nisyros	Okmok	Spurr	Tongariro
SiO_2	1.21	0.92	1.05	1.25	0.81	1.00	0.99	0.85	0.85	1.24	0.89	0.94	1.07
TiO_2	0.01	0.01	0.01	0.00	0.02	0.02	0.02	0.04	0.04	0.00	0.02	0.01	0.01
Al_2O_3	0.12	0.18	0.16	0.14	0.18	0.14	0.15	0.13	0.13	0.14	0.17	0.19	0.17
Fe_2O_3	0.01	0.01	0.01	0.00	0.01	0.01	0.01	0.01	0.01	0.00	0.01	0.01	0.01
FeO	0.03	0.08	0.05	0.01	0.10	0.08	0.08	0.14	0.15	0.02	0.10	0.07	0.06
MnO	0.002	0.002	0.002	0.001	0.002	0.003	0.003	0.003	0.003	0.001	0.003	0.002	0.001
MgO	0.02	0.09	0.08	0.01	0.13	0.07	0.08	0.14	0.13	0.03	0.13	0.11	0.05
CaO	0.05	0.15	0.12	0.03	0.18	0.08	0.09	0.18	0.18	0.03	0.17	0.14	0.08
Na_2O	0.07	0.04	0.06	0.07	0.06	0.09	0.09	0.05	0.05	0.04	0.05	0.06	0.04
K_2O	0.025	0.018	0.012	0.032	0.022	0.024	0.022	0.005	0.005	0.040	0.009	0.010	0.014
P_2O_5	0.001	0.002	0.001	0.000	0.004	0.002	0.002	0.002	0.002	0.001	0.001	0.002	0.001
SO_3	0.000	0.014	0.000	0.000	0.001	0.000	0.000	0.002	0.005	0.000	0.000	0.002	0.003
Total	1.55	1.52	1.55	1.54	1.53	1.53	1.53	1.56	1.55	1.54	1.55	1.54	1.52

Table B.7: Molecular Proportions of Major Element Oxides for Glass Analyses

Molecular proportion	Askja	Aso	Augustine	Chaitén	Etna	Eyjafjallajökull (a)	Eyjafjallajökull (b)	Grímsvötn (a)	Nisyros	Okmok	Spurr	Tongariro
SiO_2	1.23	0.93	1.10	1.23	0.85	1.10	1.07	0.85	1.20	0.92	0.84	0.97
TiO_2	0.01	0.01	0.00	0.00	0.03	0.01	0.01	0.03	0.00	0.02	0.00	0.00
Al_2O_3	0.13	0.19	0.20	0.15	0.16	0.14	0.14	0.13	0.16	0.14	0.29	0.25
Fe_2O_3	0.01	0.01	0.00	0.00	0.02	0.01	0.01	0.01	0.00	0.02	0.00	0.00
FeO	0.03	0.08	0.01	0.01	0.11	0.06	0.06	0.16	0.01	0.13	0.02	0.01
MnO	0.001	0.002	0.001	0.001	0.003	0.003	0.002	0.003	0.001	0.003	0.001	0.000
MgO	0.01	0.05	0.01	0.01	0.08	0.02	0.02	0.14	0.00	0.10	0.04	0.01
CaO	0.04	0.15	0.12	0.04	0.13	0.04	0.05	0.17	0.06	0.14	0.25	0.17
Na_2O	0.06	0.05	0.07	0.07	0.07	0.09	0.09	0.04	0.05	0.05	0.05	0.06
K_2O	0.026	0.023	0.013	0.027	0.040	0.039	0.034	0.005	0.036	0.013	0.001	0.012
P_2O_5	0.001	0.002	0.001	0.000	0.005	0.002	0.002	0.003	0.000	0.002	0.001	0.001
SO_3	0.000	0.000	0.000	0.000	0.000	0.000	0.000	0.000	0.000	0.000	0.000	0.000
Total	1.55	1.51	1.52	1.54	1.50	1.51	1.51	1.56	1.53	1.54	1.48	1.49

Table B.8: Atomic Proportions of Major Elements for Bulk Analyses

Atomic proportion	Askja	Aso	Augustine	Chaitén	Etna	Eyjafjallajökull (a)	Eyjafjallajökull (b)	Grímsvötn (a)	Grímsvötn (b)	Nisyros	Okmok	Spurr	Tongariro
Si	1.21	0.92	1.05	1.25	0.81	1.00	0.99	0.85	0.85	1.24	0.89	0.94	1.07
Ti	0.01	0.01	0.01	0.00	0.02	0.02	0.02	0.04	0.04	0.00	0.02	0.01	0.01
Al	0.25	0.36	0.33	0.28	0.35	0.29	0.30	0.27	0.27	0.28	0.33	0.37	0.35
Fe^{3+}	0.02	0.02	0.02	0.01	0.03	0.03	0.03	0.03	0.03	0.01	0.03	0.02	0.02
Fe^{2+}	0.03	0.08	0.05	0.01	0.10	0.08	0.08	0.14	0.15	0.02	0.10	0.07	0.06
Mn	0.002	0.002	0.002	0.001	0.002	0.003	0.003	0.003	0.003	0.001	0.003	0.002	0.001
Mg	0.02	0.09	0.08	0.01	0.13	0.07	0.08	0.14	0.13	0.03	0.13	0.11	0.05
Ca	0.05	0.15	0.12	0.03	0.18	0.08	0.09	0.18	0.18	0.03	0.17	0.14	0.08
Na	0.13	0.09	0.13	0.14	0.12	0.18	0.17	0.09	0.09	0.09	0.10	0.11	0.08
K	0.051	0.036	0.024	0.064	0.045	0.049	0.044	0.010	0.010	0.081	0.019	0.021	0.029
P	0.002	0.003	0.002	0.001	0.008	0.003	0.004	0.004	0.004	0.001	0.003	0.003	0.002
S	0.000	0.014	0.000	0.000	0.001	0.000	0.000	0.002	0.005	0.000	0.000	0.002	0.003
O	3.03	2.87	2.95	3.08	2.75	2.88	2.87	2.75	2.75	3.07	2.82	2.89	2.98

Table B.9: Atomic Proportions of Major Elements for Glass Analyses

Element proportion	Askja	Aso	Augustine	Chaitén	Etna	Eyjafjallajökull (a)	Eyjafjallajökull (b)	Grímsvötn (a)	Nisyros	Okmok	Spurr	Tongariro
Si	1.23	0.93	1.10	1.23	0.85	1.10	1.07	0.85	1.20	0.92	0.84	0.97
Ti	0.01	0.01	0.00	0.00	0.03	0.01	0.01	0.03	0.00	0.02	0.00	0.00
Al	0.25	0.38	0.39	0.30	0.33	0.28	0.29	0.26	0.32	0.28	0.58	0.50
Fe^{3+}	0.01	0.02	0.00	0.00	0.03	0.03	0.03	0.03	0.01	0.03	0.00	0.00
Fe^{2+}	0.03	0.08	0.01	0.01	0.11	0.06	0.06	0.16	0.01	0.13	0.02	0.01
Mn	0.001	0.002	0.001	0.001	0.003	0.003	0.002	0.003	0.001	0.003	0.001	0.000
Mg	0.01	0.05	0.01	0.01	0.08	0.02	0.02	0.14	0.00	0.10	0.04	0.01
Ca	0.04	0.15	0.12	0.04	0.13	0.04	0.05	0.17	0.06	0.14	0.25	0.17
Na	0.12	0.10	0.14	0.14	0.15	0.19	0.18	0.09	0.10	0.11	0.10	0.12
K	0.051	0.046	0.027	0.054	0.081	0.078	0.068	0.010	0.072	0.026	0.002	0.024
P	0.002	0.004	0.001	0.001	0.011	0.003	0.004	0.005	0.000	0.004	0.002	0.001
S	0.000	0.000	0.000	0.000	0.000	0.000	0.000	0.000	0.000	0.000	0.000	0.000
O	3.05	2.85	3.02	3.08	2.75	2.94	2.92	2.74	3.06	2.79	2.90	2.97

Table B.10: NBO/T Calculation for Bulk Analyses

Calculation	Askja	Aso	Augustine	Chaitén	Etna	Eyjafjallajökull (a)	Eyjafjallajökull (b)	Grímsvötn (a)	Grímsvötn (b)	Nisyros	Okmok	Spurr	Tongariro
Si + Ti + P	1.22	0.93	1.06	1.25	0.84	1.02	1.01	0.89	0.89	1.24	0.91	0.95	1.08
Na + K + 2Ca + 2Mg	0.32	0.61	0.54	0.27	0.79	0.54	0.56	0.74	0.73	0.27	0.72	0.63	0.38
Al^{3+} in tetrahedral?	0.25	0.36	0.33	0.27	0.35	0.29	0.30	0.27	0.27	0.27	0.33	0.37	0.35
(Na+K)-Al	-0.07	-0.24	-0.18	-0.08	-0.19	-0.06	-0.08	-0.17	-0.16	-0.11	-0.21	-0.24	-0.24
Excess available for charge-balance?	0.00	0.00	0.00	0.00	0.00	0.00	0.00	0.00	0.00	0.00	0.00	0.00	0.00
Fe^{3+} in tetrahedral?	0.00	0.00	0.00	0.00	0.00	0.00	0.00	0.00	0.00	0.00	0.00	0.00	0.00
Total T	1.47	1.30	1.39	1.53	1.19	1.31	1.30	1.16	1.16	1.52	1.24	1.32	1.43
NBO	0.19	0.56	0.36	0.05	0.75	0.49	0.52	0.86	0.87	0.07	0.67	0.48	0.24
NBO/T	0.13	0.43	0.26	0.04	0.63	0.38	0.40	0.74	0.75	0.05	0.54	0.36	0.17

Table B.11: NBO/T Calculation for Glass Analyses

Calculation	Askja	Aso	Augustine	Chaitén	Etna	Eyjafjallajökull (a)	Eyjafjallajökull (b)	Grímsvötn (a)	Nisyros	Okmok	Spurr	Tongariro
Si + Ti + P	1.24	0.94	1.11	1.23	0.88	1.12	1.09	0.89	1.20	0.94	0.84	0.97
Na + K + 2Ca + 2Mg	0.29	0.57	0.41	0.29	0.66	0.37	0.40	0.72	0.29	0.62	0.67	0.51
Al^{3+} in tetrahedral?	0.25	0.38	0.39	0.29	0.33	0.28	0.29	0.26	0.29	0.28	0.58	0.50
(Na+K)-Al	-0.08	-0.23	-0.23	-0.11	-0.10	-0.01	-0.04	-0.16	-0.15	-0.14	-0.48	-0.35
Excess available for charge-balance?	0.00	0.00	0.00	0.00	0.00	0.00	0.00	0.00	0.00	0.00	0.00	0.00
Fe^{3+} in tetrahedral?	0.00	0.00	0.00	0.00	0.00	0.00	0.00	0.00	0.00	0.00	0.00	0.00
Total T	1.49	1.32	1.50	1.52	1.21	1.39	1.38	1.15	1.49	1.22	1.42	1.47
NBO	0.15	0.42	0.06	0.08	0.67	0.29	0.33	0.87	0.15	0.72	0.14	0.04
NBO/T	0.10	0.32	0.04	0.05	0.55	0.21	0.24	0.76	0.10	0.59	0.10	0.03

Appendix C

Parameterisation

The parameterisation developed in this thesis calculates the real (n) and imaginary (k) parts of the refractive index over 1,933 discrete wavelengths. A spreadsheet has been created in order to allow the user to input a volcanic ash composition in terms of NBO/T or wt.%SiO_2. This is illustrated in Figure C.1.

The parameterisation spreadsheet can be accessed via the digital version of this thesis.

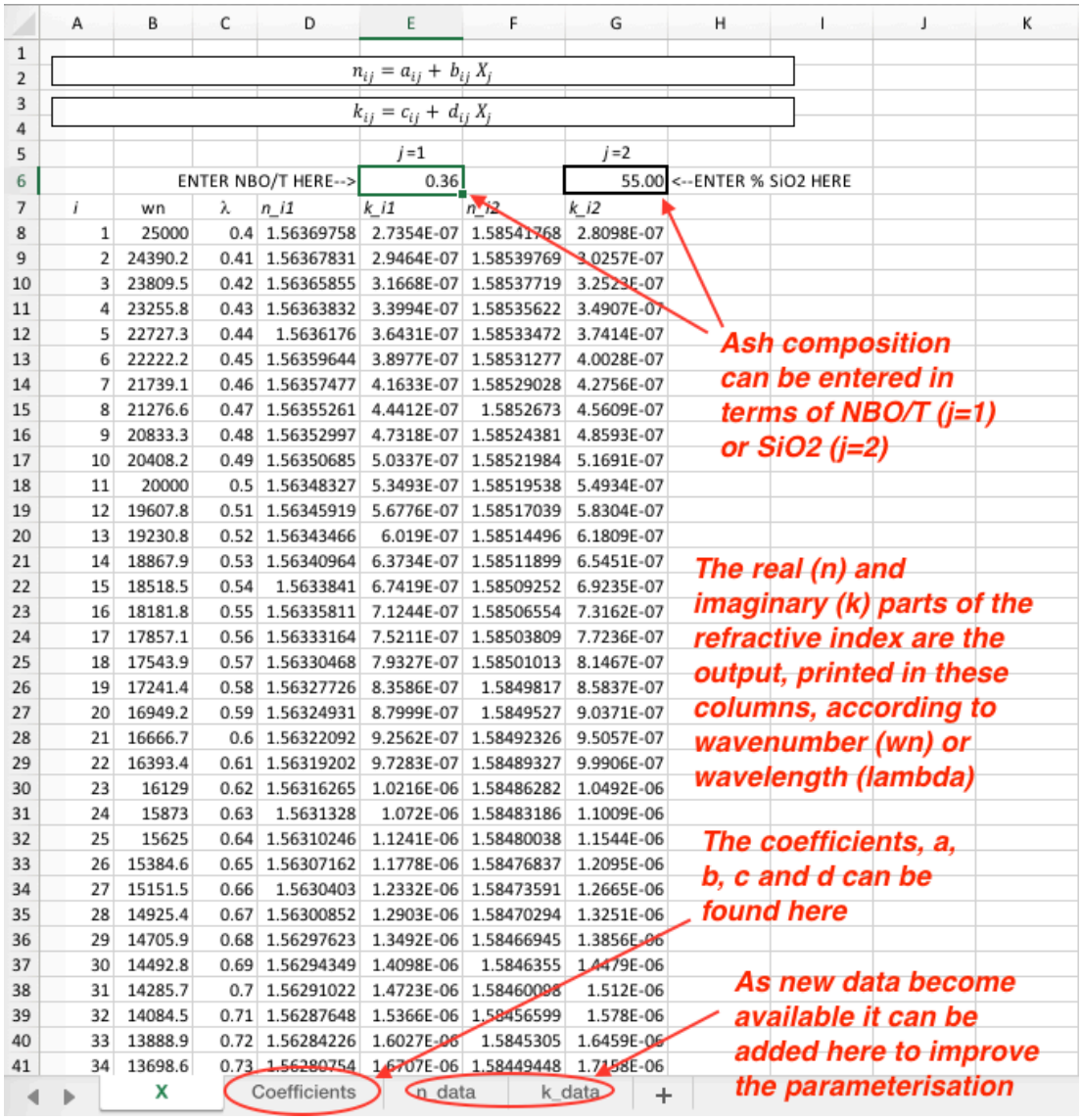

Figure C.1: Screenshot of the parameterisation spreadsheet

Appendix D

HYSPLIT Back Trajectories

This appendix contains back-trajectory plots for the samples in **bold** presented in Chapter 4, Table 4.1. The back-trajectories were calculated using the HYbrid Single-Particle Lagrangian Integrated Trajectory (HYSPLIT) transport and dispersion model (Stein et al., 2015) on the READY website (http://www.ready.noaa.gov), provided by the NOAA Air Resources Laboratory (ARL).

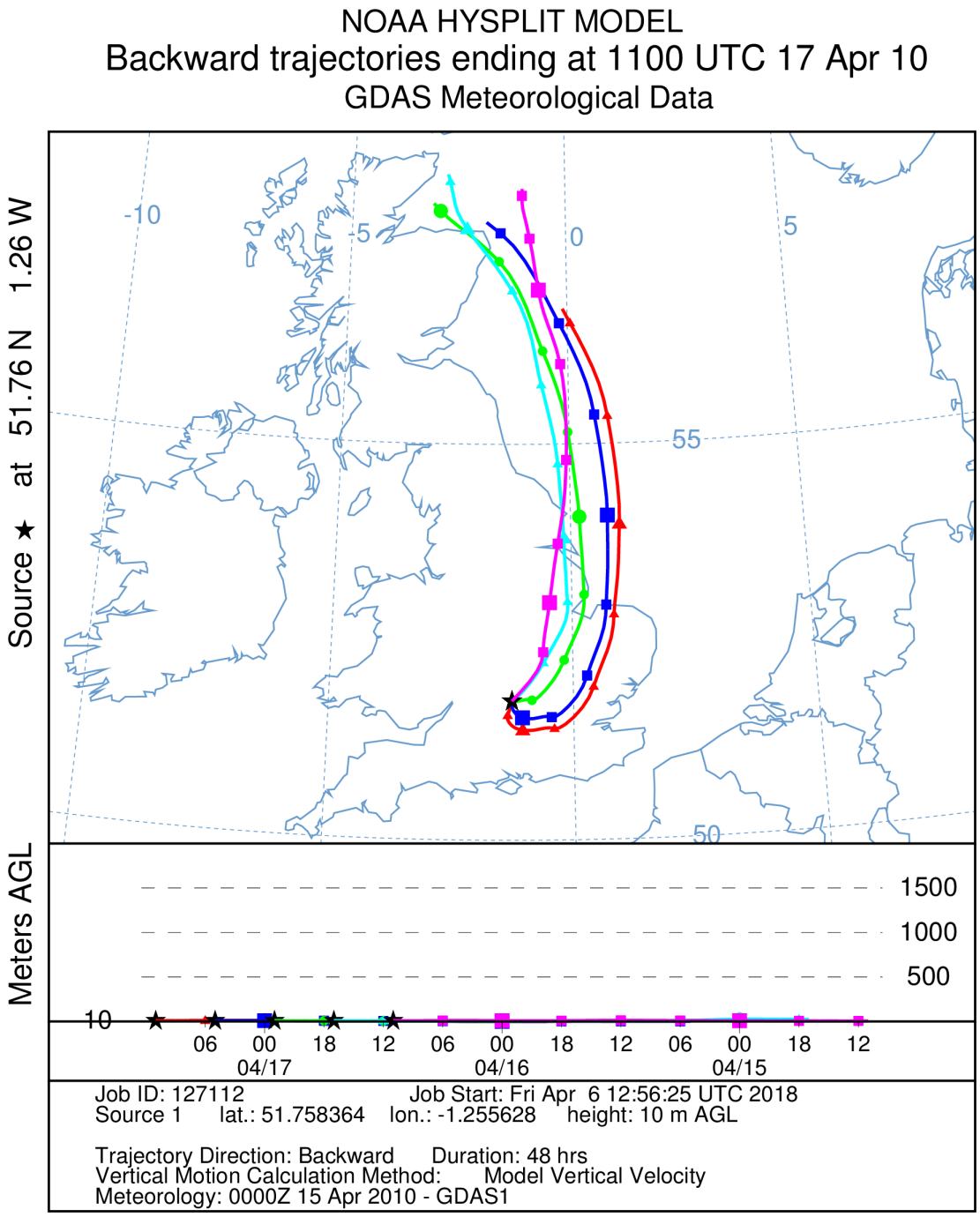

Figure D.1: HYSPLIT back trajectory for OxAsh 1, to cover the sample collection period of 20.6 h from the start time 15:00 UTC 16/04/2010.

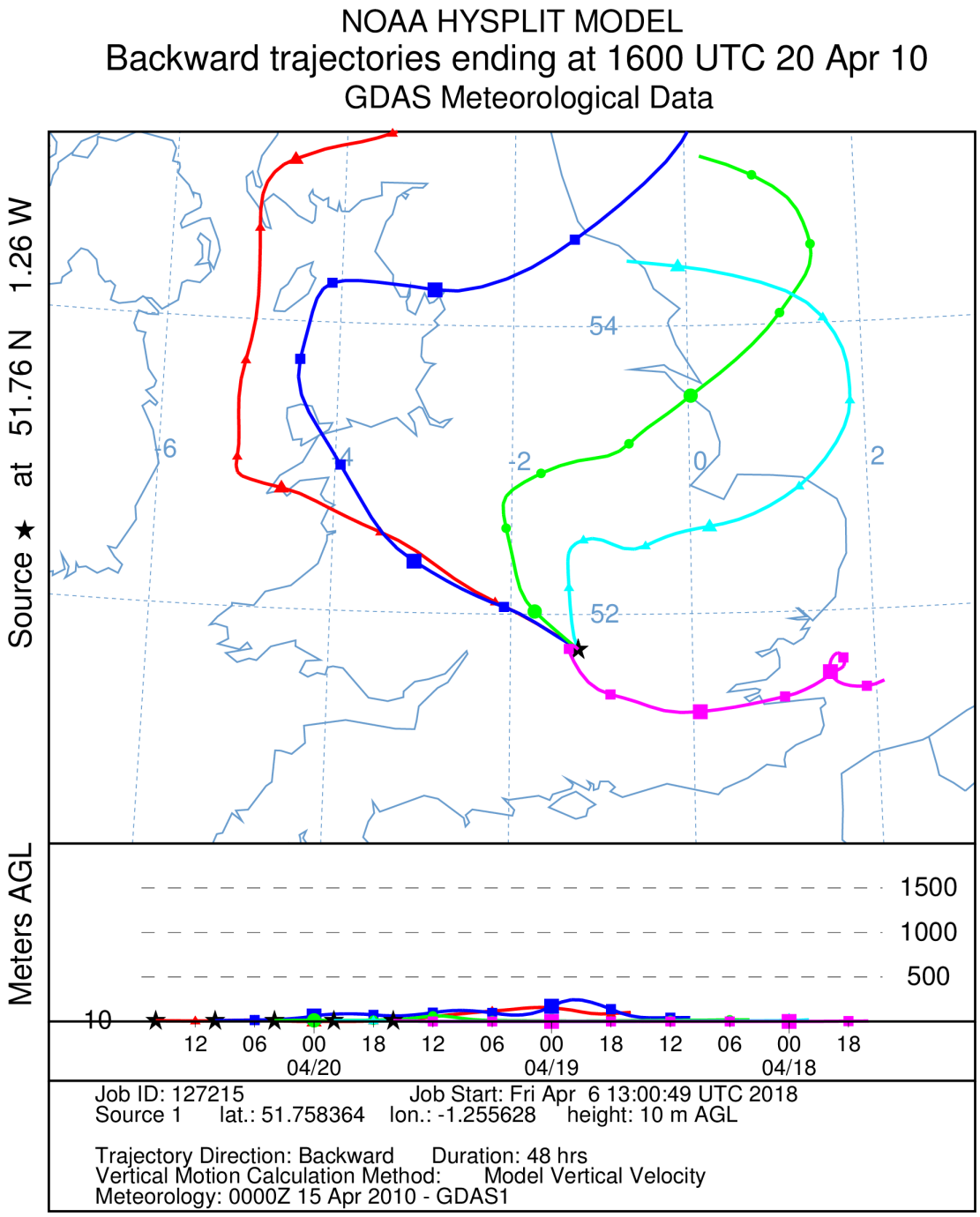

Figure D.2: HYSPLIT back trajectory for OxAsh 4, to cover the sample collection period of 24.8 h from the start time 15:25 UTC 19/04/2010.

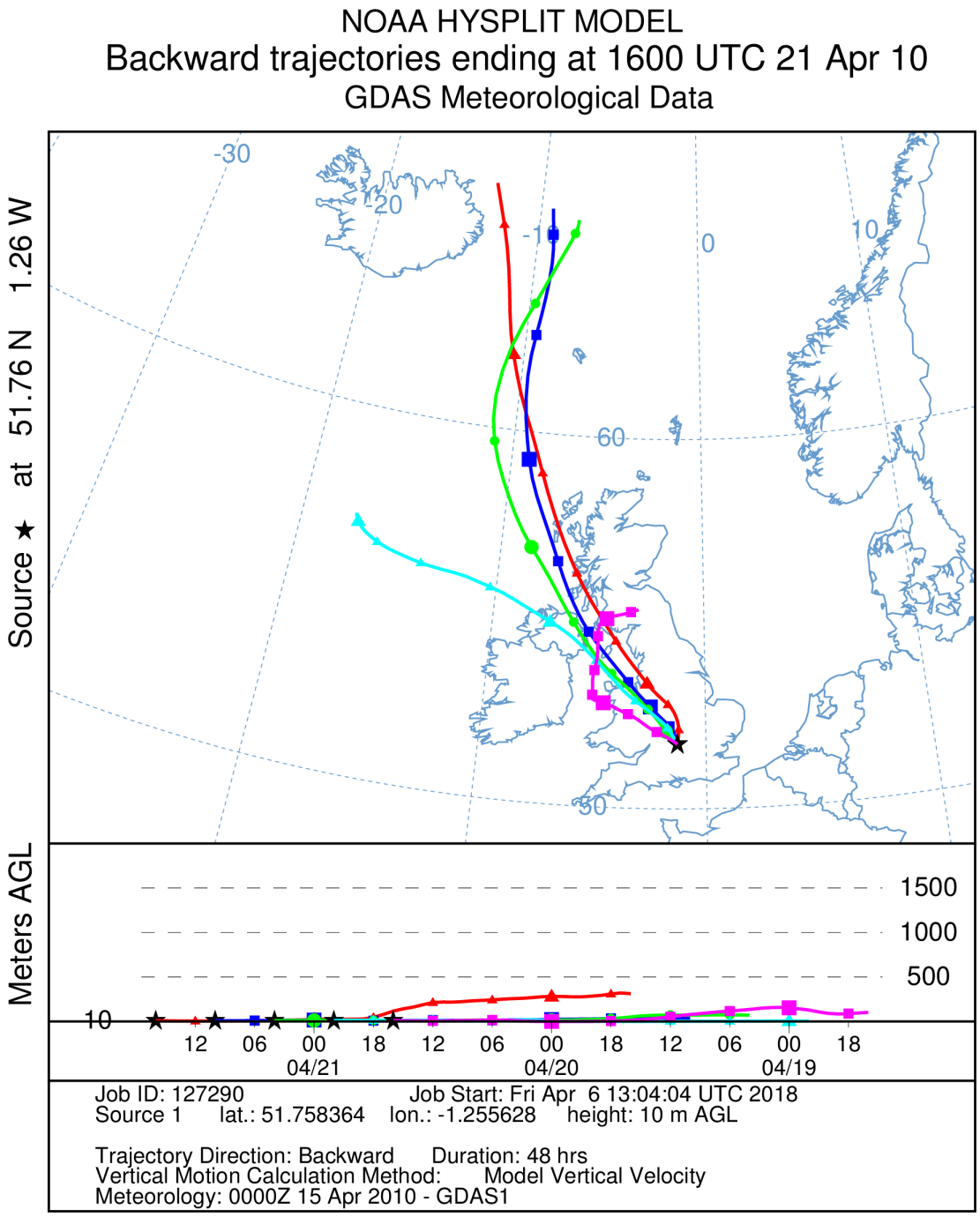

Figure D.3: HYSPLIT back trajectory for OxAsh 5, to cover the sample collection period of 23.8 h from the start time 16:40 UTC 20/04/2010.

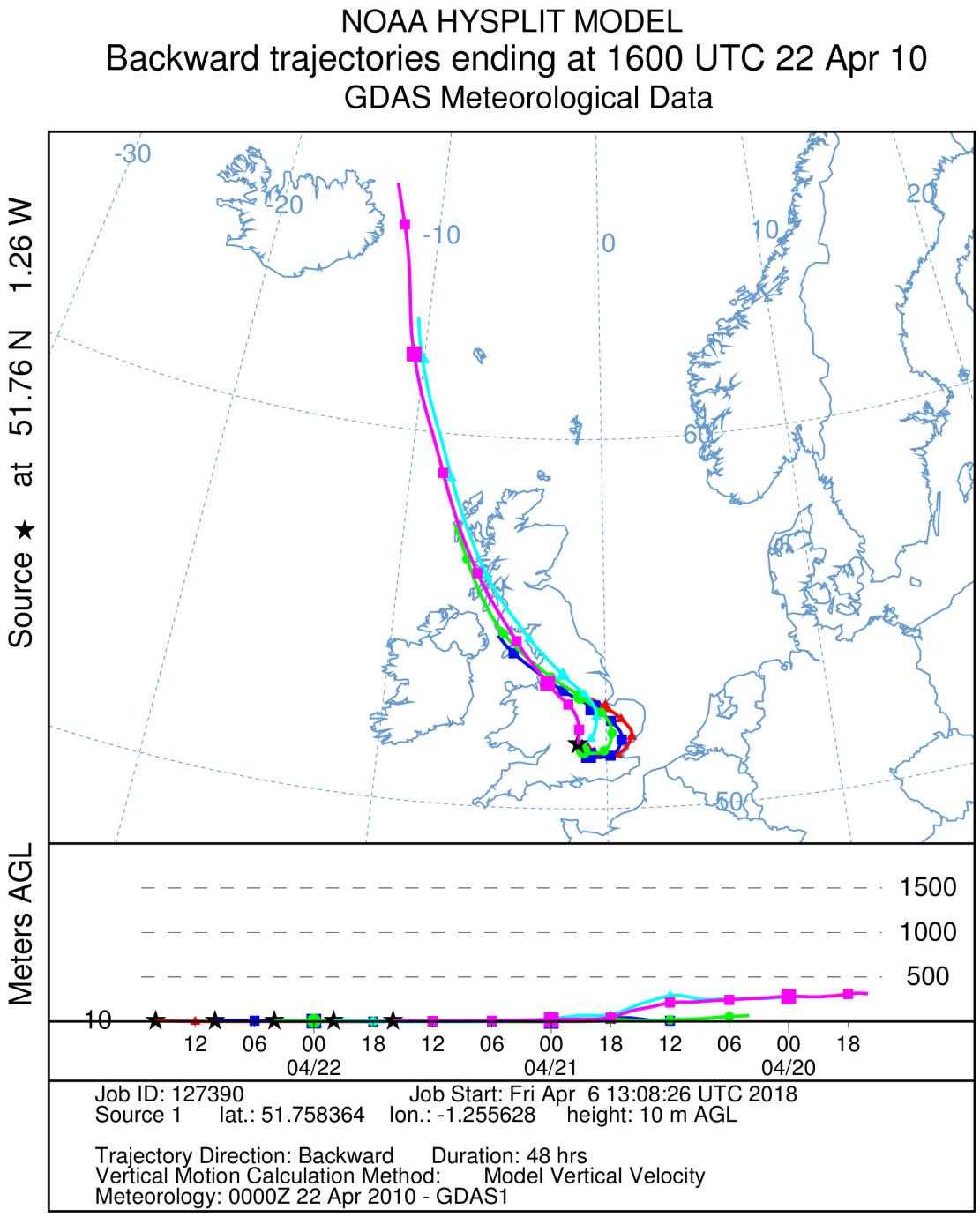

Figure D.4: HYSPLIT back trajectory for OxAsh 6, to cover the sample collection period of 23.5 h from the start time 17:00 UTC 21/04/2010.

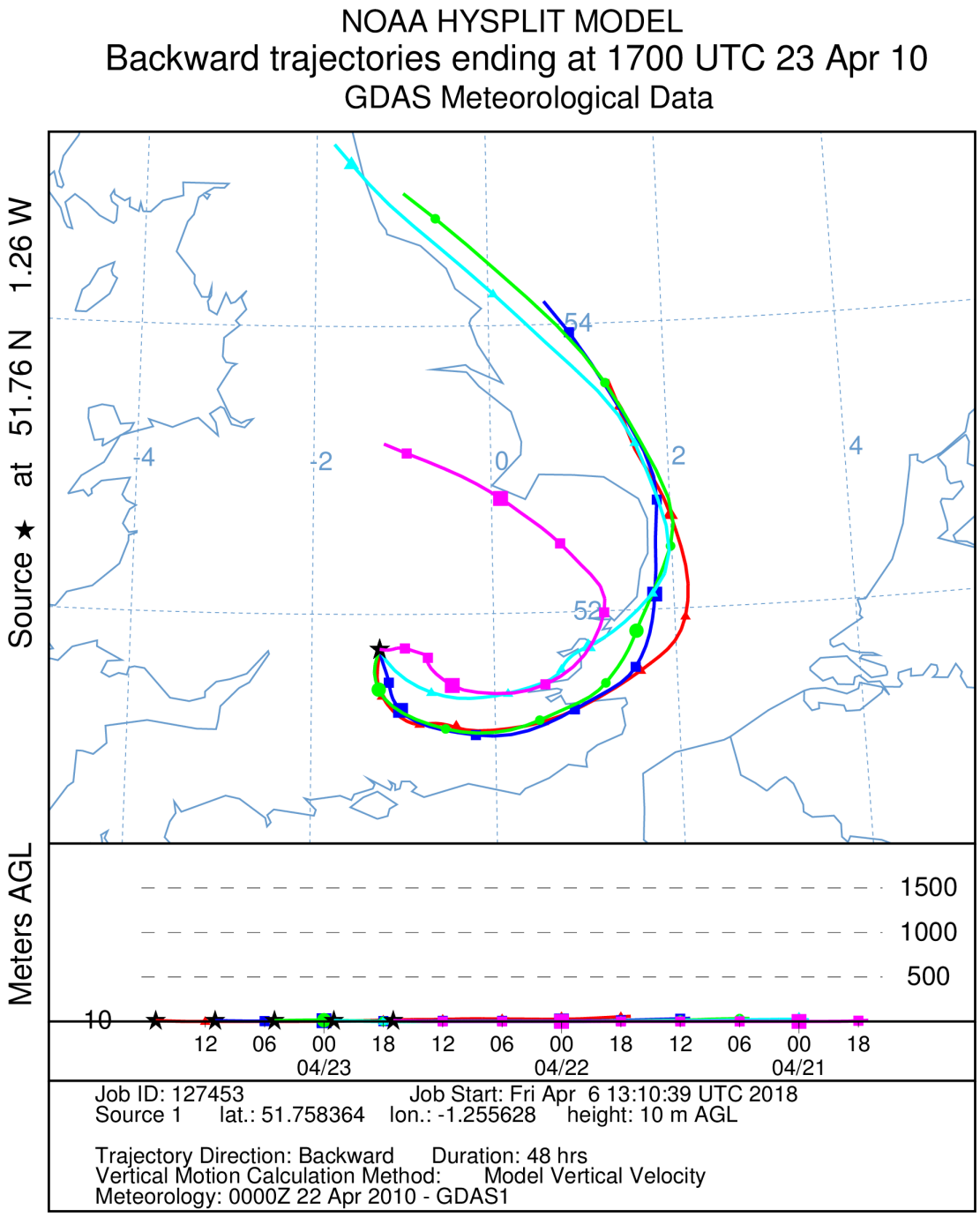

Figure D.5: HYSPLIT back trajectory for OxAsh 7, to cover the sample collection period of 23.8 h from the start time 17:00 UTC 22/04/2010.

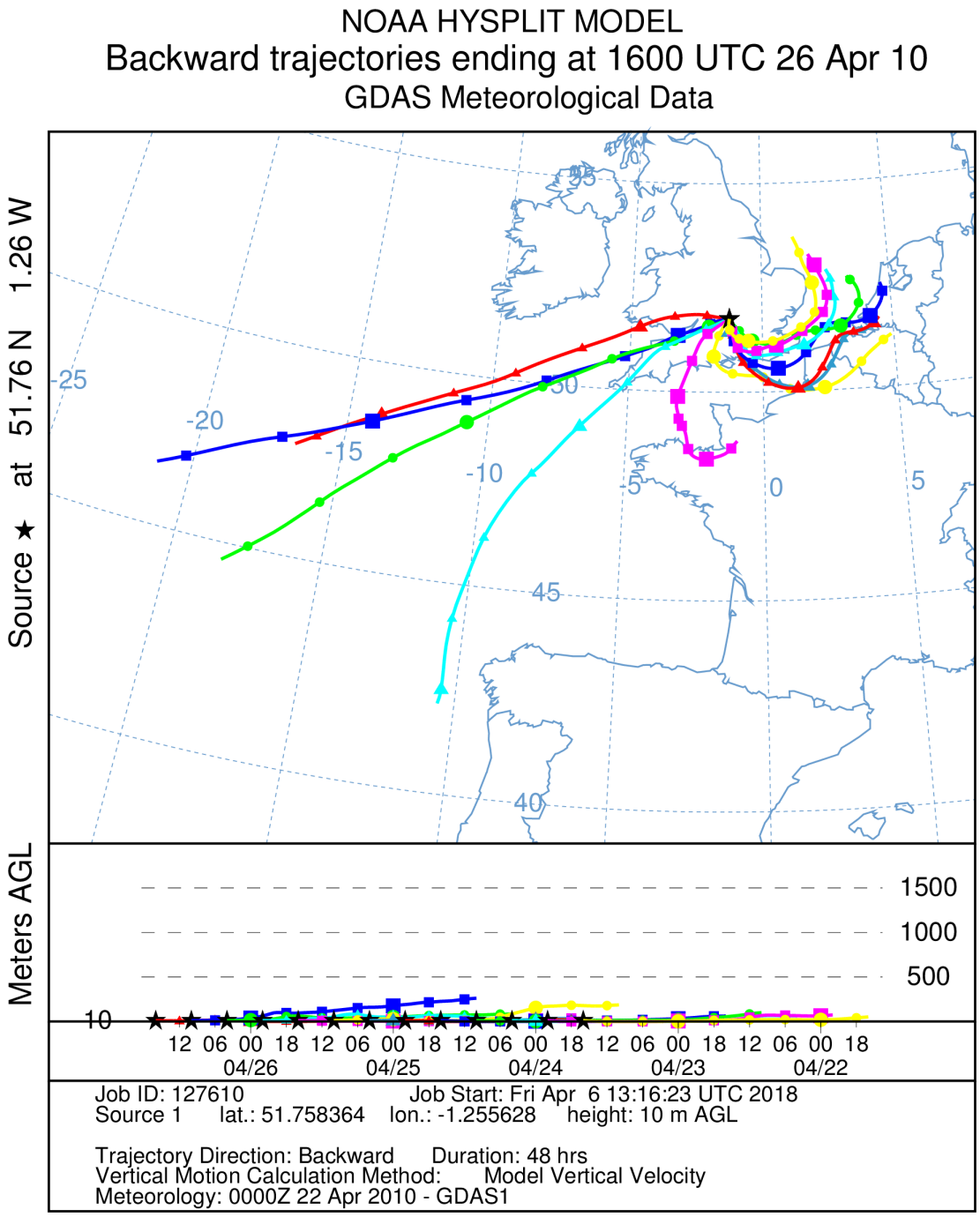

Figure D.6: HYSPLIT back trajectory for OxAsh 8, to cover the sample collection period of 70.2 h from the start time 17:23 UTC 23/04/2010.

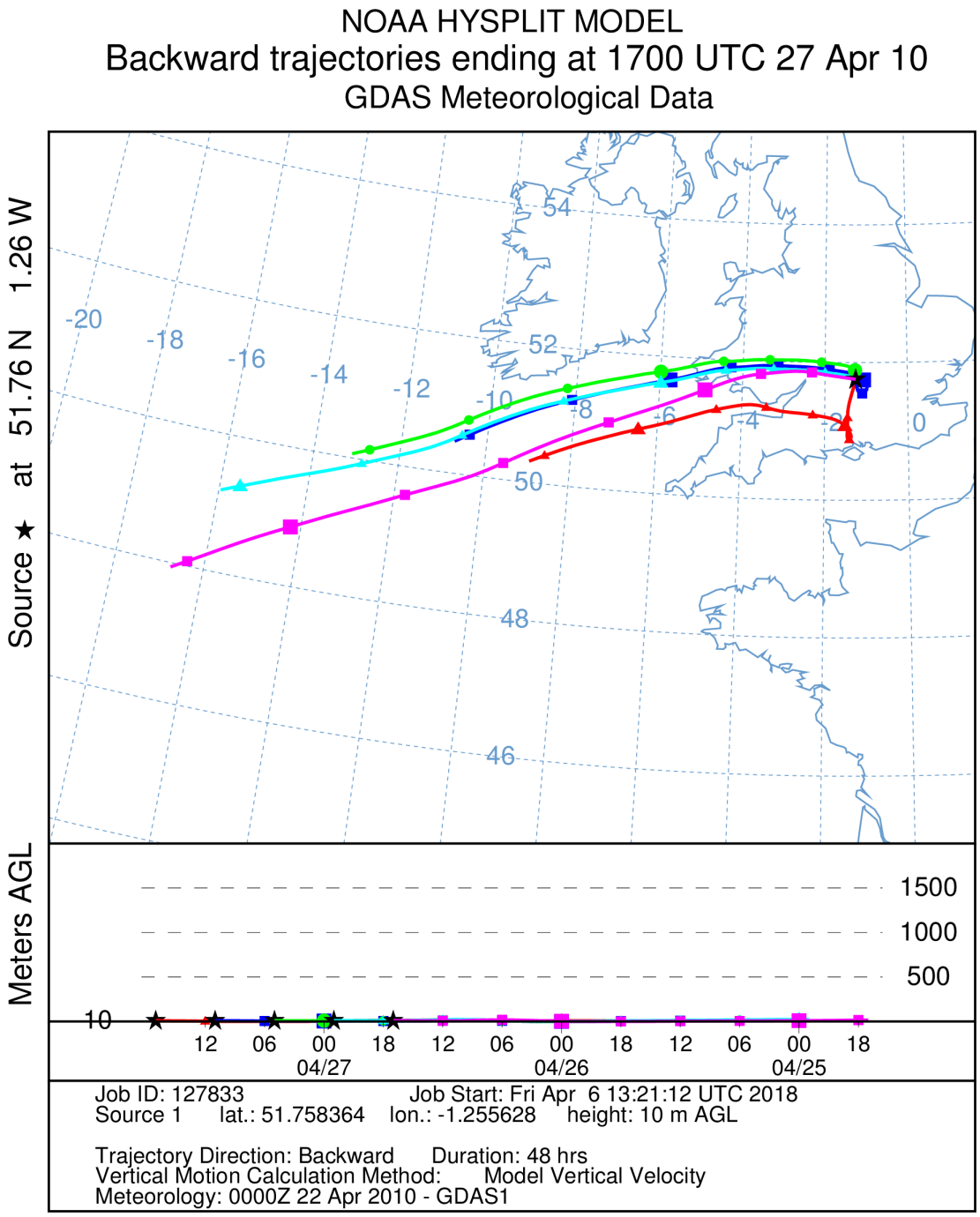

Figure D.7: HYSPLIT back trajectory for OxAsh 9, to cover the sample collection period of 24.8 h from the start time 16:05 UTC 26/04/2010.

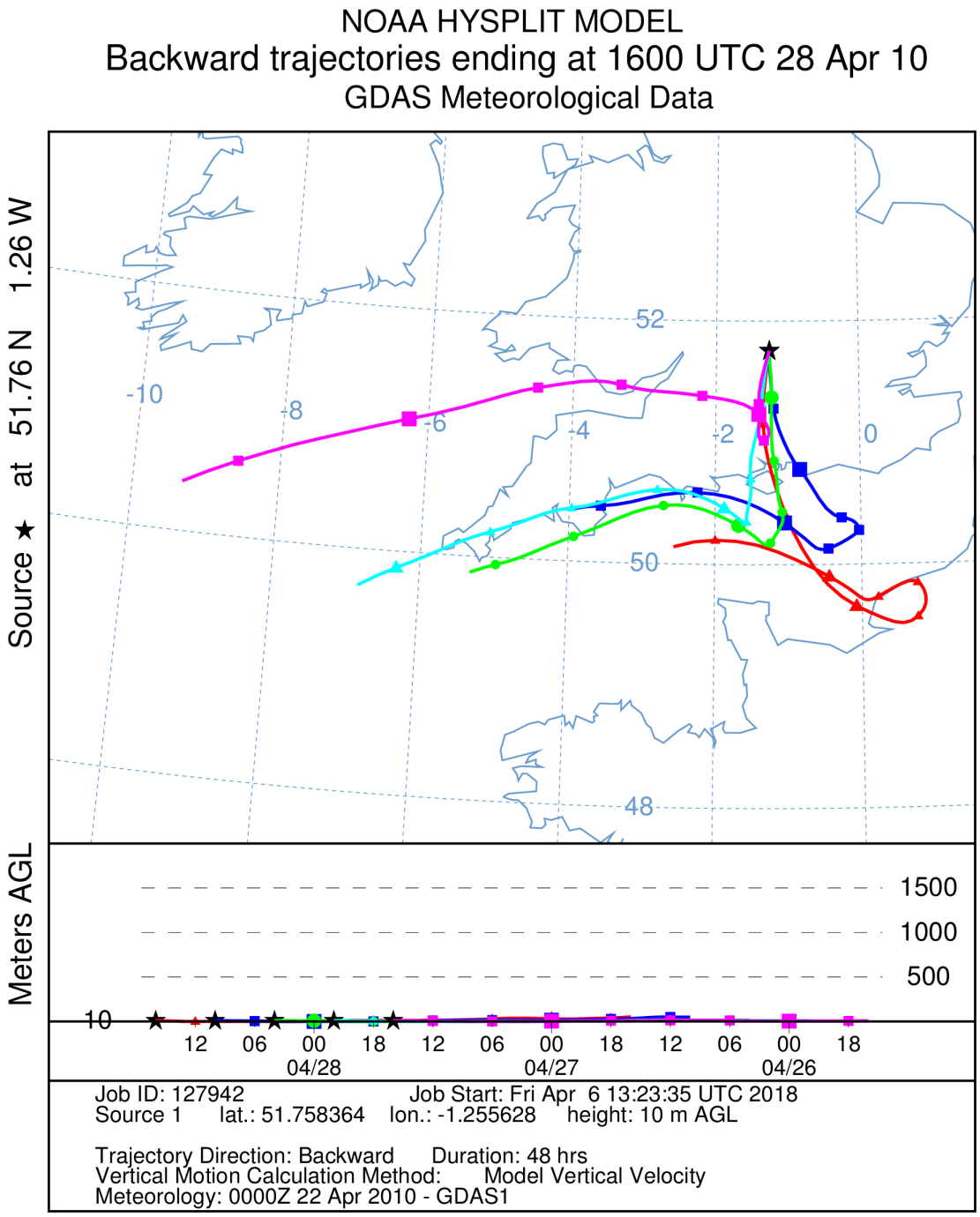

Figure D.8: HYSPLIT back trajectory for OxAsh 10, to cover the sample collection period of 22.7 h from the start time 17:20 UTC 27/04/2010.

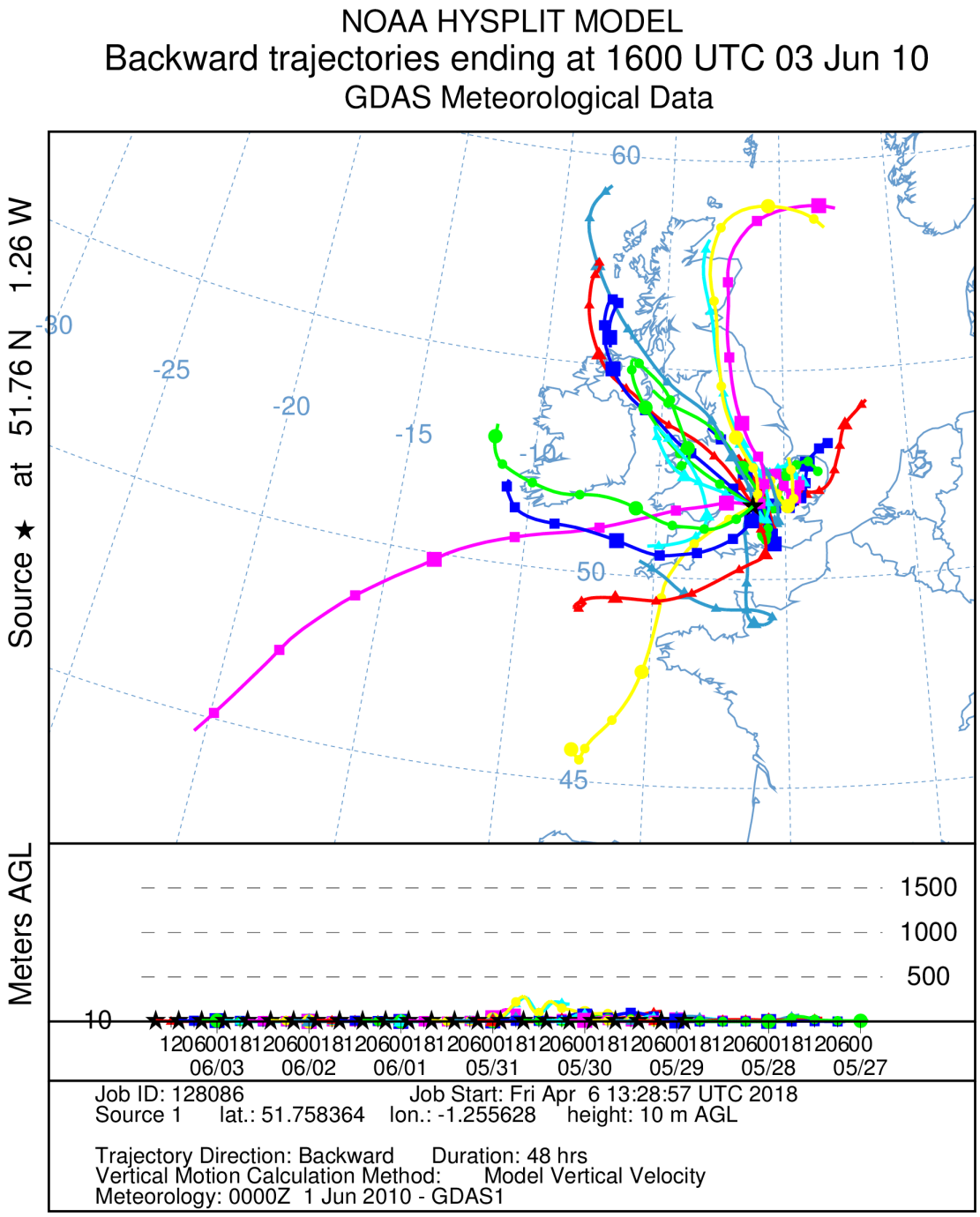

Figure D.9: HYSPLIT back trajectory for OxAsh 20, to cover the sample collection period of 141.9 h from the start time 17:48 UTC 28/05/2010.

Appendix E

Composition time series plots

This appendix contains time series plots for the trace metal concentration ratios to background of samples in **bold** presented in Chapter 4, Table 4.1.

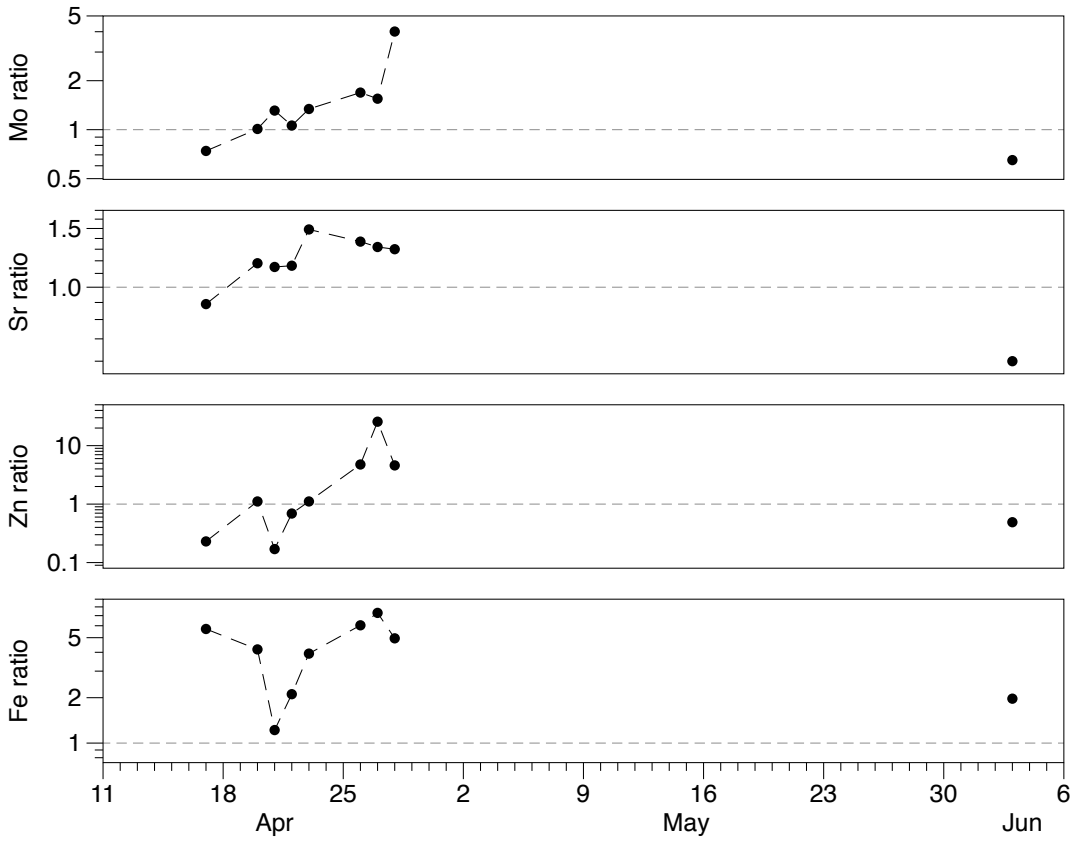

Figure E.1: Time series of the concentration ratios to background of Fe, Zn, Sr and Mo.

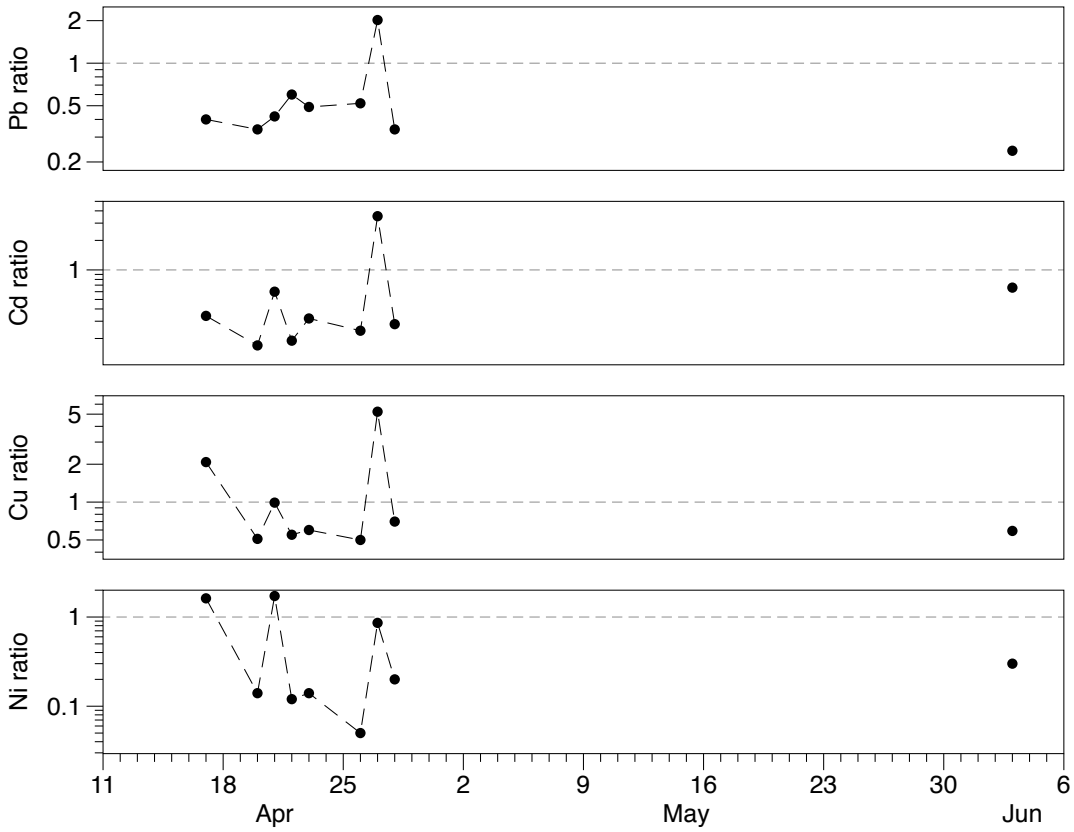

Figure E.2: Time series of the concentration ratios to background of Ni, Cu, Cd and Pb.

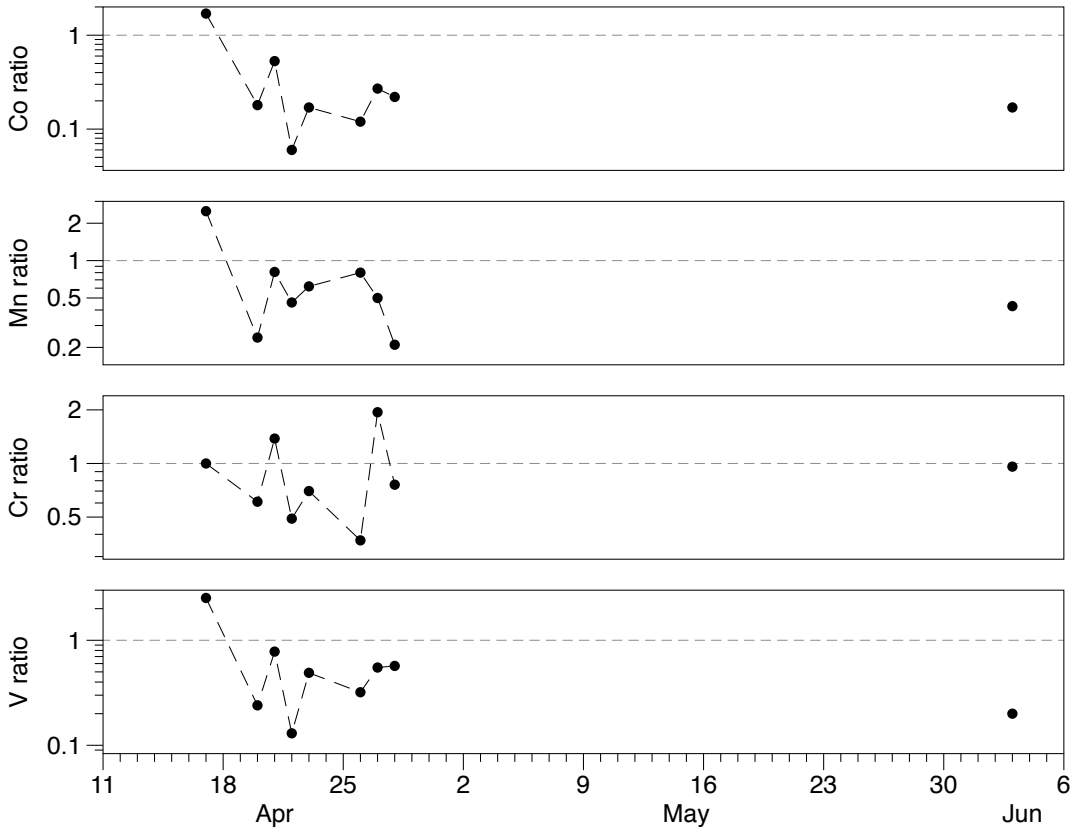

Figure E.3: Time series of the concentration ratios to background of V, Cr, Mn and Co.

References

Achterberg, E. P., Mark Moore, C., Henson, S. A., Steigenberger, S., Stohl, A., Eckhardt, S., Avendano, L. C., Cassidy, M., Hembury, D., Klar, J. K., Lucas, M. I., Macey, A. I., Marsay, C. M., and Ryan-Keogh, T. J. (2013). Natural iron fertilisation by the Eyjafjallajökull volcanic eruption. ***Geophysical Research Letters***, 40:921–926.

Andersson, S. M., Martinsson, B. G., Friberg, J., Brenninkmeijer, C. A. M., Rauthe-Schöch, A., Hermann, M., Van Velthoven, P. F. J., and Zahn, A. (2013). Geoscientific Instrumentation Methods and Data Systems Composition and evolution of volcanic aerosol from eruptions of Kasatochi, Sarychev and Eyjafjallajökull in 2008–2010 based on CARIBIC observations. ***Atmos. Chem. Phys***, 13:1781–1796.

Ayris, P. and Delmelle, P. (2012). Volcanic and atmospheric controls on ash iron solubility: A review. ***Physics and Chemistry of the Earth, Parts A/B/C***, 45-46:103–112.

Bagnato, E., Aiuppa, A., Bertagnini, A., Bonadonna, C., Cioni, R., Pistolesi, M., Pedone, M., and Hoskuldsson, A. (2013). Scavenging of sulphur, halogens and trace metals by volcanic ash: The 2010 Eyjafjallajökull eruption. ***Geochimica et Cosmochimica Acta***, 103:138–160.

Ball, J. G. C., Reed, B. E., Grainger, R. G., Peters, D. M., Mather, T. A., and Pyle, D. M. (2015). Measurements of the complex refractive index of volcanic ash at 450, 546.7, and 650 nm. ***Journal of Geophysical Research Atmospheres***, 120(15):7747–7757.

Barton, I. J., Prata, A. J., Watterson, I. G., and Young, S. A. (1992). Identification of the Mount Hudson volcanic cloud over SE Australia. ***Geophysical Research Letters***, 19(12):1211–1214.

Beckett, F. M., Witham, C. S., Hort, M. C., Stevenson, J. A., Bonadonna, C., and Millington, S. C. (2015). Sensitivity of dispersion model forecasts of volcanic ash clouds to the physical characteristics of the particles. ***Journal of Geophysical Research: Atmospheres***, 120(22):11,636–11,652.

Beeston, M., Grgić, I., van Elteren, J. T., Iskra, I., Kapun, G., and Močnik, G. (2012). Chemical and morphological characterization of aerosol particles at Mt. Krvavec, Slovenia, during the Eyjafjallajökull Icelandic volcanic eruption. ***Environmental Science and Pollution Research***, 19(1):235–243.

Birmili, W., Allen, A. G., Bary, F., and Harrison, R. M. (2006). Trace metal concentrations and water solubility in size-fractionated atmospheric particles and influence of road traffic. ***Environmental Science and Technology***, 40(4):1144–1153.

Bohren, C. F. and Huffman, D. R. (1983). ***Absorption and scattering of light by small particles***. John Wiley & Sons, New York.

Brown, R. J., Bonadonna, C., and Durant, A. J. (2012). A Review of Volcanic Ash Aggregation. ***Physics and Chemistry of the Earth, Parts A/B/C***, 45-46:65–78.

Brown, R. J. C., Yardley, R. E., Muhunthan, D., Butterfield, D. M., Williams, M., Woods, P. T., Brown, A. S., and Goddard, S. L. (2008). Twenty-five years of nationwide ambient metals measurement in the United Kingdom: concentration levels and trends. ***Environmental Monitoring and Assessment***, 142(1-3):127–140.

Browning, T. J., Bouman, H. A., Henderson, G. M., Mather, T. A., Pyle, D. M., Schlosser, C., Woodward, E. M. S., and Moore, C. M. (2014). Strong responses of Southern Ocean phytoplankton communities to volcanic ash. ***Geophysical Research Letters***, 41(8):2851–2857.

Browning, T. J., Stone, K., Bouman, H. A., Mather, T. A., Pyle, D. M., Moore, C. M., and Martinez-Vicente, V. (2015). Volcanic ash supply to the surface ocean—remote sensing of biological responses and their wider biogeochemical significance. ***Frontiers in Marine Science***, 2:14.

Bukowiecki, N., Zieger, P., Weingartner, E., Jurányi, Z., Gysel, M., Neininger, B., Schneider, B., Hueglin, C., Ulrich, A., Wichser, A., Henne, S., Brunner, D., Kaegi, R., Schwikowski, M., Tobler, L., Wienhold, F. G., Engel, I., Buchmann, B., Peter, T., and Baltensperger, U. (2011). Ground-based and airborne in-situ measurements of the Eyjafjallajökull volcanic aerosol plume in Switzerland in spring 2010. ***Atmospheric Chemistry and Physics***, 11(19):10011–10030.

Bursik, M. I., Kobs, S. E., Burns, A., Braitseva, O. A., Bazanova, L. I., Melekestsev, I. V., Kurbatov, A., and Pieri, D. C. (2009). Volcanic plumes and wind: Jetstream interaction examples and implications for air traffic. ***Journal of Volcanology and Geothermal Research***, 186(1-2):60–67.

Bursik, M. I., Sparks, R. S. J., Gilbert, J. S., and Carey, S. N. (1992). Sedimentation of tephra by volcanic plumes: I. Theory and its comparison with a study of the Fogo A plinian deposit, Sao Miguel (Azores). ***Bulletin of Volcanology***, 54(4):329–344.

Campanelli, M., Estelles, V., Smyth, T., Tomasi, C., Martìnez-Lozano, M., Claxton, B., Muller, P., Pappalardo, G., Pietruczuk, A., Shanklin, J., Colwell, S., Wrench, C., Lupi, A., Mazzola, M., Lanconelli, C., Vitale, V., Congeduti, F., Dionisi, D., Cardillo, F., Cacciani, M., Casasanta, G., and Nakajima, T. (2012). Monitoring of Eyjafjallajökull volcanic aerosol by the new European Skynet Radiometers (ESR) network. ***Atmospheric Environment***, 48:33–45.

Casadevall, T. J. (1994). Volcanic ash and aviation safety: proceedings of the first international symposium on volcanic ash and aviation safety. ***US Geological Survey Bulletin***, 2047:1–6.

Cashman, K. and Rust, A. C. (2016). Volcanic ash: generation and spatial variations. In Mackie, S., Cashman, K., Ricketts, H., Rust, A. C., and Watson, I. M., editors, ***Volcanic Ash: Hazard Observation***, number 2, pages 5–24. Elsevier Ltd.

Chester, R. (2000). ***Marine geochemistry***. Blackwell Science, Oxford, UK, 2nd edition.

Clarisse, L. and Prata, A. J. (2016). Infrared Sounding of Volcanic Ash. In Mackie, S., Cashman, K., Ricketts, H., and Watson, I. M., editors, ***Volcanic Ash: Hazard Observation***, number 11, pages 189–216. Elsevier Ltd.

Clarisse, L., Prata, A. J., Lacour, J.-L., Hurtmans, D., Clerbaux, C., and Coheur, P.-F. (2010). A correlation method for volcanic ash detection using hyperspectral infrared measurements. ***Geophysical Research Letters***, 37(19):L19806.

Clark, R. N. (1999). Spectroscopy of rocks and minerals, and principles of spectroscopy. In Rencz, A. N., editor, ***Remote sensing for the earth sciences: Manual of remote sensing***, volume 3, chapter 1, pages 3–52. John Wiley & Sons, 3rd edition.

Clarkson, R. J., Majewicz, E. J., and Mack, P. (2016). A re-evaluation of the 2010 quantitative understanding of the effects volcanic ash has on gas turbine engines. ***Proceedings of the Institution of Mechanical Engineers, Part G: Journal of Aerospace Engineering***, 230(12):2274–2291.

Colette, A., Favez, O., Meleux, F., Chiappini, L., Haeffelin, M., Morille, Y., Malherbe, L., Papin, A., Bessagnet, B., Menut, L., Leoz, E., and Rouïl, L. (2011). Assessing in near real time the impact of the April 2010 Eyjafjallajökull ash plume on air quality. ***Atmospheric Environment***, 45(5):1217–1221.

Costa, A., Macedonio, G., and Folch, A. (2006). A three-dimensional Eulerian model for transport and deposition of volcanic ashes. ***Earth and Planetary Science Letters***, 241(3-4):634–647.

Dacre, H. F., Grant, A. L. M., and Johnson, B. T. (2013). Aircraft observations and model simulations of concentration and particle size distribution in the Eyjafjallajökull volcanic ash cloud. ***Atmospheric Chemistry and Physics***, 13(3):1277–1291.

De Rosa, R. (1999). Compositional modes in the ash fraction of some modern pyroclastic deposits: their determination and significance. ***Bulletin of Volcanology***, 61(3):162–173.

Di Genova, D., Morgavi, D., Hess, K.-U., Neuville, D. R., Borovkov, N., Perugini, D., and Dingwell, D. B. (2015). Approximate chemical analysis of volcanic glasses using Raman spectroscopy. ***Journal of Raman Spectroscopy***, 46(12):1235–1244.

Dixon, J. L. (2008). Macro and micro nutrient limitation of microbial productivity in oligotrophic subtropical Atlantic waters. ***Environmental Chemistry***, 5(2):135.

Duggen, S., Olgun, N., Croot, P., Hoffmann, L. J., Dietze, H., Delmelle, P., and Teschner, C. (2010). The role of airborne volcanic ash for the surface ocean biogeochemical iron-cycle: a review. ***Biogeosciences***, 7:827–844.

Durant, A. J., Bonadonna, C., and Horwell, C. J. (2010). Atmospheric and environmental impacts of volcanic particulates. ***Elements***, 6(4):235.

Durant, A. J., Rose, W. I., Sarna-Wojcicki, A. M., Carey, S., and Volentik, A. C. M. (2009). Hydrometeor-enhanced tephra sedimentation: Constraints from the 18 May 1980 eruption of Mount St. Helens. ***Journal of Geophysical Research-Solid Earth***, 114(B3):B03204.

Francis, P. N., Cooke, M. C., and Saunders, R. W. (2012). Retrieval of physical properties of volcanic ash using Meteosat: A case study from the 2010 Eyjafjallajökull eruption. ***Journal of Geophysical Research: Solid Earth***, 117(D20).

Frogner, P., Gíslason, S. R., and Oskarsson, N. (2001). Fertilizing potential of volcanic ash in ocean surface water. ***Geology***, 29(6):487.

Gangale, G., Prata, A., and Clarisse, L. (2010). The infrared spectral signature of volcanic ash determined from high-spectral resolution satellite measurements. ***Remote Sensing of Environment***, 114(2):414–425.

Giordano, D., Russell, J. K., and Dingwell, D. B. (2008). Viscosity of magmatic liquids: A model. ***Earth and Planetary Science Letters***, 271(1-4):123–134.

Gíslason, S. R., Hassenkam, T., Nedel, S., Bovet, N., Eiríksdóttir, E. S., Alfredsson, H. A., Hem, C. P., Balogh, Z. I., Dideriksen, K., Oskarsson, N., Sigfusson, B., Larsen, G., and Stipp, S. L. S. (2011). Characterization of Eyjafjallajökull volcanic ash particles and a protocol for rapid risk assessment. ***PNAS***, 108(18):7307–7312.

Grainger, R. G., Peters, D. M., Thomas, G. E., Smith, A. J. A., Siddans, R., Carboni, E., and Dudhia, A. (2013). Measuring volcanic plume and ash properties from space. In ***Remote Sensing of Volcanoes and Volcanic Processes: Integrating Observation and Modelling***, volume 380, pages 293–320. Geological Society, London, Special Publications.

Gudmundsson, M. T., Thordarson, T., Höskuldsson, A., Larsen, G., Björnsson, H., Prata, F. J., Oddsson, B., Magnússon, E., Högnadóttir, T., Petersen, G. N., Hayward, C. L., Stevenson, J. A., and Jónsdóttir, I. (2012). Ash generation and distribution from the April-May 2010 eruption of Eyjafjallajökull, Iceland. ***Scientific reports***, 2:572.

Guffanti, M., Mayberry, G. C., Casadevall, T. J., and Wunderman, R. (2009). Volcanic hazards to airports.

Harbin, M., Swanson, S., Nye, C., and Miller, T. (1995). Preliminary petrology and chemistry of proximal eruptive products; 1992 eruptions of Crater Peak, Mount Spurr Volcano, Alaska. In Keith, T., editor, ***The 1992 eruptions of Crater Peak vent, Mount Spurr Volcano, Alaska***, pages 139–148. U. S. Geological Survey Professional Paper.

Heiken, G. and Wohletz, K. (1985). ***Volcanic Ash***. University of California Press, Berkley.

Herbin, H., Pujol, O., Hubert, P., and Petitprez, D. (2017). New approach for the determination of aerosol refractive indices - Part I: Theoretical bases and numerical methodology. ***Journal of Quantitative Spectroscopy and Radiative Transfer***, 200:1–30.

Hobbs, P. V., Radke, L. F., Eltgroth, M. W., and Hegg, D. A. (1981). Airborne studies of the emissions from the volcanic eruptions of mount st. Helens. ***Science***, 211(4484):816–8.

Horwell, C., Baxter, P., Hillman, S., Calkins, J., Damby, D., Delmelle, P., Donaldson, K., Dunster, C., Fubini, B., Kelly, F., Le Blond, J., Livi, K., Murphy, F., Nattrass, C., Sweeney, S., Tetley, T., Thordarson, T., and Tomatis, M. (2013). Physicochemical and toxicological profiling of ash from the 2010 and 2011 eruptions of Eyjafjallajökull and Grímsvötn volcanoes, Iceland using a rapid respiratory hazard assessment protocol. ***Environmental Research***.

Horwell, C. J. (2007). Grain-size analysis of volcanic ash for the rapid assessment of respiratory health hazard. ***Journal of environmental monitoring : JEM***, 9(10):1107–15.

Horwell, C. J. and Baxter, P. J. (2006). The respiratory health hazards of volcanic ash: a review for volcanic risk mitigation. ***Bulletin of Volcanology***, 69(1):1–24.

Hoshyaripour, G., Hort, M., Langmann, B., and Delmelle, P. (2014). Volcanic controls on ash iron solubility: New insights from high-temperature gas–ash interaction modeling. ***Journal of Volcanology and Geothermal Research***, 286:67–77.

ICAO (2016). Volcanic Ash Contingency Plan, European and North Atlantic Regions. EUR Doc. 019, NAT Doc. 006, Part II. Edition 2.0.0 – July 2016. International Civil Aviation Organization: Neuilly-sur-Seine, France.

Ishimoto, H., Masuda, K., Fukui, K., Shimbori, T., Inazawa, T., Tuchiyama, H., Ishii, K., and Sakurai, T. (2016). Estimation of the refractive index of volcanic ash from satellite infrared sounder data. 174:165–180.

Jickells, T. D., An, Z. S., Andersen, K. K., Baker, A. R., Bergametti, G., Brooks, N., Cao, J. J., Boyd, P. W., Duce, R. A., Hunter, K. A., Kawahata, H., Kubilay, N., LaRoche, J., Liss, P. S., Mahowald, N., Prospero, J. M., Ridgwell, A. J., Tegen, I., and Torres, R. (2005). Global iron connections between desert dust, ocean biogeochemistry, and climate. ***Science***, 308(5718):67–71.

Jones, M. T. and Gislason, S. R. (2008). Rapid releases of metal salts and nutrients following the deposition of volcanic ash into aqueous environments. ***Geochimica et Cosmochimica Acta***, 72(15):3661–3680.

Jones, M. T., Sparks, R. S. J., and Valdes, P. J. (2007). The climatic impact of supervolcanic ash blankets. ***Climate Dynamics***, 29(6):553–564.

Jordi, A., Basterretxea, G., Tovar-Sánchez, A., Alastuey, A., and Querol, X. (2012). Copper aerosols inhibit phytoplankton growth in the Mediterranean Sea. ***Proceedings of the National Academy of Sciences of the United States of America***, 109(52):21246–9.

Karlsdóttir, S., Gylfason, Á. G., Höskuldsson, Á., Brandsdóttir, B., Ilyinskaya, E., Gudmundsson, M. T., and Högnadóttir, □ . (2012). The 2010 Eyjafjallajökull eruption, Iceland. ***Report to ICAO***, page 209.

Keller, J., Ryan, W. B. F., Ninkovich, D., and Altherr, R. (1978). Explosive volcanic activity in the Mediterranean over the past 200,000 yr as recorded in deep-sea sediments. ***Geological Society of America Bulletin***, 89(4):591–604.

Kelly, F. J. and Fussell, J. C. (2012). Size, source and chemical composition as determinants of toxicity attributable to ambient particulate matter. ***Atmospheric Environment***, 60:504–526.

Kieffer, S. W. (1979). Thermodynamics and lattice vibrations of minerals: 2. Vibrational characteristics of silicates. ***Reviews of Geophysics***, 17(1):20–34.

Kitamura, R., Pilon, L., and Jonasz, M. (2007). Optical constants of silica glass from extreme ultraviolet to far infrared at near room temperature. ***Applied Optics***, 46(33):8118–8133.

Klüser, L., Erbertseder, T., and Meyer-Arnek, J. (2013). Observation of volcanic ash from Puyehue–Cordón Caulle with IASI. ***Atmospheric Measurement Techniques***, 6(1):35–46.

Krotkov, N., Flittner, D., Krueger, A., Kostinski, A., Riley, C., Rose, W., and Torres, O. (1999). Effect of particle non-sphericity on satellite monitoring of drifting volcanic ash clouds. ***Journal of Quantitative Spectroscopy and Radiative Transfer***, 63(2-6):613–630.

Langmann, B., Arboledas, L. A., Folch, A., Matthias, V., Lettino, A., Caggiano, R., Fiore, S., Macchiato, M., Sabia, S., and Trippetta, S. (2012). Eyjafjallajökull volcanic ash in southern Italy. ***Atmospheric Environment***, 48:97–103.

Langmann, B., Zakšek, K., and Hort, M. (2010a). Atmospheric distribution and removal of volcanic ash after the eruption of Kasatochi volcano: A regional model study. ***Journal of Geophysical Research-Solid Earth***, 115.

Langmann, B., Zaksek, K., Hort, M., and Duggen, S. (2010b). Volcanic ash as fertiliser for the surface ocean. ***Atmospheric Chemistry and Physics***, 10(8):3891–3899.

Larsen, J. F., Nye, C. J., Coombs, M. L., Tilman, M., Izbekov, P., and Cameron, C. (2010). Petrology and Geochemistry of the 2006 Eruption of Augustine Volcano. In Power, J. A., Coombs, M. L., and Freymueller, J. T., editors, ***The 2006 eruption of Augustine Volcano, Alaska: U.S. Geological Survey Professional Paper 1769***, chapter Chapter 15, pages 335–382.

Larsen, J. F., Śliwiński, M. G., Nye, C., Cameron, C., and Schaefer, J. R. (2013). The 2008 eruption of Okmok Volcano, Alaska: Petrological and geochemical constraints on the subsurface magma plumbing system. ***Journal of Volcanology and Geothermal Research***, 264:85–106.

Le Maitre, R. W., Streckeisen, A., Zanettin, B., Le Bas, M. J., Bonin, B., Bateman, P., Bellieni, G., Dudek, A., Efremova, S., Keller, J., Lameyre, J., Sabine, P. A., Schmid, R., Sorensen, H., Woolley, A. R., and Le Maitre, R. W. (2005). Igneous Rocks: A classification and glossary of terms.

Lettino, A., Caggiano, R., Fiore, S., Macchiato, M., Sabia, S., and Trippetta, S. (2012). Eyjafjallajökull volcanic ash in southern Italy. ***Atmospheric Environment***, 48(C):97–103.

Lieke, K. I., Kristensen, T. B., Korsholm, U. S., Sørensen, J. H., Kandler, K., Weinbruch, S., Ceburnis, D., Ovadnevaite, J., O 'dowd, C. D., Bilde, M., O'Dowd, C., and Bilde, M. (2013). Characterization of volcanic ash from the 2011 Grímsvötn eruption by means of single-particle analysis. ***Atmospheric Environment***, 79:411–420.

Longchamp, C., Bonadonna, C., Bachmann, O., and Skopelitis, A. (2011). Characterization of tephra deposits with limited exposure: The example of the two largest explosive eruptions at Nisyros volcano (Greece). ***Bulletin of Volcanology***, 73(9):1337–1352.

Mackie, S., Cashman, K., Ricketts, H., Rust, A. C., and Watson, I. M. (2016). ***Volcanic Ash: Hazard Observation***. Elsevier, Amsterdam, Netherlands.

Mackie, S., Millington, S., and Watson, I. M. (2014). How assumed composition affects the interpretation of satellite observations of volcanic ash. ***Meteorological Applications***, 21(1):20–29.

Marti, A., Folch, A., Jorba, O., and Janjic, Z. (2017). Volcanic ash modeling with the online NMMB-MONARCH-ASH v1.0 model: Model description, case simulation, and evaluation. ***Atmospheric Chemistry and Physics***, 17(6):4005–4030.

Mastin, L. G., Guffanti, M., Servranckx, R., Webley, P., Barsotti, S., Dean, K., Durant, A., Ewert, J. W., Neri, A., Rose, W. I., Schneider, D., Siebert, L., Stunder, B., Swanson, G., Tupper, A., Volentik, A., and Waythomas, C. F. (2009). A multidisciplinary effort to assign realistic source parameters to models of volcanic ash-cloud transport and dispersion during eruptions. ***Journal of Volcanology and Geothermal Research***, 186(1-2):10–21.

Maters, E. C., Delmelle, P., and Gunnlaugsson, H. P. (2017). Controls on iron mobilisation from volcanic ash at low pH: Insights from dissolution experiments and Mössbauer spectroscopy. ***Chemical Geology***, 449:73–81.

Mather, T. A., Pyle, D. M., and Oppenheimer, C. (2003). Tropospheric volcanic aerosol. In ***Geophysical Monograph Series***, volume 139, pages 189–212.

Mazzocchi, M. ., Hansstein, F. ., and Ragona, M. (2010). The 2010 Volcanic Ash Cloud and Its Financial Impact on the European Airline Industry. ***CESifo Forum***, 11(2):92–100.

Middlemost, E. A. K. (1975). The basalt clan. ***Earth Science Reviews***, 11(4):337–364.

Middlemost, E. A. K. (1989). Iron oxidation ratios, norms and the classification of volcanic rocks. ***Chemical Geology***, 77(1):19–26.

Mills, K. C. (1993). The influence of strcuture on the physico-chemical properties of slags. ***ISIJ International***, 33(1):148–155.

Mysen, B. O. and Richet, P. (2005). ***Silicate Glasses and Melts***. Elsevier, Amsterdam, Netherlands.

Mysen, B. O., Virgo, D., and Seifert, F. A. (1982). The structure of silicate melts: Implications for chemical and physical properties of natural magma. ***Reviews of Geophysics***, 20(3):353.

O'Dowd, C., Ceburnis, D., Ovadnevaite, J., Martucci, G., Bialek, J., Monahan, C., Berresheim, H., Vaishya, A., Grigas, T., Jennings, S. G., McVeigh, P., Varghese, S., Flanagan, R., Martin, D., Moran, E., Lambkin, K., Semmler, T., Perrino, C., and McGrath, R. (2012). The Eyjafjallajökull ash plume - Part I: Physical, chemical and optical characteristics. ***Atmospheric Environment***, 48:129–142.

Olgun, N., Duggen, S., Croot, P. L., Delmelle, P., Dietze, H., Schacht, U., Óskarsson, N., Siebe, C., Auer, A., and Garbe-Schönberg, D. (2011). Surface ocean iron fertilization: The role of airborne volcanic ash from subduction zone and hot spot volcanoes and related iron fluxes into the Pacific Ocean. ***Global Biogeochemical Cycles***, 25(GB4001).

Pappalardo, G., Mona, L., D'Amico, G., Wandinger, U., Adam, M., Amodeo, A., Ansmann, A., Apituley, A., Alados Arboledas, L., Balis, D., Boselli, A., Bravo-Aranda, J. A., Chaikovsky, A., Comeron, A., Cuesta, J., De Tomasi, F., Freudenthaler, V., Gausa, M., Giannakaki, E., Giehl, H., Giunta, A., Grigorov, I., Groß, S., Haeffelin, M., Hiebsch, A., Iarlori, M., Lange, D., Linné, H., Madonna, F., Mattis, I., Mamouri, R.-E., McAuliffe, M. A. P., Mitev, V., Molero, F., Navas-Guzman, F., Nicolae, D., Papayannis, A., Perrone, M. R., Pietras, C., Pietruczuk, A., Pisani, G., Preißler, J., Pujadas, M., Rizi, V., Ruth, A. A., Schmidt, J., Schnell, F., Seifert, P., Serikov, I., Sicard, M., Simeonov, V., Spinelli, N., Stebel, K., Tesche, M., Trickl, T., Wang, X., Wagner, F., Wiegner, M., and Wilson, K. M. (2013). Four-dimensional distribution of the 2010 Eyjafjallajökull volcanic cloud over Europe observed by EARLINET. ***Atmospheric Chemistry and Physics***, 13(8):4429–4450.

Patterson, E. M. (1975). Optical absorption coefficients of soil aerosol particles and

volcanic ash between 1 and 16 μm. ***Second Conference on Atmospheric Radiation***, pages 177–180.

Patterson, E. M. (1981). Measurements of the imaginary part of the refractive index between 300 and 700 nanometers for Mount St. Helens ash. ***Science***, 211(4484):836–838.

Patterson, E. M., Pollard, C. O., and Galindo, I. (1983). Optical properties of the ash from El Chichon volcano. ***Geophysical Research Letters***, 10(4):317–320.

Pavolonis, M. J. (2010). Advances in Extracting Cloud Composition Information from Spaceborne Infrared Radiances—A Robust Alternative to Brightness Temperatures. Part I: Theory. ***Journal of Applied Meteorology and Climatology***, 49(9):1992–2012.

Pavolonis, M. J., Feltz, W. F., Heidinger, A. K., Gallina, G. M., Pavolonis, M. J., Feltz, W. F., Heidinger, A. K., and Gallina, G. M. (2006). A Daytime Complement to the Reverse Absorption Technique for Improved Automated Detection of Volcanic Ash. ***Journal of Atmospheric and Oceanic Technology***, 23(11):1422–1444.

Paytan, A., Mackey, K. R. M., Chen, Y., Lima, I. D., Doney, S. C., Mahowald, N., Labiosa, R., and Post, A. F. (2009). Toxicity of atmospheric aerosols on marine phytoplankton. ***Proceedings of the National Academy of Sciences of the United States of America***, 106(12):4601–5.

Petäjä, T., Laakso, L., Grönholm, T., Launiainen, S., Evele-Peltoniemi, I., Virkkula, A., Leskinen, A., Aurela, M., Hakola, H., Makkonen, U., Hellén, H., Hillamo, R., Vira, J., Prank, M., Sofiev, M., Siitari-kauppi, M., Laaksonen, A., J, K. E., Kulmala, M., Viisanen, Y., Kerminen, V. M., Backman, J., Manninen, H. E., Sipilä, M., Haapanala, S., Hämeri, K., Vanhala, E., Tuomi, T., Paatero, J., Aurela, M., Hakola, H., Makkonen, U., Hellén, H., Hillamo, R., Vira, J., Prank, M., Sofiev, M., Siitari-kauppi, M., Laaksonen, A., Lehtinen, K. E. J., Kulmala, M., Viisanen, Y., and Ker-

minen, V. M. (2012). In-situ observations of Eyjafjallajökull ash particles by hot-air balloon. ***Atmospheric Environment***, 48(C):104–112.

Petty, G. W. (2006). ***A First Course in Atmospheric Radiation***. Sundog Pub, 2nd edition.

Pollack, J. B., Toon, O. B., and Khare, B. N. (1973). Optical Properties of Some Terrestrial Rocks and Glasses. ***Icarus***, 19(3):372–389.

Prata, A. J. (1989). Infrared radiative transfer calculations for volcanic ash clouds. ***Geophysical Research Letters***, 16(11):1293–1296.

Prata, A. J. (2009). Satellite detection of hazardous volcanic clouds and the risk to global air traffic. ***Natural Hazards***, 51(2):303–324.

Prata, A. J., Dezitter, F., Davies, I., Weber, K., Birnfeld, M., Moriano, D., Bernardo, C., Vogel, A., Prata, G. S., Mather, T. A., Thomas, H. E., Cammas, J., and Weber, M. (2016). Artificial cloud test confirms volcanic ash detection using infrared spectral imaging. ***Scientific Reports***, 6:25620.

Prata, A. J. and Grant, I. F. (2001). Retrieval of microphysical and morphological properties of volcanic ash plumes from satellite data: Application to Mt Ruapehu, New Zealand. ***Quarterly Journal of the Royal Meteorological Society***, 127(576):2153–2179.

Prata, A. J. and Prata, A. T. (2012). Ejafjallajökull volcanic ash concentrations determined form SEVIRI measurements. ***Journal of Geophysical Research Atmospheres***, 117:1–25.

Prata, A. J. and Tupper, A. (2009). Aviation hazards from volcanoes: the state of the science. ***Natural Hazards***, 51(2):239–244.

Prata, A. J., Woodhouse, M., Huppert, H. E., Prata, A., Thordarson, T., and Carn, S. (2017). Atmospheric processes affecting the separation of volcanic ash and SO_2 in

volcanic eruptions: inferences from the May 2011 Grímsvötn eruption. ***Atmospheric Chemistry and Physics***, 17(17):10709–10732.

Prata, A. T. (2016). Remote sensing of volcanic eruptions: from aviation hazards to global cooling. In Duarte, J. C. and Schellart, W. P., editors, ***Plate boundaries and natural hazards***, pages 289–322.

Prata, F. and Prata, G. (2015). Remote sensing of volcanic ash and sulfur dioxide. In Schmidt, A., Fristad, K. E., and Elkins-Tanton, L. T., editors, ***Volcanism and Global Environmental Change***. Cambridge University Press, Cambridge, UK.

Rauthe-Schöch, A., Weigelt, A., Hermann, M., Martinsson, B. G., Baker, A. K., Heue, K.-P., M Brenninkmeijer, C. A., Zahn, A., Scharffe, D., Eckhardt, S., Stohl, A., and J van Velthoven, P. F. (2012). CARIBIC aircraft measurements of Eyjafjallajokull volcanic clouds in April/May 2010 CARIBIC aircraft measurements of Eyjafjallajökull volcanic clouds in April/May 2010. ***Atmospheric Chemistry and Physics Atmos. Chem. Phys. Atmospheric Chemistry and Physics***, 12(12):879–902.

Reed, B. E., Peters, D. M., McPheat, R., and Grainger, R. G. (2018). The complex refractive index of volcanic ash aerosol retrieved from spectral mass extinction. ***Journal of Geophysical Research Atmospheres***, 96(1):36–62.

Reed, B. E., Peters, D. M., McPheat, R., Smith, A. J., and Grainger, R. (2017). Mass extinction spectra and size distribution measurements of quartz and amorphous silica aerosol at 0.33–19 μm compared to modelled extinction using Mie, CDE, and T-matrix theories. ***Journal of Quantitative Spectroscopy and Radiative Transfer***, 199:1–19.

Revuelta, M. A., Sastre, M., Fernández, A. J., Martin, L., García, R., Gómez-Moreno, F. J., Artíñano, B., Pujadas, M., and Molero, F. (2012). Characterization of the Eyjafjallajökull volcanic plume over the Iberian Peninsula by lidar remote sensing and ground-level data collection. ***Atmospheric Environment***, 48(C):46–55.

Robock, A. (2015). Climatic Impacts of Volcanic Eruptions. In Sigurdsson, H., Houghton, B. F., McNutt, S., Rymer, H., and Stix, J., editors, ***The Encyclopedia of Volcanoes***, chapter 53, pages 935–942. Elsevier, Amsterdam, Netherlands, 2nd edition.

Rocha-Lima, A., Martins, J. V., Remer, L. A., Krotkov, N. A., Tabacniks, M. H., Ben-Ami, Y., and Artaxo, P. (2014). Optical, microphysical and compositional properties of the Eyjafjallajökull volcanic ash. ***Atmospheric Chemistry and Physics***, 14:10649–10661.

Rose, W. I. and Durant, A. J. (2009). Fine ash content of explosive eruptions. ***Journal of Volcanology and Geothermal Research***, 186(1-2):32–39.

Rossini, P., Molinaroli, E., De Falco, G., Fiesoletti, F., Papa, S., Pari, E., Renzulli, A., Tentoni, P., Testoni, A., Valentini, L., and Matteucci, G. (2012). April-May 2010 Eyjafjallajökull volcanic fallout over Rimini, Italy. ***Atmospheric Environment***, 48(null):122–128.

Saito, M. A. and Goepfert, T. J. (2008). Zinc-cobalt colimitation of Phaeocystis antarctica. ***Limnology and Oceanography***, 53(1):266–275.

Sandrini, S., Giulianelli, L., Decesari, S., Fuzzi, S., Cristofanelli, P., Marinoni, A., Bonasoni, P., Chiari, M., Calzolai, G., Canepari, S., Perrino, C., and Facchini, M. C. (2014). In situ physical and chemical characterisation of the Eyjafjallajökull aerosol plume in the free troposphere over Italy. ***Atmospheric Chemistry and Physics***, 14(2):1075–1092.

Schäfer, K., Thomas, W., Peters, A., Ries, L., Obleitner, F., Schnelle-Kreis, J., Birmili, W., Diemer, J., Fricke, W., Junkermann, W., Pitz, M., Emeis, S., Forkel, R., Suppan, P., Flentje, H., Gilge, S., Wichmann, H. E., Meinhardt, F., Zimmermann, R., Weinhold, K., Soentgen, J., Münkel, C., Freuer, C., and Cyrys, J. (2011). Influences of

the 2010 Eyjafjallajökull volcanic plume on air quality in the northern Alpine region. ***Atmospheric Chemistry and Physics***, 11(16):8555–8575.

Schleicher, N., Kramar, U., Dietze, V., Kaminski, U., and Norra, S. (2012). Geochemical characterization of single atmospheric particles from the Eyjafjallajökull volcano eruption event collected at ground-based sampling sites in Germany. ***Atmospheric Environment***, 48:113–121.

Schumann, U., Weinzierl, B., Reitebuch, O., Schlager, H., Minikin, A., Forster, C., Baumann, R., Sailer, T., Graf, K., Mannstein, H., Voigt, C., Rahm, S., Simmet, R., Scheibe, M., Lichtenstern, M., Stock, P., Rüba, H., Schäuble, D., Tafferner, A., Rautenhaus, M., Gerz, T., Ziereis, H., Krautstrunk, M., Mallaun, C., Gayet, J. F., Lieke, K., Kandler, K., Ebert, M., Weinbruch, S., Stohl, A., Gasteiger, J., Olafsson, H., and Sturm, K. (2011). Airborne observations of the Eyjafjalla volcano ash cloud over Europe during air space closure in April and May 2010. ***Atmospheric Chemistry and Physics Discussions***, 11:2245–2279.

Sigmarsson, O., Vlastelic, I., Andreasen, R., Bindeman, I., Devidal, J.-L., Moune, S., Keiding, J. K., Larsen, G., Höskuldsson, Á., and Thordarson, T. (2011). Remobilization of silicic intrusion by mafic magmas during the 2010 Eyjafjallajökull eruption. ***Solid Earth***, 2(2):271–281.

Sigmundsson, F., Hreinsdóttir, S., Hooper, A., Árnadóttir, T., Pedersen, R., Roberts, M. J., Óskarsson, N., Auriac, A., Decriem, J., Einarsson, P., Geirsson, H., Hensch, M., Ófeigsson, B. G., Sturkell, E., Sveinbjörnsson, H., and Feigl, K. L. (2010). Intrusion triggering of the 2010 Eyjafjallajökull explosive eruption. ***Nature***, 468(7322):426–430.

Sigurdsson, H., Houghton, B. F., McNutt, S., Rymer, H., and Stix, J., editors (2015). ***Encyclopedia of volcanoes***. Elsevier, Amsterdam, Netherlands, 2nd edition.

Song, W., Lavallée, Y., Hess, K.-U., Kueppers, U., Cimarelli, C., and Dingwell, D. B. (2016). Volcanic ash melting under conditions relevant to ash turbine interactions. ***Nature Communications***, 7:10795.

Sparks, R. S. J., Wilson, L., and Sigurdsson, H. (1981). The Pyroclastic Deposits of the 1875 Eruption of Askja, Iceland. ***Philosophical Transactions of the Royal Society A: Mathematical, Physical and Engineering Sciences***, A299(1447):241–273.

Spence, R. J. S., Kelman, I., Baxter, P. J., Zuccaro, G., and Petrazzuoli, S. (2005). Residential building and occupant vulnerability to tephra fall. ***Natural Hazards and Earth System Science***, 5(4):477–494.

Spokes, L., Jickells, T., and Jarvis, K. (2001). Atmospheric inputs of trace metals to the northeast Atlantic Ocean: the importance of southeasterly flow. ***Marine Chemistry***, 76(4):319–330.

Stein, A. F., Draxler, R. R., Rolph, G. D., Stunder, B. J. B., Cohen, M. D., Ngan, F., Stein, A. F., Draxler, R. R., Rolph, G. D., Stunder, B. J. B., Cohen, M. D., and Ngan, F. (2015). NOAA's HYSPLIT Atmospheric Transport and Dispersion Modeling System. ***Bulletin of the American Meteorological Society***, 96(12):2059–2077.

Stevenson, J. A., Loughlin, S., Rae, C., Thordarson, T., Milodowski, A. E., Gilbert, J. S., Harangi, S., Lukács, R., Højgaard, B., Árting, U., Pyne-O'Donnell, S., MacLeod, A., Whitney, B., and Cassidy, M. (2012). Distal deposition of tephra from the Eyjafjallajökull 2010 summit eruption. ***Journal of Geophysical Research: Solid Earth***, 117(B9).

Stohl, A., Prata, A. J., Eckhardt, S., Clarisse, L., Durant, A., Henne, S., Kristiansen, N. I., Minikin, A., Schumann, U., Seibert, P., Stebel, K., Thomas, H. E., Thorsteinsson, T., Tørseth, K., and Weinzierl, B. (2011). Determination of time- and height-resolved volcanic ash emissions and their use for quantitative ash dispersion mod-

eling: the 2010 eyjafjallajökull eruption. ***Atmospheric Chemistry and Physics***, 11(9):4333–4351.

Thomas, H. E. and Prata, A. J. (2011). Sulphur dioxide as a volcanic ash proxy during the April-May 2010 eruption of Eyjafjallajökull Volcano, Iceland. ***Atmospheric Chemistry and Physics***, 11(14):6871–6880.

Toledano, C., Bennouna, Y., Cachorro, V., Ortiz de Galisteo, J., Stohl, A., Stebel, K., Kristiansen, N., Olmo, F., Lyamani, H., Obregón, M., Estellés, V., Wagner, F., Baldasano, J., González-Castanedo, Y., Clarisse, L., and de Frutos, A. (2012). Aerosol properties of the Eyjafjallajökull ash derived from sun photometer and satellite observations over the Iberian Peninsula. ***Atmospheric Environment***, 48:22–32.

Ventress, L. J., McGarragh, G., Carboni, E., Smith, A. J., and Grainger, R. G. (2016). Retrieval of ash properties from IASI measurements. ***Atmospheric Measurement Techniques***, 9(11):5407–5422.

Vogel, A., Diplas, S., Durant, A. J., Azar, A. S., Sunding, M. F., Rose, W. I., Sytchkova, A., Bonadonna, C., Krüger, K., and Stohl, A. (2017). Reference data set of volcanic ash physicochemical and optical properties. ***Journal of Geophysical Research Atmospheres***, 122(17):9485–9514.

Vogel, A., Weber, K., Eliasson, J., Palsson, A., Moser, H. M., Palsson, T., von Löwis, S., and Fischer, C. (2012). Airborne and groundbased measurements of ash particles on Iceland and over Germany during the Grímsvötn eruption May 2011. In ***EGU General Assembly 2012, held 22-27 April, 2012 in Vienna, Austria.***, volume 14, page 12854.

Volz, F. E. (1973). Infrared optical-constants of ammonium sulfate, Sahara dust, volcanic pumice, and flyash. ***Applied Optics***, 12(3):564–568.

Walter, L. S. and Salisbury, J. W. (1989). Spectral characterization of igneous rocks in the 8- to 12-μm region. ***Journal of Geophysical Research: Solid Earth***, 94(B7):9203–9213.

Watson, A. J. (1997). Volcanic iron, CO_2, ocean productivity and climate. ***Nature***, 385:587–588.

Watt, S. F. L., Pyle, D. M., Mather, T. A., Martin, R. S., and Matthews, N. E. (2009). Fallout and distribution of volcanic ash over Argentina following the May 2008 explosive eruption of Chaitén, Chile. ***Journal of Geophysical Research***, 114(B4):B04207.

Weber, K., Eliasson, J., Vogel, A., Fischer, C., Pohl, T., Van Haren, G., Meier, M., Grobéty, B., and Dahmann, D. (2012). Airborne in-situ investigations of the Eyjafjallajökull volcanic ash plume on Iceland and over north-western Germany with light aircrafts and optical particle counters. ***Atmospheric Environment***, 48:9–21.

Wen, S. and Rose, W. I. (1994). Retrieval of sizes and total masses of particles in volcanic clouds using AVHRR bands 4 and 5. ***Journal of Geophysical Research***, 99(D3):5421–5431.

Werner, M., Kryza, M., Dore, A. J., Bla, M., Hallsworth, S., Vieno, M., Tang, Y. S., and Smith, R. I. (2011). Modelling of marine base cation emissions, concentrations and deposition in the UK. ***Atmos. Chem. Phys. Atmospheric Chemistry and Physics***, 11:1023–1037.

Wilson, G., Wilson, T., Cole, J., and Oze, C. (2012a). Vulnerability of laptop computers to volcanic ash and gas. ***Natural Hazards***, 63(2):711–736.

Wilson, T. M., Stewart, C., Sword-Daniels, V., Leonard, G. S., Johnston, D. M., Cole, J. W., Wardman, J., Wilson, G., and Barnard, S. T. (2012b). Volcanic ash impacts on critical infrastructure. ***Physics and Chemistry of the Earth, Parts A/B/C***, 45-46:5 – 23. Volcanic ash: an agent in Earth systems.

Witham, C., Oppenheimer, C., and Horwell, C. (2005). Volcanic ash-leachates: a review and recommendations for sampling methods. ***Journal of Volcanology and Geothermal Research***, 141(3):299–326.

Witt, M., Meheran, N., Mather, T. A., de Hoog, J., and Pyle, D. (2010). Aerosol trace metals, particle morphology and total gaseous mercury in the atmosphere of Oxford, UK. ***Atmospheric Environment***, 44(12):1524–1538.

Woodhouse, M., Hogg, A., Phillips, J., and Sparks, R. (2013). Interaction between volcanic plumes and wind during the 2010 eyjafjallajokull eruption, iceland. ***Journal of Geophysical Research: Solid Earth***, 118(1):92–109.

Zehner, C. E. (2012). Monitoring Volcanic Ash from Space. ESA-EUMETSAT workshop on the 14 April to 23 May 2010 eruption at the Eyjafjöll volcano, South Iceland (ESA/ESRIN, 26–27 May 2010). ***ESA Publication STM-280***.

Zimanowski, B., Wohletz, K. H., Dellino, P., and Büttner, R. (2003). The volcanic ash problem. ***Journal of Volcanology and Geothermal Research***, 122(1):1–5.